

**Microwave-assisted synthesis of monodispersed  
Fe<sub>3</sub>O<sub>4</sub> nanoparticles: Size dependent properties and  
its application with PVDF as nanogenerator**

*A thesis submitted in partial fulfilment of the requirements for the degree of  
Master of Technology in Nano Science and Technology*

*By*  
**PRATIK CHATTOPADHYAY**  
**Roll. No.: M4NST19019**

*Under the guidance of*  
**Prof. Kalyan Kumar Chattopadhyay**  
**School of Material Science and Nanotechnology**  
**Jadavpur University, Kolkata**

*Course Affiliated to*  
**Faculty of Engineering and Technology**  
**Jadavpur University, Kolkata – 700032**  
**India**  
**2019**

## **CERTIFICATE OF RECOMMENDATION**

This is to certify that this thesis “**Microwave-assisted synthesis of monodispersed Fe<sub>3</sub>O<sub>4</sub> nanoparticles: Size dependent properties and its application with PVDF as Nano generator**” is a bonafide work carried out by **PRATIK CHATTOPADHYAY** under my supervision and guidance for the partial fulfilment of the requirements of Master of Technology (Nano Science and Technology) in School of Material Science and Nanotechnology during the academic session 2017– 2019.

---

### **THESIS ADVISOR**

**Prof. Kalyan Kumar Chattopadhyay**  
**School of Material Science and**  
**Nanotechnology**  
**Jadavpur University, Kolkata**

---

### **DIRECTOR**

**Prof. Chandan Kumar Ghosh**  
**School of Material Science and Nanotechnology**  
**Jadavpur University,**  
**Kolkata – 700032**

---

### **DEAN**

**Faculty of Interdisciplinary Studies, Law and Management**  
**Jadavpur University**  
**Kolkata**

**CERTIFICATE OF APPROVAL \*\***

This foregoing thesis is hereby approved as a credible study of an engineering subject carried out and presented in a manner satisfactorily to warrant its acceptance as a prerequisite to the degree for which it has been submitted. It is understood that by this approval, the undersigned do not endorse or approve any statement made or opinion expressed or conclusion drawn therein but approve the thesis only for the purpose for which it has been submitted.

**Committee of final examination  
for approval of thesis**

---

---

---

---

---

**\*\* Only if the thesis is approved**

*Dedicated to  
my parents and  
family*

## **Declaration of Originality and Compliance of Academic Ethics**

I hereby declare that this thesis contains literature survey and original research work done by The undersigned candidate, as part of his Master of Technology (Nano Science and Technology) studies during the academic session 2017 – 2019.

All information in this document is obtained and presented in accordance with academic and Ethical codes of conduct.

I also declare that, as required by the rules and conduct, I have fully cited and referred all Material and results that are not original to this work.

NAME: PRATIK CHATTOPADHYAY

ROLL NUMBER: M4NST19019

THESIS TITLE: Microwave-assisted synthesis of monodispersed Fe<sub>3</sub>O<sub>4</sub> nanoparticles: Size dependent properties and its application with PVDF as nanogenerator

Signature:

Date:

## **Acknowledgement**

First and foremost, I would like to express my sincerest gratitude to Prof. Kalyan Kumar Chattopadhyay for providing me with the opportunity to work under his guidance and pursue the research presented in this thesis. He has been a source of constant motivation and inspiration to me and my classmates for the last two years. I thank him for his valuable insight, guidance, help and patience over the last 12 months. I also thank him for giving me the chance of a lifetime, to work at Thin Film and Nanoscience Lab at JU, which has the best research environment and seniors who are always there to help.

I am also grateful to Prof. C.K. Ghosh Dr. S. Sarkar, Dr. M.G. Chowdhury for their valuable suggestions and constructive criticism during the course of my M. Tech program. Their enthusiasm and sagacious questioning provided me a helpful and effective way of learning which in turn inspired me to follow the research project with great vigour.

I would also like to express my sincerest gratitude to Dr. Nilesh Mazumder, and Souvik Bhattacharjee, without whom, the completion of this thesis would have been impossible. They were the brains behind the project, and the source of knowledge, guidance and inspiration that helped me continue to pursue this research even after multiple initial failures. No words can express how thankful I am to have had the opportunity of a lifetime to work under their guidance.

I am also really grateful to my laboratory senior Suvankar Mondal and Antika Das who showed me the ropes around the laboratory, and how to operate various instruments and machinery, and guided me in every possible way. I would also like to thank Karam da, Subhasis da and for helping me throughout the year.

I would also like to thank my friends and classmates Pulok da , Sumit ,Debnath ,Ankit, Ankita, sourav, utpal, anupam, saket, monikuntala and all the other seniors in the lab for their endless support.

## **Abstract**

Magnetite ( $\text{Fe}_3\text{O}_4$ ), a relaxor multiferroic material, has attracted much attention in the last decade due to the recent understandings of charge-ordering phenomena below Verwey transition and uncountable potential biomedical applications. Monodispersed and highly water dispersible spherical  $\text{Fe}_3\text{O}_4$  nanoparticles (NP's) with enormous variation in size (4 - 150 nm) can be synthesized by a facile microwave-assisted solvothermal approach using disodium tartrate as a crystal grain growth inhibitor and stabilizer in polyol medium. Temperature, pressure, crystal growth time, concentration of surfactants, and density of  $\text{Fe}^{3+}$  ions in the solution play key-role in tuning size. The resultant  $\text{Fe}_3\text{O}_4$  NP's; due to covalent surface-functionalization; exhibit an excellent long-term colloidal stability in aqueous or other polar solutions, which have been further confirmed by Zeta potential measurements. The calculated optical band-gap ( $E_g$ ) from UV-Vis-NIR absorption spectroscopy increases from 1.59 to 4.78 eV in a regular fashion with decreasing size of NP's, which can be well-explained in the light of Crystal Field Theory (CFT). The coordinative effect of carboxylate groups in the surface-composition is further verified from FTIR spectra, whereas thermal degradation of the as-prepared core-shell structure of the NP's was investigated by TGA-DTG measurements. A thorough XPS analysis revealed the difference in binding energies of the tetrahedral and octahedrally co-ordinated Fe atoms along with degree of stoichiometry and related surface-chemistry. A red-shifting and line-shape asymmetry of Raman peaks with smaller size was detected and illustrated by the Phonon Confinement Model (PCM). In addition, these  $\text{Fe}_3\text{O}_4$  NP's may be useful in other fields, such as hyperthermia treatment of cancer and targeted drug delivery because of their size-dependent magnetic property and excellent stability.

# Table of Contents

<i>Certificate of recommendation</i>	(i)
<i>Certificate of Approval</i>	(ii)
<i>Declaration</i>	(iii)
<i>Acknowledgement</i>	(iv)
<i>Abstract</i>	(v)

## ***Chapter 1 – Introduction to Nano Science and technology***

<i>1.1 Definition .....</i>	<i>2</i>
<i>1.2 History and fundamentals of nanotechnology.....</i>	<i>2</i>
<i>1.3 Current Trend and Status.....</i>	<i>8</i>
<i>1.4 Future .....</i>	<i>10</i>
<i>1.5 Application.....</i>	<i>11</i>
<i>1.6 References.....</i>	<i>15</i>



## ***Chapter 2 – Introduction to Magnetite ( $Fe_3O_4$ )***

<i>2.1 Overview</i> .....	<i>17</i>
<i>2.2 Crystal Structure</i> .....	<i>18</i>
<i>2.3 Magnetic Properties</i> .....	<i>18</i>
<i>2.4 Low Temperature Phase Transition</i> .....	<i>19</i>
<i>2.5 Reference</i> .....	<i>20</i>

## ***Chapter 3 – Review of past work***

<i>3.1 Introduction</i> .....	<i>22</i>
<i>3.2 Controversy</i> .....	<i>23</i>
<i>3.3 Future</i> .....	<i>23</i>
<i>3.4 Reference</i> .....	<i>24</i>

## Chapter 4 – Instruments and Apparatus

4.1 XRD .....	26
4.1.1 Basic Principle.....	26
4.1.2 Experimental Set up.....	27
4.2 HR TEM.....	28
4.2.1 Basic Principle.....	28
4.2.2 Experimental Set up.....	29
4.3 UV-VIS.....	31
4.3.1 Basic Principle.....	31
4.3.2 Experimental Set up.....	32
4.4 Photoluminescence (PL) .....	34
4.4.1 Basic Principle.....	34
4.4.2 Experimental Set up.....	36
4.5 Fourier Transform Infrared Spectroscopy.....	38
4.5.1 Basic Principle.....	38
4.5.2 Experimental Set up.....	39
4.6 Raman Spectroscopy.....	41
4.6.1 Basic Principle.....	41
4.6.2 Experimental Set up.....	43
4.7 Field emission scanning electron microscope (FESEM).....	45
4.7.1 Basic Principle.....	45
4.7.2 Experimental Set up.....	46

## Chapter-5 Novel synthesis and size-dependent properties of Fe<sub>3</sub>O<sub>4</sub> nanoparticles and related characterizations

5.1 Introduction.....	48
5.2 Microwave Synthesis Reactor and its implication.....	49
5.3 Reagents and materials.....	49
5.4 Synthesis Procedure.....	50
5.4.1 Microwave-assisted synthesis.....	50
5.4.2 Solvothermal synthesis.....	51
5.5 Role of surfactants and capping agents in coating mechanism....	52
<b>Results and Discussion</b>	
5.6 X-ray diffraction (XRD) & Williamson-Hall analysis.....	54
5.7 Dynamic light scattering (DLS) & Zeta potential (ZP).....	55
5.8 Electron microscopy (FE-SEM and HR-TEM).....	57
5.9 Fourier-transform infrared (FT-IR) spectroscopy.....	63
5.10 Thermogravimetric Analysis (TGA) & Difference Thermogravimetry (DTG).....	64
5.11 X-ray photoelectron spectroscopy (XPS).....	65
5.12. UV-Vis-NIR Spectroscopy.....	67

## **Chapter-6 Self-poled Fe<sub>3</sub>O<sub>4</sub>/PVDF composites for piezoelectric nanogenerator applications**

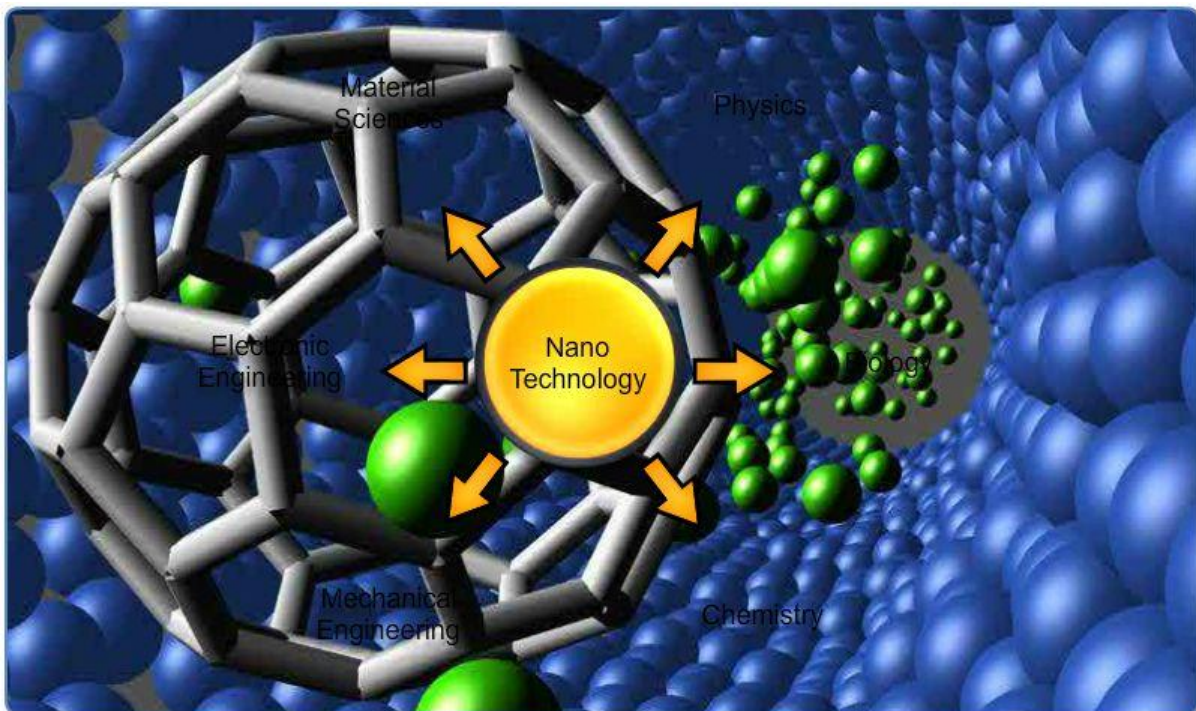
6.1 Introduction and Objective.....	76
6.2 Fabrication of self-poled standalone Fe <sub>3</sub> O <sub>4</sub> /PVDF Composite Nano generators.....	77
6.3 Basic Characterization.....	77
6.4 Piezo performance.....	79
6.5 Discussion and Conclusion.....	81
6.6 Reference.....	82

## **Chapter-7 Grand Conclusion**

7.1 Grand Conclusion.....	84
---------------------------	----

# ***CHAPTER 1***

## ***Introduction to Nano Science and Technology***



## 1.1 Definition

Nanotechnology is the creation of useful or functional materials, devices and systems through control of matter on the nanometre length scale and exploitation of novel phenomena and properties which arise because of the nanometre length scale. Nanotechnology includes the synthesis, characterization, exploration and utilization of nanostructured materials. The nanostructured materials are very interesting materials both for scientific reasons and practical applications.

## 1.2 History and fundamentals of nanotechnology

Although some aspects of Nanoscience has been known to some ancient cultures for centuries, eg., ancient Indian swords have been found to contain Carbon Nano tubes and carbon fibres, which is why they were renowned in the whole world, the modern craze for study of the nanometre dimensions began after Dr. Richard Feynman's famous speech on the 29th of December 1959 at the American Physical Society, titled, "*There is plenty of room at the bottom*".

In his speech Feynman discussed the importance "of manipulating and controlling things on a small scale" saying that "The principles of physics, as far as I can see, do not speak against the possibility of maneuvering things atom by atom" and how they could "tell us much of great interest about the strange phenomena that occur in complex situations."

He described how physical phenomena change their manifestation depending on scale, and posed two challenges: the creation of a nanometre, and the scaling down of letters to the size that would allow the whole Encyclopaedia Britannica to fit on the head of a pin. At that time,

Feynman's words were received as pure science fiction. Today, we have instruments that allow precisely what Feynman had predicted: creating structures by moving atoms individually.

The term 'nanotechnology' was used first by the Japanese scientists Norio Taniguchi (1912-1999) in a 1974 paper on production technology that creates objects and features on the order of a nanometer. Inspired by Feynman's concepts, The American engineer K. Eric Drexler independently used the term "nanotechnology" in his 1986 book "Engines of Creation: The Coming Era of Nanotechnology", which proposed the idea of a nanoscale "assembler" which would be able to build a copy of itself and of other items of arbitrary complexity with atomic control. Also in 1986, Drexler co-founded The Foresight Institute (with which he is no longer affiliated) to help increase public awareness and understanding of nanotechnology concepts and implications.

Thus, emergence of nanotechnology as a field in the 1980s occurred through convergence of Drexler's theoretical and public work, which developed and popularized a conceptual framework for nanotechnology, and high visibility experimental advances that drew additional wide scale attention to the prospects of atomic control of matter.

The invention of scanning tunnelling microscope in the 1980s by IBM Zurich Scientists and then the atomic force microscope allowed scientists to see materials at an unprecedented atomic level. The microscope's developers Gerd Binnig and Heinrich Rohrer at IBM Zurich Research Laboratory received a Nobel Prize in Physics in 1986. Significant progress was obtained by IBM in 1990 when a team of physicists had spelled out the letters "IBM" using 35 individual atoms of xenon. Another breakthrough came in 1985 with the discovery of new shapes for molecules of carbon, known as the Bucky ball, which are round and consist of 60 carbon atoms. This led to the discovery of a related molecular shape known as the carbon

nanotube in 1991. Carbon nanotubes are still one of the most promising areas of nanotechnology as they are about 100 times stronger than steel but just a sixth of the weight; they have unusual heat and conductivity characteristics. In parallel, studies of semiconductor nanocrystals led to the development of quantum dots, whose properties are between those of bulk semiconductors and discrete molecules. The major focus of research across the world continues to be research on nanoscale properties, synthesis of materials and characterization, and application development to create useful devices and processes and reap economic benefits.

Nanotechnology is an emerging interdisciplinary technology that has been booming in many areas during the recent decade, including material science, mechanics, electronics, optics, medicine, plastics, energy electronics and aerospace. The “Nano” in Nanotechnology comes from the Greek word “Nanos” that means dwarf. Scientists use this prefix to indicate  $10^{-9}$  or one billionth. One nanometer is one billionth meter that is about 10000 times smaller than the diameter of a single human hair. Nano technology endeavours are aimed at manipulating atoms, molecules and Nano size particles in a precise and controlled manner in order to build materials with a fundamentally new organization and novel properties.

Nanotechnology is called a “bottom up” technology by which bulk materials can be built precisely in tiny building blocks. Therefore, resultant materials have fewer defects and higher quality.

The fundamentals of nanotechnology lie in the fact that properties of substances dramatically change when their size is reduced to the nanometer range. When a bulk material is divided into small size particles with one or more dimension (length, width or thickness) in the nanometer range or even smaller, the individual particles exhibit unexpected properties, different from



those of the bulk materials. Bulk materials possess continuous physical properties. The same applied to macro sized materials also. But when particles assume nanoscale dimension, the principles of classical mechanics are no longer capable of describing their behaviour (movement, energy, etc.). At these dimensions principles of quantum mechanics apply. The same material at the nanoscale can therefore have properties (eg. Optical, mechanical, electrical, etc.) Which are very different from (even opposite to) the properties the material has at the macro scale (bulk).

The field of nanotechnology, in general, is loosely divided into four subareas:

- Micro and Nano instruments
- Nano electronics
- Nano Biosystems and
- Nano engineered materials

The first addresses some of the most far reaching yet practical applications of miniature instruments for measuring atoms or molecules in chemical, clinical, or biochemical analysis; in biotechnology for agent detection; and environmental analysis.

The second category, Nano electronics concerns the development of systems and materials required for the electronics industry to go beyond current technological limits producing even finer details than features in a high performance microprocessor chip along with a new generation of electronics based on plastics, which is expected to create new markets with applications ranging from smart cards to tube like computers.

The third class, Nano Biosystems can be described as molecular manipulation of biomaterials and the associated miniaturization of analytical devices such as DNA, peptide, protein, and cell chips.

The last sub area, Nano engineered materials looks at several classes of advanced materials including nanocrystal line materials and Nano powders used in electronics and photonics applications, as catalysts in automobiles, in the food and pharmaceutical industries, as membranes for fuel cells, and for industrial scale polymers. Nanotechnology engineering is a multidisciplinary engineering field, which simultaneously draws from and benefits areas such as material science and engineering, chemistry, physics and biology. Indeed, it is all about generating new solutions based on atomic and molecular scale manipulations. Nano electronic devices based on new nanomaterials systems and new device structures will contribute to the development of next generation of microelectronics.

For example, single electron transistor and field effect transistor based on single wall carbon nanotubes are already on the way. Another very important aspect of nanotechnology is the miniaturization of current and new instruments, sensors and machines that will greatly impact the world we live in. Examples of possible miniaturization are computers with infinitely great power that compute algorithms to mimic human brains, biosensors that warn us at the early stage of the onset of disease and preferably at the molecular level and target specific drugs that automatically attack the diseased cells on site, Nano robots that can repair internal damage and remove chemical toxins in human bodies, and nanoscale electronics that constantly monitor our local environment. Further, nanotechnology was also expanded extensively to other fields due to the novel properties of nanomaterials discovered and to be discovered.

For example, nanowires can be potentially used in Nano photonics, laser, Nano electronics, solar cells, resonators and high sensitivity sensors. Nanoparticles can be potentially used in catalysts, functional coatings, Nano electronics, energy storage, drug delivery and biomedicines. Nanostructured thin films can be used in light emitting devices, displays and high efficiency photovoltaics.

These are only a limited part of the fast developing nanotechnology, yet numerous of other Potential applications of nanomaterials have already been or will be discovered. Nanotechnology is an interdisciplinary research field in which many physicists, chemists, biologists, materials scientist and other specialists are involved. Therefore it requires formation and contribution from multidisciplinary teams of physicists, chemists, materials scientists, engineers, molecular biologists, pharmacologists and others to work together on

- Synthesis and processing of nanomaterials and nanostructures, understanding the Physical properties related to the nanometer scale,
- Design and fabrication of Nano devices or devices with nanomaterials as building Blocks, and
- Design and construction of novel tools for characterization of nanostructures and Nanomaterials.

Synthesis and processing of nanomaterials and nanostructures are the essential aspect of nanotechnology. Studies on new physical properties and applications of nanomaterials and nanostructures are possible only when nanostructured materials are made available with desired size, morphology, crystal and microstructure and chemical composition.

Nanotechnology is considered by some to be the next industrial revolution and is believed to cause enormous impacts on the society, economy and life in general in the future.

### 1.3 Current status and trends

Nanotechnology is considered to be the technology of the future; it is perhaps today's most advanced manufacturing technology and has been called "extreme technology", because it reaches the theoretical limit of accuracy which is the size of a molecule or atom. In manufacturing industry, two interrelated trends are clearly seen: the trend towards miniaturisation and the trend towards ultra-precision processing. Both trends are moving in the direction of nanotechnology, because both are tending to dimensions which lie in the range of several nanometres.

Nanotechnology deals with materials and systems having the following key properties

- They have at least one dimension of about 1–100 nm;
- They are designed through processes that exhibit fundamental control over the physical and chemical attributes of molecular-scale structures.
- They can be combined to form larger structures.

Nanoscience and nanotechnology are fields that are still in their early stages. Envisioned to change almost everything about how we manufacture and approach technology, it is a technological development that is well anticipated and significantly hyped. The current explosion of interest in the field began with the characterization of carbon based nanotubes in 1990. This discovery set off a flurry of study on other one dimensional nanostructures, materials that have one growth direction that is significantly faster than all other growth directions. Here the other two directions are confined to the nanoscale range. Examples of one

dimensional nanostructure include nanotubes, nanowires, nanobelts, and nanorods. Two dimensional nanostructures have two fast growth directions, so that only one direction is contained to nanoscale dimensions. Examples of these include Nano sheets and self-assembled monolayers. Zero dimensional nanostructures have all directions confined to nanoscale dimensions. These include quantum dots and nanoparticles. These materials exhibit significantly enhanced or altered properties as they are confined to the Nano scale. Because of this change in properties, developing control over these materials has been the significant thrust of research in nanotechnology for the past few decades. The basic physical and chemical concepts that govern the interactions at play with nanotechnology are not fully understood. This is why a bulk of the research aims at discovering novel properties, unique structures and morphologies, or basic commercial device fabrication using nanostructures.

High temperature structural and functional ceramics offer great promise in diverse applications ranging from gas turbines and aircraft engines, refractory components, Membranes and filters, to piezoelectric actuators, fuel cells, and electronic devices High performance applications, such as rotating hot gas path components, require ceramics that combine strength, toughness, creep resistance, and thermal stability unfortunately, this combination is not readily available in any generation of monolithic ceramic materials. For example, silicon carbide and silicon nitride have excellent stability at high temperature, but they lack the required fracture toughness. The first step toward enhancing these properties was the development of ceramic matrix composites, which are now being tested in hot gas path components. Modelling suggests that the mechanical properties of ceramic materials are expected to improve dramatically through the synthesis of hierarchical structures with nanoscale order.

When measuring properties of a material on a nanoscale, there is a strong correlation between the dimensionality of the material and the physical or chemical properties. For example, a small change in the size of quantum dots (~ 5 nm) can shift their luminescence from the red end of the visible light spectrum to the blue end. Therefore, the precision required controlling the dimensionality within a few nanometres or less is necessary for the development and use of nanomaterials.

Nanotechnologies have the potential to provide society with great benefits. Many products or services our industry currently insures will be adapted to contain such technology in future. An environment of such innovation is to be encouraged and has certainly led to many improvements in the past.

## 1.4 Future of Nano Technology

After the discovery of the fullerene, physicists were only speculating the possibility of transistors the size of single molecules. The discovery of graphene changed all that, because that speculation is now a certain reality. But the factors that have been holding us back is the quantum effects that take over once the dimension goes in the order of 10 nm, At those levels, bulk properties of the material are no longer valid. The current models of Intel CPUs consist of multiple cores of processors made up of transistors of the order of 14 nm.

Researchers at Intel and other Silicon Valley chip makers are currently working towards scaling down further to 7nm. But we can only scale down so much.

Economics plays a major role here, in deciding whether we keep scaling down or develop something new that will take over from Si based technologies. We will keep scaling down that we have currently, till it is profitable and possible. **Moore's law**, as the prediction of Gordon Moore is famously known, is already being pushed to the limits. There is more CMOS per square cm than Mr. Moore himself could have ever imagined.

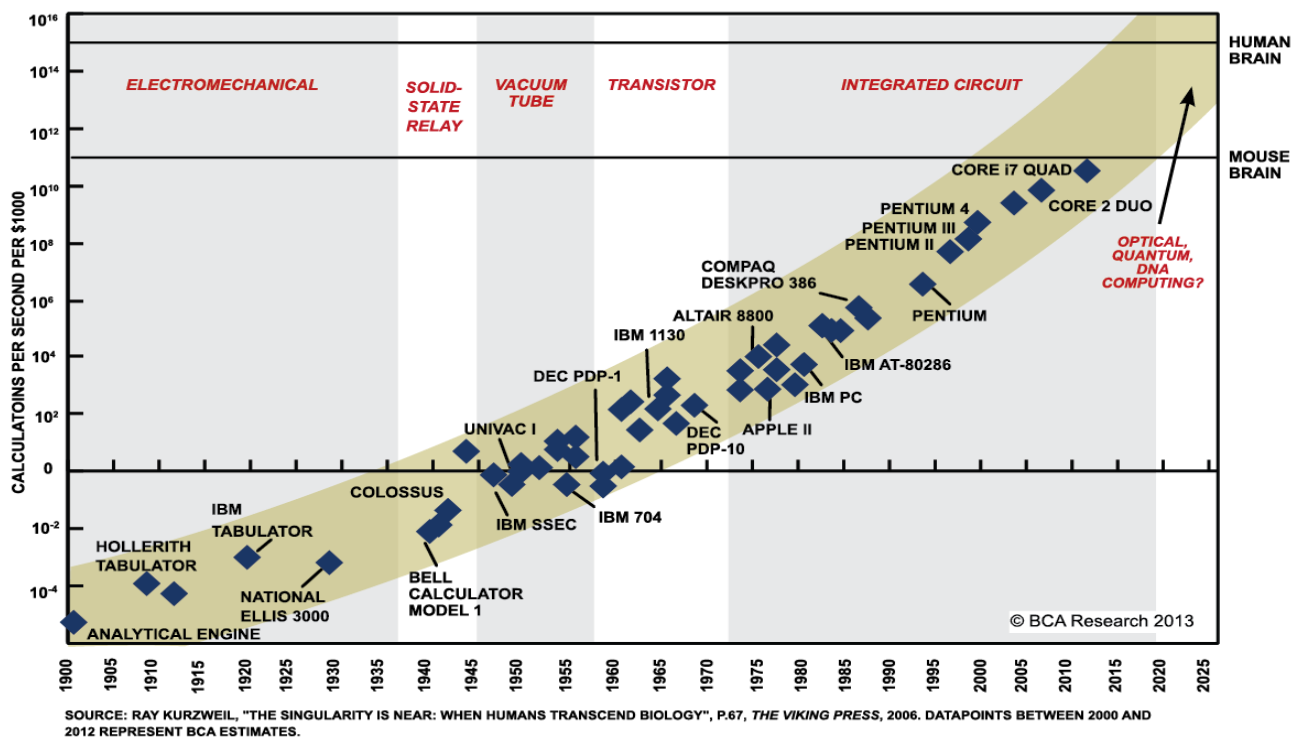


**Fig.1.1** The improvement in switching speeds of Si based processors over the years.

## 1.5 Applications of Nanotechnology

Nano technological application is extended in different field of research with various unique applications. When a particle is shrunk to Nano-scale, several properties of the material change in accordance with size. So it gives new applications in several fields. As due to the size the surface to volume ratio increases, it gives more surface area to react. Several optical as well as mechanical properties are also dependent on the diameter or the size of particles.

Nanotechnology has innumerable applications in variety of diverse fields all of which are interconnected with each other. The modern world has burgeoned in a consequential extent with the advent of newer technologies based on Nano science. The applications include nanoscale patterning of electronic circuits, high density data storage, quantum computers, fuel cell catalysts, environmental catalysts, industrial catalysts, waste water treatment, functional

nanocomposites, food packaging, food processing catalysts, hydrogen production photo catalysts, automotive catalysts, fuel additive catalysts, lithium ion battery electrodes, natural or synthetic polymer hybrid fibres, reinforced plastics, controlled drug release, cancer therapy, drug delivery, bio imaging, bio markers, hyper thermic treatment, MRI contrast agents, IR contrast agents, ultra violet protection like sunscreens, antioxidants, ultra violet blocking coatings, water resistant coatings, gas barrier coatings, anti-microbial coatings, self-cleaning building surface, food quality and safety analysis sensors, chemical sensors, gas sensors, high sensitive sensors, pollution monitoring sensors, functional nanocomposites, Nano pigments, super thermal-conductive liquid, Nano phosphors for display, super plastic ceramics, transparent conductive polymer films, chemical mechanical planarization, nano inks, single electron transistors, quantum lasers, high power magnets, pollutant scavengers, interactive food, nutraceutical, fungicides and pesticides, medical textiles, technical textiles, heat retaining textiles, self-cleaning textiles, anti-stain textiles, electro-conducting textiles, ultra violet blocking textiles, wound dressing, dental ceramics, bone growth, tissue cells engineering, molecular tagging, dye sensitized solar cells, paint-on solar cells, hydrogen storage materials, bio-composites, Ferro-fluids, refractive index engineering, aerospace engineering and many others.

Detail applications in some important fields are given below:

### **1.5.1 Nanotechnology in Health and Medicine:**

Nanotechnology has a high impact on the research and applications related to biology and medicine. Nano-drug delivery is the safest procedure for medication because small quantity of nanomaterial can help to recover with reducing side effects. Nano medicine has also the potential to enable early detection and prevention, and to essentially improve diagnosis, treatment and follow-up of diseases with the help of bio-sensors[5].



- (1) Carbon nanotubes have promising application for the development of advanced biosensors with novel features.
- (2) CNT, though inert, can be functionalized at the tip with a probe molecule. Their study uses AFM as an experimental platform.
  - i. Leukaemia cells identification
  - ii. Catheter development.
- (3) Nano devices can make gene sequencing more efficient.
- (4) Tissue engineering makes use of artificially stimulated cell which can help in transplantation of organs or artificial implants
- (5) The technology is also being used to develop sensors for cancer diagnostics.

### **1.5.2 Nanotechnology in Defence and Security:**

Nanotechnology will lead to higher protection, more lethality, longer endurance and better self-supporting capacities of future combat soldiers. Substantial advantages are expected to be gained which include threat detection, novel electronic display and interface systems, as well as a pivotal role for the development of miniaturised unmanned combat vehicles and robotics. Nanotechnology will also enable small portable sensor systems capable of identifying chemical, biological and nuclear, radiation, or explosive threats.

### **1.5.3 Nanotechnology in Information & Communication:**

Electronic memory designs in the past have largely relied on the formation of transistors. The miniaturization of electronic industry has been the driving force behind the rapid research and development of Nano science and technology. Continuing to shrink silicon chips is getting expensive and difficult. Chips built using the molecular transistors are the industry's best hope for building faster, cheaper computers well into this century. "With the electronics we're talking about, we're going to make a computer that doesn't just fit in your wristwatch, not just in a

button on your shirt, but in one of the fibres of your shirt," says Philip Kuekes, a computer architect at Hewlett-Packard Laboratories. According to the manufacturers, NRAM (Nanotube-based/Non-volatile random access memory) is a universal memory chip suitable for countless existing and new applications in the field of electronics. In the modern communication technology traditional analog electrical devices are increasingly replaced by optical or optoelectronic devices due to their enormous bandwidth and capacity. Two promising examples are photonic crystals and quantum dots. Quantum dots are nanoscale objects, which can be used for the construction of lasers. The advantage of a quantum dot laser over the traditional semiconductor laser is that their emitted wavelength depends on the diameter of the dot. Quantum dot lasers are cheaper and offer a higher beam quality than conventional laser diodes.

#### **1.5.4 Nanotechnology in Energy and Environment:**

Energy crisis and environmental pollution in present days have severe negative impact in human life. To provide sufficient energy to the developing world, nanotechnology is the key factor because less expensive improved energy can be produced through suitable nanomaterial. Recent nanotechnology projects to diminish the energy crisis is related to the parameters like storage, conversion, sufficient super capacitance and recyclability production with the help of small amount of nanomaterial, thermal insulation increment etc. Energy application with the help of nanomaterial:

- (1) Fuel cell (e.g. CNT) for hydrogen storage and related automobile applications.
- (2) Cheap, light weight and more efficient metal oxide nanomaterial photovoltaic application for the purpose of water splitting and efficient dye sensitized solar cell.
- (3) Nanotechnology can be used to the further reduction of combustion engine pollutants by nonporous filters; this can clean the exhaust mechanically.

- (4) Nanotechnology in water disinfection with the help of nanostructured photosensitized catalyst and further step towards environmental safe and green technologies.
- (5) Solid state lightening is a powerful tool to reduce total electricity consumption by 10% and cut carbon emission by the equivalent of 28 million tons/year.

## 1.6 References

- [1] Nanostructures and Nanomaterials by G. Cao
- [2] [www.aps.org](http://www.aps.org)
- [3] [www.intel.com](http://www.intel.com)
- [4] [www.graphene.manchester.ac.uk](http://www.graphene.manchester.ac.uk)

# **CHAPTER 2**

## **Introduction To Magnetite( $\text{Fe}_3\text{O}_4$ )**

## 2.1 Overview

The oldest known magnetic material Magnetite ( $\text{Fe}_3\text{O}_4$ ) has attracted much attention in the last decade due to the recent understandings of charge-ordering phenomena in low-temperature symmetries during Verwey transition and associated relaxor properties along with uncountable potential biomedical applications such as biomolecular separation, biological sensing & cell tracking, targeted drug delivery, magnetic fluid hyperthermia (MFH) treatment of tumour cells, gene delivery, waste water purification, environmental remediation, nickel-ion batteries and magnetic resonance imaging (MRI) as  $T_2$  contrast agents[2],[14],[13]. Among various magnetic materials,  $\text{Fe}_3\text{O}_4$  NP's have been extensively investigated due to their excellent biocompatibility, negligible toxicity and tunable magnetic property. For spherical particles, the surface area to volume ratio is inversely proportional to the radius, so a substantial reduction in particle size leads to a dramatic increase in surface area and thereby the surface-energy term and associated defect-states; giving rise to certain physio-chemical properties.

There exists roughly 16 different iron oxide & oxyhydroxide polymorphs having a wide range of properties and performance in various environment. Among these, three most common and important iron oxide polymorphs are hematite ( $\alpha\text{-Fe}_2\text{O}_3$ ), maghemite ( $\gamma\text{-Fe}_2\text{O}_3$ ), and magnetite ( $\text{Fe}_3\text{O}_4$ ). Magnetite NP's exhibit unique size-dependent magnetic properties. Bulk magnetite crystallizes in the inverse cubic-spinel structure  $(\text{Fe}^{3+})_A[\text{Fe}^{2+}\text{Fe}^{3+}]_B(\text{O}^{2-})_4$ ; space group  $O_h^7$  ( $Fd\bar{3}m$ ) and lattice parameter  $a_c = 8.407 \text{ \AA}$ , which consists of face-centred cubic (FCC) close-packed lattice of  $\text{O}^{2-}$  ions. Magnetite possesses a smaller unit cell than hematite and is free of vacancies unlike maghemite. There are two types of Fe atoms: the tetrahedrally coordinated A-sites (Wyckoff site 8a, point group  $\bar{4}3m$ ) and the octahedrally coordinated B-sites (Wyckoff site 16d, point group  $\bar{3}m$ ) with respect to the oxygen sublattice. Rapid hopping of an extra down-spin electron between B sites results in minority-spin-polarized electronic conductivity ascribing its half-metallic behaviour at room-temperature. In fact,  $\text{Fe}_3\text{O}_4$  possesses a conducting minority spin channel and semiconducting majority spin channel, which results an absolute spin polarization at the Fermi level, making magnetite a prospective material for spintronic devices too.

## 2.2 Crystal Structure

Magnetite ( $\text{Fe}_3\text{O}_4$ ) is the prototype of the class of ferrites which has the spinel structure. This structure crystallizes in cubic system, the unit cell containing eight formula units of the molecule  $\text{MeFe}_2\text{O}_4$ ; here Me stands for a divalent metal ion (generally 0.5-1.0 Å ionic radius, e.g, Mn, Co, Ni,Cu) which in the case of  $\text{Fe}_3\text{O}_4$  is the ion  $\text{Fe}^{2+}$ . The other iron ions in the formula are  $\text{Fe}^{3+}$ . The extensive x-ray investigations have revealed that the  $\text{O}^{2-}$  ions form an f.c.c close packed lattice while the 8 divalent and 16 trivalent ions are distributed over available tetrahedral and octahedral interstitials (64 and 32 sites per unit cell respectively).[3] From a plan of view of the structure it is seen that the tetrahedral ions (on A sites) have 4 nearest  $\text{O}^{2-}$  neighbours, while the octahedral ions (on B sites) have 6 nearest  $\text{O}^{2-}$  neighbours. The structure may also be described as that of diamond lattice if each carbon atom is replaced by a  $\text{Fe}_3\text{O}_4$  molecule.[5],[7]

## 2.3 Magnetic Properties

Basically, magnetic properties of bulk magnetite with a multidomain structure are governed by two distinct mechanisms. The first is the anti-ferrimagnetic super-exchange interaction between the  $\text{Fe}_{Oct}^{3+}$  and  $\text{Fe}_{Tet}^{3+}$  sites coupling through the overlapping 2p orbital of intermediate oxygen.[11] Association of B-sites in a pyrochlore lattice with corner-sharing tetrahedra gives rise to a magnetic moment antiparallely aligned with A-sites having unequal magnitude. The second factor is the predominant double-exchange interaction between the  $\text{Fe}_{Oct}^{2+}$  and  $\text{Fe}_{Oct}^{3+}$  sites via hopping of spin-down electrons, which makes them align parallel. Therefore, all the  $\text{Fe}_{Oct}^{2+}$  ions contribute to the magnetic moment, while all  $\text{Fe}^{3+}$  ions cancel each other out.[9] In fact, there are twice as many B-site  $\text{Fe}^{3+} 3d^5$  ( $S = 5/2$ ) up-spins as there are down-spins at the A-sites, resulting a net non-vanishing magnetic moment, giving rise to ferrimagnetism with a Curie temperature of 858 K.

As the particle-size decreases below ~100 nm, the particles tend to attain a single-domain structure, where coercivity is maximized and Curie temperature gets lowered. When the particle size is smaller than ~20 nm, the magnetization of magnetite NP's is randomized by thermal agitation. As a consequence, they become superparamagnetic with only 2 stable orientations. The temperature below which a particle becomes superparamagnetic i.e., attains a steeper magnetization curve with large susceptibility and zero hysteresis area, is called the

blocking temperature ( $T_B$ ) and can be calculated from  $T_B = KV/25k_B$ , where  $K$  is the magnetic anisotropy energy density,  $k_B$  is the Boltzmann constant, and  $V$  is the average volume of the NP's. NP's with sizes of 3–100 nm have garnered a great deal of attention from the perspective of both basic and developmental sciences in a distinct variety of fields. This is due to the fact that these NP's exhibit size-dependent electrical, optical, magnetic, and catalytic phenomena that cannot be realized by their bulk counterparts.[5],[8]

## 2.4 Low Temperature Phase Transition

There is abundant experimental evidence that  $Fe_3O_4$  undergoes a phase transition in the neighbourhood of 120K that is not observed in the other ferrites with similar structure. Changes in the following physical properties suggest that the transition can be related to an ordering phenomenon.[10] However it has not yet been clearly established whether the transition is of the first or second order, and an attempt to classify made on the basis of these observations

Electrical resistivity measurement of pure synthetic single crystals of  $Fe_3O_4$  on cooling through the transition region revealed that it increases by a factor of 90 at 115K in a temperature interval of 1K

Magnetic properties measurements for both natural and synthetic crystals indicate that the magnetism undergoes a sharp discontinuity at 120K, which in most case is confined to a region 2-4K wide. The initial permeability has an equally sharp transition here.[3]

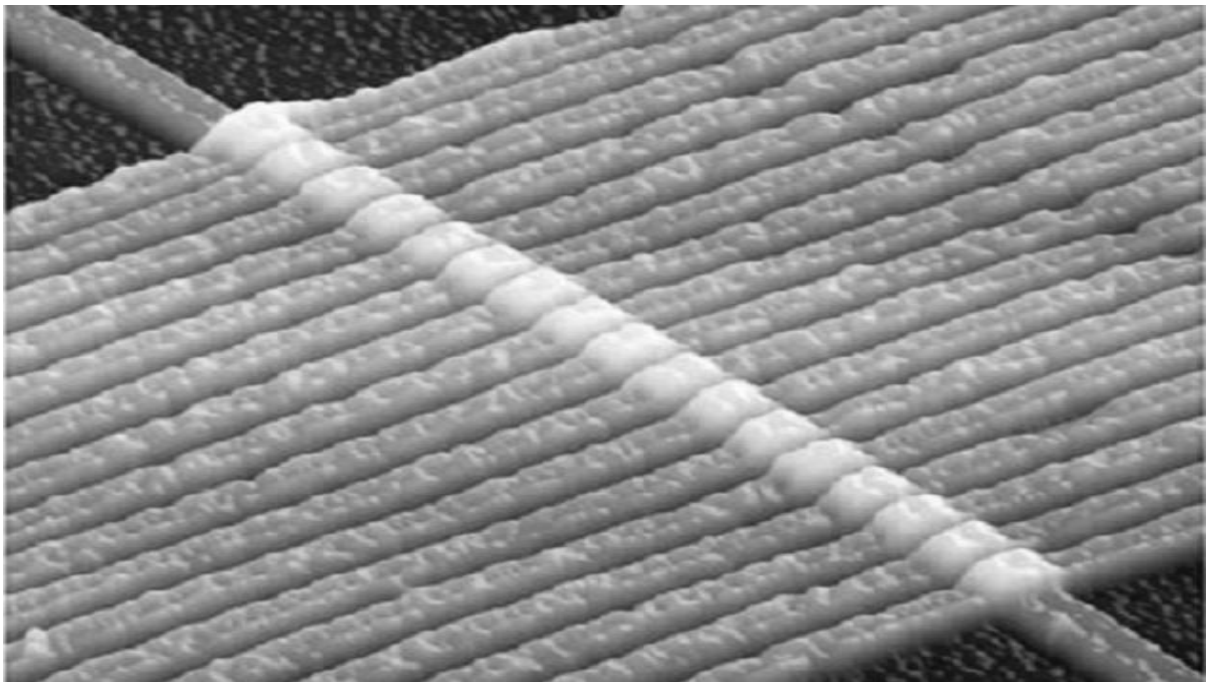
## 2.5 Reference

- [1] S. A. Wolf, D. D. Awschalom, R. A. Buhrman, J. M. Daughton, S. von Molnár, M. L. Roukes, A. Y. Chtchelkanova, and D. M. Treger, *Science* **294**, 1488 (2001).
- [2] J. J. Versluijs, M. A. Bari, J. M. D. Coey, *Phys. Rev. Lett.* **87**, 026601 (2001).
- [3] Zutic J. Fabian, and S. Das Sarma, *Rev. Mod. Phys.* **76**, 323 (2004).
- [4] E. J. W. Verwey *Nature* **144**, 327 (1939).
- [5] D. T. Margulies, F. T. Parker, M. L. Rudee, F. E. Spada, J. N. Chapman, P. R. Aitchison, and A. E. Berkowitz, *Phys. Rev. Lett.* **79**, 5162 (1997).
- [6] S. K. Arora, R. G. S. Sofin, and I. V. Shvets *Phys. Rev.* **B 72**, 134404 (2005).
- [7] W. Eerenstein, T. T. M. Palstra, S. S. Saxena, and T. Hibma, *Phys. Rev. Lett.* **88**, 247204 (2002).
- [8] S. Kale, S. M. Bhagat, S. E. Lofland, T. Scabarozzi, S. B. Ogale, A. Orozco, S. R. Shinde, and T. Venkatesan and B. Hannoyer, *Phys Rev* **B 64**, 205413 (2001).
- [9] D. M. Phase, Shailja Tiwari, Ram Prakash, Aditi Dubey, V. G. Sathe and R. J. Choudhary, *J. Appl. Phys.* **100**, 123703 (2006).
- [10] S. B. Ogale, K. Ghosh, R. P. Shrama, R. L. Greene, R. Ramesh, and T. Venkatesan. *Phys. Rev.* **B 57**, 7823(1998).
- [11] S. Tiwari, R. J. Choudhary, Ram Prakash, and D. M. Phase, *J. Phys. Cond. Mat.* **19**, 176002 (2007).
- [12] Y.X. Lu, J.S. Claydon and Y.B. Xu, *Phys. Rev. B* **70**, 233304 (2004).
- [13] S. M. Watts, C. Boothnan, S. van Dijken and J.M.D. Coey, *Appl. Phys. Lett.* **86**, 212108 (2005).
- [14] S. M. Watts, C. Boothnan, S. van Dijken and J.M.D. Coey, *J. Appl. Phys.* **95**, 7465 (2004).



# **CHAPTER 3**

## ***Review of past work***



## 3.1 Introduction

Extensive literature survey reveals a wide variety of bottom-up magnetite synthesis methods including co-precipitation, sol-gel technique, one-pot synthesis with reflux or hot-injection method in inert condition, electrochemical, solvothermal or hydrothermal, reduction followed by microwave irradiation, thermal decomposition of iron (III) acetylacetonate in polyol medium etc. Use of different bases, reducing and capping agents such as NaOH, KOH, NaBH<sub>4</sub>, N(CH<sub>3</sub>)<sub>4</sub>OH, sodium oleate, PEG, PVA, PVP etc have been reported previously. The effect of size, shape, morphology and surface functionalization in different physio-chemical properties have been thoroughly scrutinized by many researchers [References].[10][5]

Polyol-mediated synthesis is a versatile chemical approach to prepare high-quality water-stable Fe<sub>3</sub>O<sub>4</sub> NP's. In this method; an even mixture of ethylene glycol (EG), diethylene glycol (DEG), triethylene glycol (TREG), tetraethylene glycol (TEG) and polyethylene glycol (PEG) of different molecular weights often act as a high-boiling point solvent cum reductant, as well as a stabilizer to control the particle growth and morphology and thereby prevents interparticle aggregation. Compared to the thermal decomposition method, Fe<sub>3</sub>O<sub>4</sub> NP's prepared by this route exhibit better stability and dispersibility in organic solvents due to polyol coating. However, such a coating is not covalently linked to the particle-surface and therefore achieves a relatively weak interaction with polyol-molecules. When these NP's are introduced inside a body, they usually exhibit poor stability due to the desorption of polyols, facilitating their aggregation and uptake by the macrophages. Considering these factors, long-term colloidal stability under physiological conditions is desired to overcome these problems. Biocompatible carboxylic acid salts with coating tendency can conquer this problem. Shen *et al.* have synthesized ultra-small, monodispersed and water-dispersible Fe<sub>3</sub>O<sub>4</sub> NP's by using disodium citrate as growth inhibitor cum stabilizer, whereas Wang *et al.* have produced smaller NP's via high-temperature precipitation approach using poly(acrylic acid) as a capping agent to control morphology. Jun *et al.* developed biocompatible Fe<sub>3</sub>O<sub>4</sub> nanocrystal line samples by using 2,3-dimercaptosuccinic acid (DMSA) as a capping ligand to study size-dependent magnetic properties for MFH & MRI-based applications.[9]

## 3.2 Controversy

$\text{Fe}_3\text{O}_4$  has been theoretically predicted to be a half-metallic ferrimagnetic material with a conductive minority spin channel and semiconducting majority spin channel which results in a 100% spin polarization at EF. This makes magnetite a prospective material for spintronic devices.[4][5][6]

The electronic band structure of  $\text{Fe}_3\text{O}_4$  films has been extensively investigated by means of x-ray magnetic circular dichroism, ultraviolet photoelectron spectroscopy, as well as spin- and angle-resolved photoelectron spectroscopy. Nevertheless, the interpretation of the valence-band photoemission spectra of  $\text{Fe}_3\text{O}_4$  has been and still is a matter of debate. Recent investigations, however, showed that band dispersions must be taken into account for the interpretation of photoelectron spectra of  $\text{Fe}_3\text{O}_4$ . [9]

## 3.3 Future

Biomedical applications, which mainly focus on the targeted anticancer drug delivery.  $\text{Fe}_3\text{O}_4$ -NPs have been studied and proved that  $\text{Fe}_3\text{O}_4$ -NPs can be used in various fields of application, due to “superparamagnetic” property that  $\text{Fe}_3\text{O}_4$ -NPs possessed. In targeted drug delivery system, drug loaded  $\text{Fe}_3\text{O}_4$ -NPs can accumulate at the tumor site by the aid of external magnetic field. This can increase the effectiveness of drug release to the tumor site and vanquish cancer cells without harming healthy cells. In order to apply  $\text{Fe}_3\text{O}_4$ -NPs in human body,  $\text{Fe}_3\text{O}_4$ -NPs have to be biocompatible and biodegradable to minimize the toxicity.[1]

Superparamagnetic nanoparticles is so famous nowadays because of the properties possessed, where the nanoparticles are magnetized up to their saturation magnetization when an external magnetic field is applied, yet they will not show any magnetic interaction once the magnetic field is eliminated. Surprisingly,  $\text{Fe}_3\text{O}_4$ -NPs exhibit this interesting behaviour too. Apart from that,  $\text{Fe}_3\text{O}_4$ -NPs are biocompatible, biodegradable and potentially non-toxic to human. These characteristics show a great potential of  $\text{Fe}_3\text{O}_4$ -NPs in future biomedical applications.[2][8]

## 3.4 Reference

- [1] Jeroen V D B and Khomskii D I 2008 J. Phys. : Condens.Matter 20 434217
- [2] Dmitry V E, Jeroen V D B and Khomskii D I 2004 Nature Mater. 3 853
- [3] Schrettle F, Krohns S, Lunkenheimer P, Brabers V and Loidl A 2011 Phys. Rev. B 83 195109
- [4] Ogale S B, Ghosh K, Sharma R P, Greene R L, Ramesh R and Venkatesan T 1998 Phys. Rev. B 57 7823
- [5] Gong G Q, Gupta A, Gang X, Qian W and Dravid V P 1997 Phys. Rev. B 56 5096
- [6] Park S K, Ishikawa T and Tokura Y 1998 Phys. Rev. B 58 3717
- [7] Ziese M and Blythe H J 2000 J. Phys. : Condens. Matter 12 13
- [8] Aragon R 1992 Phys. Rev. B 46 5328
- [9] Rozenberg G, Hearne G, Pasternak M, Metcalf P A and Honig J M 1996 Phys. Rev. B 53 6482
- [10] Cava R J, Fleming R M, Littlewood P, Rietman E A, Schneemeyer L F and Dunn R G 1984 Phys. Rev. B 30 3228

# **CHAPTER 4**

## ***Instruments and Apparatus***

## 4.1 X-ray Diffraction (XRD)

### 4.1.1 Basic Principle

X-ray Powder Diffraction (XRD) is an efficient analytical technique used for determination of grain size, composition of solid solution, lattice constants, and degree of crystallinity in a mixture of amorphous and crystalline substances. It is a common technique for the study of crystal structures, atomic spacing, crystallite sizes, stress analysis, lattice parameters, and quantitative phase analysis and can provide information on unit cell dimensions. This information is important for relating the production of a material to its structure and hence its properties.

X-ray diffraction is based on constructive interference of monochromatic X-rays and a crystalline sample. These X-rays are generated by a cathode ray tube, filtered to produce monochromatic radiation, collimated to concentrate, and directed toward the sample. The interaction of the incident rays with the sample produces constructive interference (and a diffracted ray) when conditions satisfy Bragg's Law ( $n\lambda = 2d \sin\theta$ ) as shown in **fig. 4.1**. These diffracted X-rays are then detected, processed and counted. By scanning the sample through a range of  $2\theta$  angles, all possible diffraction directions of the lattice should be attained due to the random orientation of the powdered material. Conversion of the diffraction peaks to d-spacings allows identification of the mineral because each mineral has a set of unique d-spacings. Typically, this is achieved by comparison of d-spacings with standard reference patterns i.e JCPDF files.

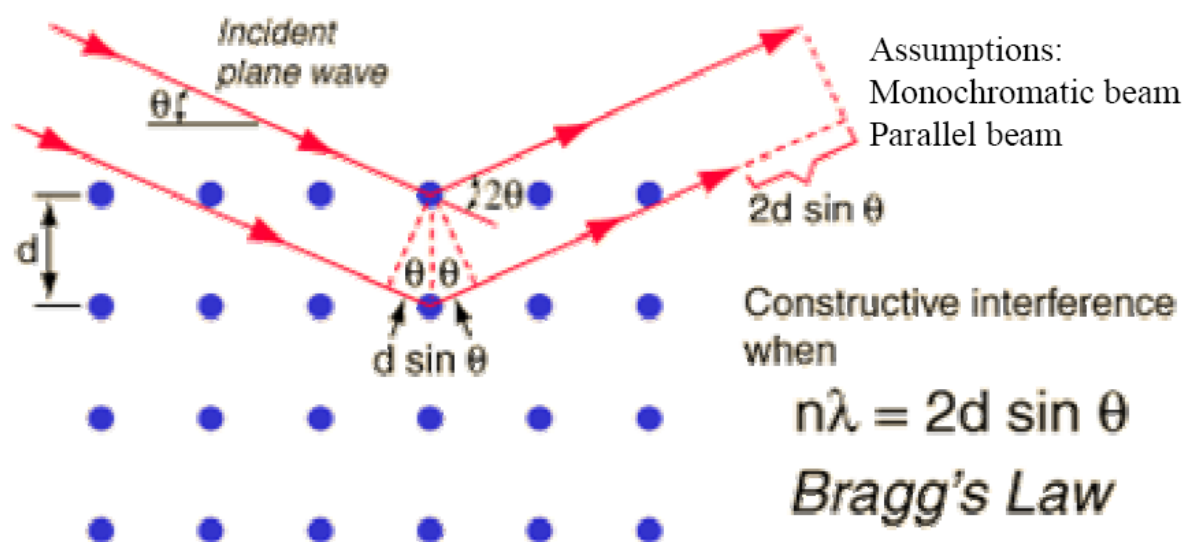


Fig 4.1 A schematic of Bragg's reflection from a crystal.

### 4.1.2 Experimental Set Up

X-ray diffractometers consists of three basic elements:

1. X-ray tube
2. Sample holder
3. X-ray detector.

X-rays are generated in a cathode ray tube by heating a filament to produce electrons, accelerating the electrons toward a target by applying a voltage, and bombarding the target material with electrons. When electrons have sufficient energy to dislodge inner shell electrons of the target material, characteristic X-ray spectra are produced. These spectra consist of several components, the most common being  $K\alpha$  and  $K\beta$ .  $K\alpha$  consists, in part, of  $K\alpha_1$  and  $K\alpha_2$ .  $K\alpha_1$  has a slightly shorter wavelength and twice the intensity as  $K\alpha_2$ . The specific wavelengths are characteristic of the target material (Cu, Fe, Mo, Cr). Filtering, by foils or crystal monochrometers, is required to produce monochromatic X-rays needed for diffraction.  $K\alpha_1$  and  $K\alpha_2$  are sufficiently close in wavelength such that a weighted average of the two is used. Copper is the most common target material for single-crystal diffraction, with  $CuK\alpha$  radiation =  $0.5418\text{\AA}$ . These X-rays are collimated and directed onto the sample. As the sample and detector are rotated, the intensity of the reflected X-rays is recorded. When the geometry of the incident X-rays impinging the sample satisfies the Bragg Equation, constructive interference occurs and a peak in intensity occurs. A detector records and processes this X-ray signal and converts the signal to a count rate which is then output to a device such as a printer or computer monitor. The geometry of an X-ray diffractometer is such that the sample rotates

in the path of the collimated X-ray beam at an angle  $\theta$  while the X-ray detector is mounted on an arm to collect the diffracted X-rays and rotates at an angle of  $2\theta$ .



**Fig 4.2** The X-ray diffractometer – Rigaku Ultima III.

## **4.2 Transmission Electron Microscopy (TEM)**

### **4.2.1 Basic Principle**

Transmission electron microscopy (TEM) is a technique used for analysing the morphology, defects, crystallographic structure, particle size and even composition of a specimen. In this technique a beam of electrons is transmitted through an ultra-thin specimen, interacting with the specimen as it passes through. An image is formed from the interaction of the electrons transmitted through the specimen; the image is magnified and focused onto an imaging device, such as a fluorescent screen, on a layer of photographic film, or to be detected by a sensor such as a CCD camera. The transmission electron microscope (TEM) operates on the same basic principles as the light microscope but uses electrons instead of light. What you can see with a light microscope is limited by the wavelength of light. TEM use electrons as "light source" and their much lower wavelength make it possible to get a resolution a thousand times better than with a light microscope.

TEMs are capable of imaging at a significantly higher resolution than light microscopes, owing to the small De Broglie wavelength of electrons. This enables the instrument's user to examine fine detail even as small as a single column of atoms, which is tens of thousands times smaller than the smallest resolvable object in a light microscope. TEM forms a major analysis method



in a range of scientific fields, in both physical and biological sciences. TEMs find application in cancer research, virology, materials science as well as pollution and semiconductor research. At smaller magnifications TEM image contrast is due to absorption of electrons in the material, due to the thickness and composition of the material. At higher magnifications complex wave interactions modulate the intensity of the image, requiring expert analysis of observed images. Alternate modes of use allow for the TEM to observe modulations in chemical identity, crystal orientation, electronic structure and sample induced electron phase shift as well as the regular absorption based imaging.

## 4.2.2 Experimental Set Up

TEM offers two methods of specimen observation as shown in **fig. 4.3**.

1. Image mode
2. Diffraction mode

In image mode, the condenser lens and aperture will control electron beam to hit the specimen, the transmitted beam will be focused and enlarged by objective and projector lens and form the image in the screen, with recognizable details related to the sample microstructure.

In diffraction mode, an electron diffraction pattern is obtained on the fluorescent screen, originating from the sample area illuminated by the electron beam. The diffraction pattern is entirely equivalent to an X-ray diffraction pattern. A single crystal will produce a spot pattern on the screen and polycrystalline will produce a powder or ring pattern. The microstructure, e.g. the grain size, and lattice defects are studied by use of the image mode, while the crystalline structure is studied by the diffraction mode.

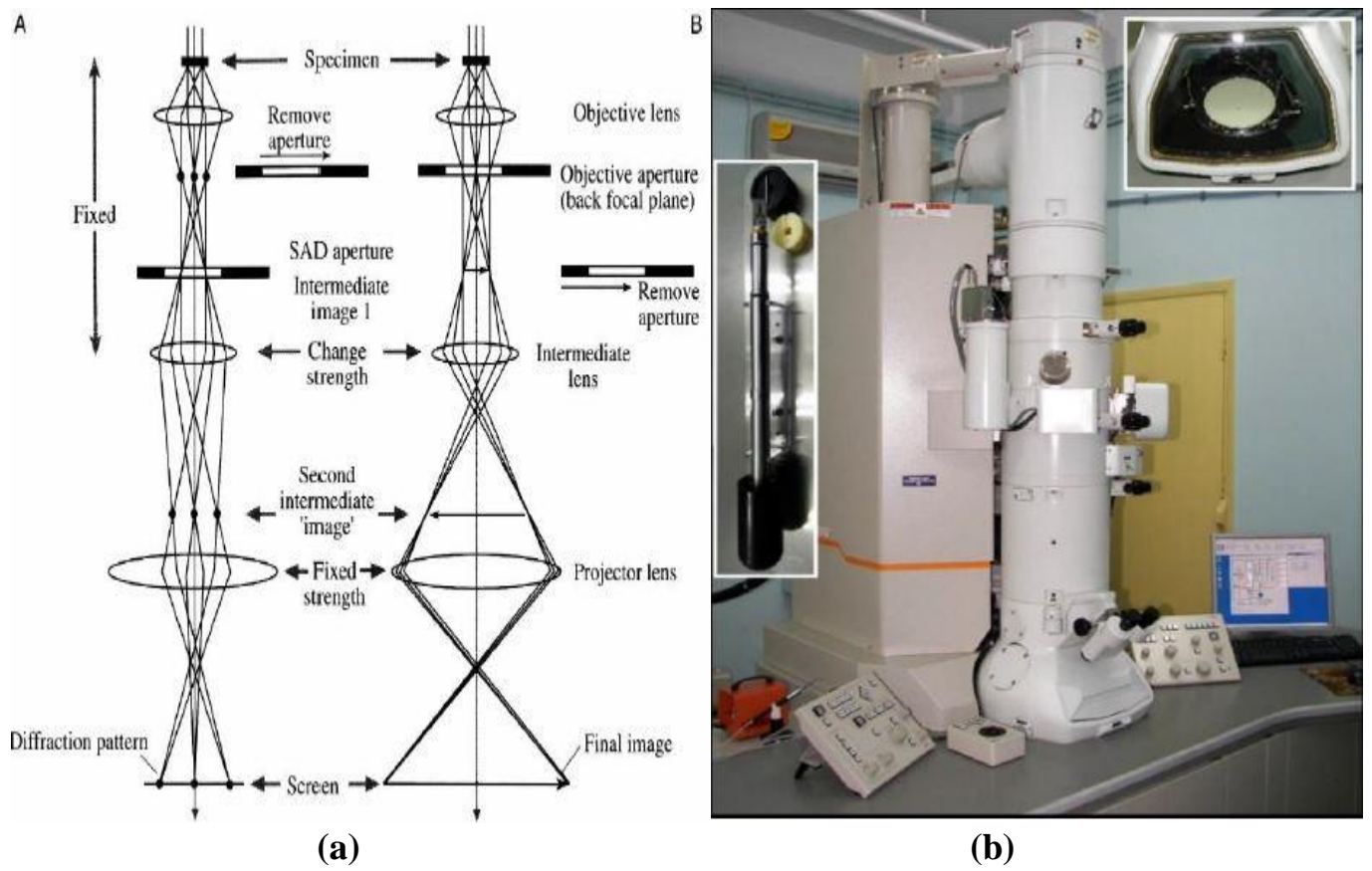


**Fig.4.3 (a)** Shows two different operations of TEM. **(b)** JEOL JEM-2100 HRTEM

## 4.3 UV–Vis–NIR Spectroscopy

### 4.3.1 Basic Principle

The instrument used in ultraviolet–visible spectroscopy is called a UV–Vis–NIR Spectrophotometer. Spectrophotometer provides a means for analysing liquids, gases and solids through the use of radiant energy in the far and near ultraviolet, visible and near infrared regions of the electromagnetic spectrum. Accordingly, the predetermined electromagnetic radiation wavelengths for ultra–violet (UV), visible (Vis) and near infra–red (NIR) radiation are defined as follows:

UV radiation: 300 to 400 nm

Vis radiation: 400 to 765 nm

NIR radiation: 765 to 3200 nm

The instrument operates by passing a beam of light through a sample and measuring wavelength of light reaching a detector. The wavelength gives valuable information about the chemical structure and the intensity is related to the number of molecules, means quantity or concentration. Analytical information can be revealed in terms of transmittance, absorbance or reflectance of energy in the wavelength range between 160 and 3500 mill microns.

Light is quantized into tiny packets called photons, the energy of which can be transferred to an electron upon collision. However, transfer occurs only when the energy level of the photon equals the energy required for the electron to get promoted onto the next energy state, for example from the ground state to the first excitation state. This process is the basis for absorption spectroscopy. Generally, light of a certain wavelength and energy is illuminated on the sample, which absorbs a certain amount of energy from the incident light. The energy of the light transmitted from the sample afterwards is measured using a photo detector, which registers the absorbance of the sample. A spectrum is a graphical representation of the amount of light absorbed or transmitted by matter as a function of wavelength. A UV–Vis–NIR spectrophotometer measures absorbance or transmittance from the UV range to which the human eye is not sensitive to the visible wavelength range to which the human eye is sensitive. Bouguer–Beer law as shown in **fig.4.4** is a basic principle of quantitative analysis, is also called the Lambert–Beer rule. The following relationship is established when light with intensity  $I_0$  is directed at a material and light with intensity  $I$  is transmitted.

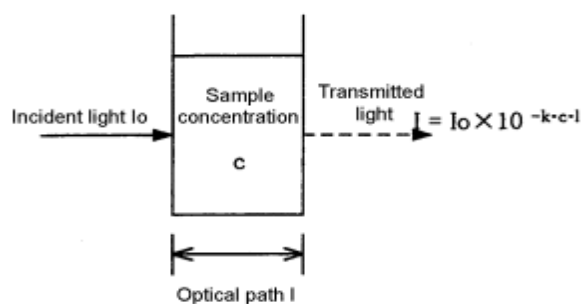


**Fig. 4.4** Bouguer–Beer Rule.

In this instance the value  $I/I_0$  is called transmittance ( $T$ ) and the value  $I/I_0 \times 100$  is called transmission rate ( $T\%$ ). The value  $\log(1/T) = \log(I_0/I)$  is called absorbance ( $Abs$ ).

$$T = I/I_0 = 10^{-kcl}$$

$$Abs = \log_{10}(1/T) = \log_{10}(I_0/I) = -kcl$$

Here  $k$  is proportionality constant and  $l$  = length of light path through the cuvette in cm. As can be seen from the above formulas, transmittance is not proportional to sample concentration. However, absorbance is proportional to sample concentration (Beer's law) along with optical path (Bouguer's law). In addition, when the optical path is 1cm and the concentration of the target component is 1 mol/l, the proportionality constant is called the molar absorption coefficient and expressed using the symbol  $\epsilon$ . The molar absorption coefficient is a characteristic value of a material under certain, specific conditions. Finally, stray light, generated light, scattered light, and reflected light must not be present in order for the Bouguer–Beer rule to apply.

### 4.3.2 Experimental Set Up

Spectrophotometers consist of a number of fundamental components: Light Sources (UV and VIS), monochromator (wavelength selector), sample holder, a detector, signal processor and readout. The radiation source used is often a tungsten filament, a deuterium arc lamp which is continuous over the ultraviolet region, and more recently light emitting diodes (LED) and xenon arc lamps for the visible wavelengths. The detector is typically a photodiode or a CCD. Photodiodes are used with monochromators, which filter the light so that only light of a single wavelength reaches the detector. When measuring absorbance at the UV spectrum, the other

lamp has to be turned off. The same goes when measuring visible light absorbance. **Fig.4.5** shows schematic diagram of UV–Vis–NIR Spectrophotometer.

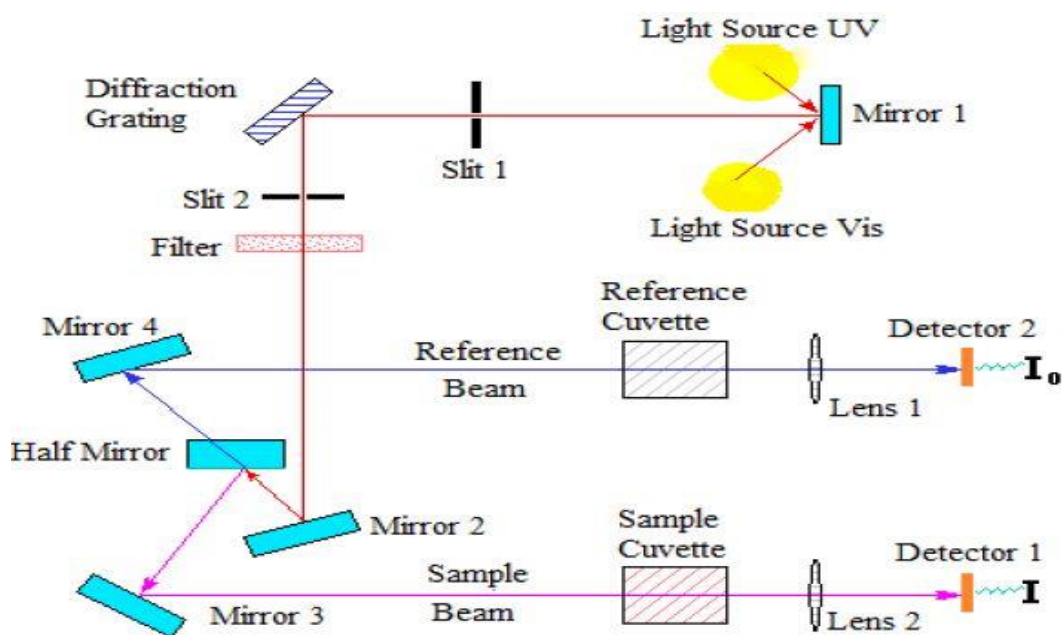


**Fig.4.5** Schematic diagram of UV–Vis–NIR Spectrophotometer.

The light source is a monochromator; the light is split into two equal intensity beams by a half mirrored device before it reaches the sample. One beam, the sample beam, passes through a small transparent container (cuvette) containing a solution of the compound being studied in a transparent solvent. The other beam, the reference, passes through an identical cuvette containing only the solvent. The containers for the sample and reference solution must be transparent to the radiation which will pass through them. Quartz or fused silica cuvettes are required for spectroscopy in the UV–Vis–NIR region. The light sensitive detector follows the sample chamber and measures the intensity of light transmitted from the cuvettes and passes the information to a meter that records and displays the value to the operator on an LCD screen. The intensities of these light beams are then measured by electronic detectors and compared. Some UV–Vis spectrophotometry has two detectors the phototube and the photomultiplier tube. The sample and reference beam are measured at the same time. The intensity of the reference beam, which should have suffered little or no light absorption, is defined as  $I_0$ . The intensity of the sample beam is defined as  $I$ . Over a short period of time, the Spectrometer automatically scans all the component wavelengths in the manner described. The ultraviolet (UV) region scanned is normally from 200 to 400 nm, and the visible portion is from 400 to 800 nm. Therefore, this method is excellent to both determine the concentration and identify the molecular structure or the structural changes. Spectrophotometer is also useful to study the

changes in the vibration and conformation energy levels after and before an interaction with a substrate, or another molecule. **fig.4.6** shows experimental set-up of UV-Vis-NIR Spectrophotometer.



**Fig.4.6** Experimental set up of UV-Vis-NIR Spectrophotometer.

## 4.4 Spectrofluorometer – PL (Photoluminescence)

### 4.4.1 Basic Principle

Photoluminescence spectroscopy is a contactless, versatile, non-destructive, powerful optical method of probing the electronic structure of materials. Light is directed onto a sample, where it is absorbed and imparts excess energy into the material in a process called photo-excitation. One way this excess energy can be dissipated by the sample is through the emission of light, or luminescence. In the case of photo-excitation, this luminescence is called photoluminescence. Thus photoluminescence is the spontaneous emission of light from a material under optical excitation. This light can be collected and analysed spectrally, spatially and also temporally. The intensity and spectral content of this photoluminescence is a direct measure of various important material properties.

Photo excitation causes electrons within the material to move into permissible excited states. When these electrons return to their equilibrium states, the excess energy is released and may

include the emission of light (a radiative process) or May not (a non-radiative process) as shown in **fig.4.7**. The energy of the emitted light (photoluminescence) relates to the difference in energy levels between the two electron states involved in the transition between the excited state and the equilibrium state. The quantity of the emitted light is related to the relative contribution of the radiative process. PL spectroscopy gives information only on the low lying energy levels of the investigated system. In semiconductor systems, the most common radiative transition is between states in the conduction and valence bands, with the energy difference being known as the bandgap. During a PL spectroscopy experiment, excitation is provided by laser light with an energy much larger than the optical band gap. The photo excited carriers consist of electrons and holes, which relax toward their respective band edges and recombine by emitting light at the energy of the band gap. Radiative transitions in semiconductors may also involve localized defects or impurity levels therefore the analysis of the PL spectrum leads to the identification of specific defects or impurities, and the magnitude of the PL signal allows determining their concentration. The respective rates of radiative and nonradiative recombination can be estimated from a careful analysis of the temperature variation of the PL intensity and PL decay time. At higher temperatures nonradiative recombination channels are activated and the PL intensity decreases exponentially. Thus photoluminescence is a process of photon excitation followed by photon emission and important for determining band gap, purity, crystalline quality and impurity defect levels of semiconducting material. It also helps to understand the underlying physics of the recombination mechanism. PL spectrum is quite different from absorption spectrum in the sense that absorption spectrum measures transitions from the ground state to excited state, while photoluminescence deals with transitions from the excited state to the ground state. The period between absorption and emission is typically extremely short. An excitation spectrum is a graph of emission intensity versus excitation wavelength which looks very much like an absorption spectrum. The value of wavelength at which the molecules absorbs energy can be used as the excitation wavelength which provide a more intense emission at a red shifted wavelength, with a value usually twice of the excitation wavelength.

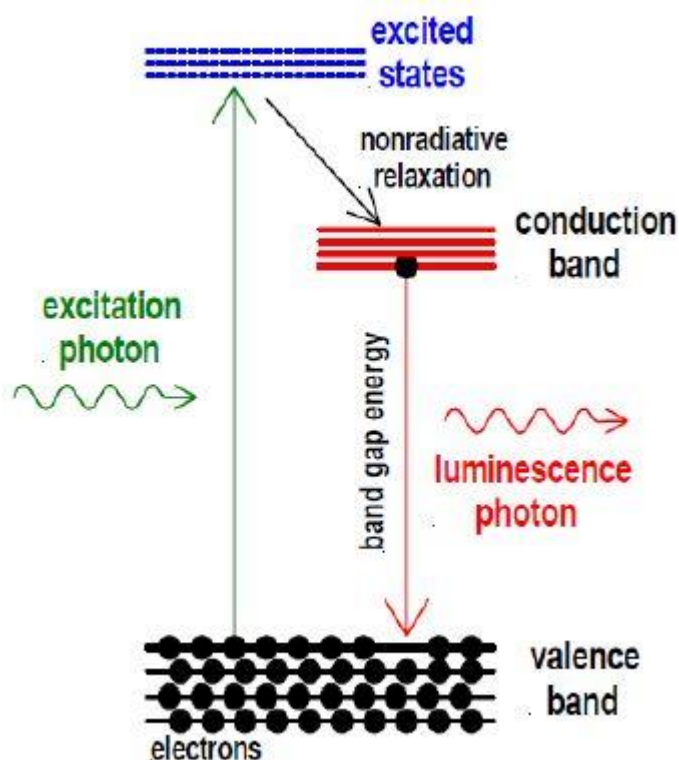


**Fig.4.7** Principle of photoluminescence spectroscopy (PL).

## 4.4.2 Experimental Set Up

A Spectrofluorometer is an analytical instrument used to measure and record the fluorescence of a sample. While recording the fluorescence, the excitation, emission or both wavelength may be scanned. With additional accessories, variation of signal with time, temperature, concentration, polarization, or other variables may be monitored. **Fig.4.8** shows the block diagram of fluorescence spectrometer. Fluorescence spectrometers use laser sources, which contains wavelength selectors, sample illumination, detectors and corrected spectra.

**Illuminator source:** - The continuous light source is 150 W ozone free xenon arc lamp. Light from the lamp is collected by a diamond turned elliptical mirror, and then focused on the entrance slit of the excitation monochromator. The lamp housing is separated from the excitation monochromator by a quartz window. This vents heat out of the instrument, and protects against the unlikely occurrence of lamp failure. Resolution over the entire spectral range and minimize spherical aberrations and re diffraction.



**Monochromators:** - It contains two monochromators:

Excitation monochromator and Emission monochromator.

They use all reflective optics to maintain high resolution over the entire spectral range, and minimize spherical aberrations and re diffraction.

**Gratings:** - The essential part of a monochromator is a reflection grating. A grating disperses the incident light by means of its vertical grooves. A spectrum is obtained by rotating the gratings contain 1200 grooves  $\text{mm}^{-1}$ , and are blazed at 330 nm (excitation) at 500 nm (emission). Each grating is coated with  $\text{MgF}_2$  for protection against oxidation.

**Slits:** - The entrance and exit ports of each monochromator have continuously adjustable slits. The width of the slits on the excitation monochromator determines the band pass of light incident on the sample. The emission monochromators slits control the intensity of the fluorescence signal recorder by the signal detector. When setting slit width, the trade-off is intensity of signal versus spectral resolution. The wider the slits are, the more light falls on the sample and detector, but the resolution decreases. The narrower slits are, the higher the resolution gets but at the expense of signal.

**Shutters:** - An excitation shutter is located just after the excitation monochromator's exit slit. The shutter protects sample from photo bleaching or photo degradation from prolonged exposure to the light source. An emission shutter is placed just before the emission monochromator's entrance and protects the detector from bright light.

**Sample compartment:** - The sample compartment accommodates various optional accessories, as well as fiber optic bundles to take the excitation beam to a remote sample and return the emission beam to the emission monochromator.

**Detectors:** - It contains two detectors: Signal detector and reference detector. The signal detector is a photon counting detector. This detector is an R928P photomultiplier tube, which sends the signal to a photon counting module. The reference detector monitors the xenon lamp, in order to correct for wavelength and time dependent output of the lamp. This detector is a UV enhance silicon photodiode, which is just before the sample compartment.

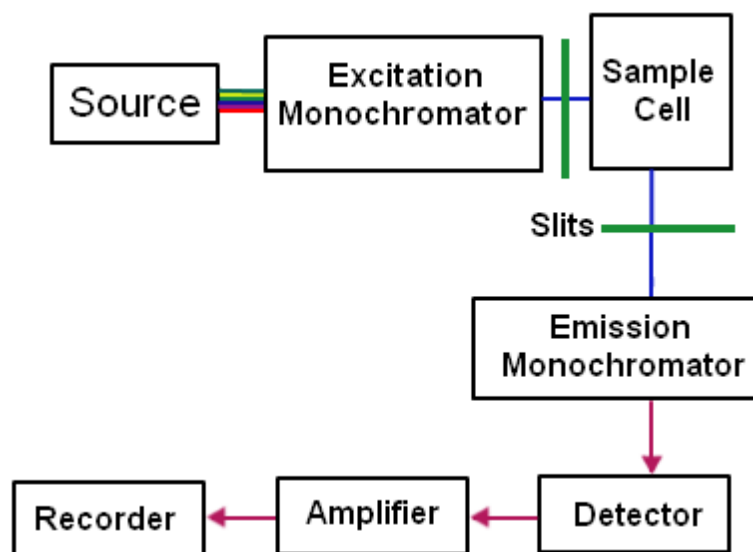


Fig.4.8 Block diagram of fluorescence spectrometer

## 4.5 Fourier Transform Infrared Spectroscopy (FTIR)

### 4.5.1 Basic Principle

Infrared spectroscopy is an important technique in organic chemistry. It is an easy way to identify the presence of certain functional groups in a molecule. Also, one can use the unique collection of absorption bands to confirm the identity of a pure compound or to detect the presence of specific impurities. Analysis by infrared spectroscopy is based on the fact that molecules have specific frequencies of internal vibrations. These frequencies occur in the infrared region of the electromagnetic spectrum:  $\sim 4000\text{ cm}^{-1}$  to  $\sim 200\text{ cm}^{-1}$ .

When a sample is placed in a beam of infrared radiation, the sample will absorb radiation at frequencies corresponding to molecular vibrational frequencies, but will transmit all other frequencies. The frequencies of radiation absorbed are measured by an infrared spectrometer, and the resulting plot of absorbed energy vs. frequency is called infrared spectrum of the material. Identification of a substance is possible because different materials have different vibrations and yield different infrared spectra. Furthermore, from the frequencies of the absorption it is possible to determine whether various chemical groups are present or absent in

a chemical structure. In addition to the characteristic nature of the absorption, the magnitude of the absorption due to a given species is related to the concentration of that species.

Fourier Transform Infrared (FTIR) spectrometry was developed in order to overcome the limitations encountered with dispersive instruments. The main difficulty was the slow scanning process. A method for measuring all of the infrared frequencies simultaneously, rather than individually, was needed. A solution was developed which employed a very simple optical device called an interferometer. The interferometer produces a unique type of signal which has all of the infrared frequencies “encoded” into it. The signal can be measured very quickly, usually on the order of one second or so. Thus, the time element per sample is reduced to a matter of a few seconds rather than several minutes. Most interferometers employ a beam splitter which takes the incoming infrared beam and divides it into two optical beams. One beam reflects off of a flat mirror which is fixed in place. The other beam reflects off of a flat mirror which is on a mechanism which allows this mirror to move a very short distance (typically a few millimetres) away from the beam splitter. The two beams reflect off of their respective mirrors and are recombined when they meet back at the beam splitter. Because the path that one beam travels is a fixed length and the other is constantly changing as its mirror moves, the signal which exits the interferometer is the result of these two beams “interfering” with each other. The resulting signal is called an interferogram which has the unique property that every data point (a function of the moving mirror position) which makes up the signal has information about every infrared frequency which comes from the source. This means that as the interferogram is measured; all frequencies are being measured simultaneously. Thus, the use of the interferometer results in extremely fast measurements.

## **4.5.2 Experimental Set Up**

Fourier Transform Infrared Spectroscopy is a technique which is used to analyse the chemical compositions of many organic compounds, polymers, paints, coatings, adhesive, lubricants semiconductor material, coolants, gases, biological samples and minerals.

Basic components of FTIR.

**1. The Source:-** Infrared energy is emitted from a glowing black body source. This beam passes through an aperture which controls the amount of energy presented to the sample (and, ultimately, to the detector).

**2. The Interferometer:-** The beam enters the interferometer where the “spectral encoding” takes place. The resulting interferogram signal then exits the interferometer.

**3. The Sample:-** The beam enters the sample compartment where it is transmitted through or reflected off of the surface of the sample, depending on the type of analysis being accomplished. This is where specific frequencies of energy, which are uniquely characteristic of the sample, are absorbed.

**4. The Detector:-** The beam finally passes to the detector for final measurement. The detectors used are specially designed to measure the special interferogram signal.

**5. The Computer:-** The measured signal is digitized and sent to the computer where the Fourier transformation takes place. The final infrared spectrum is then presented to the user for interpretation and any further manipulation.



**Fig.4.9** Experimental set up of FTIR spectrometer.

## 4.6 Raman Spectroscopy

### 4.6.1 Basic Principle

Raman spectroscopy is a useful technique for the identification of a wide range of substances—solids, liquids and gases. It is a straightforward, non-destructive technique requiring no sample preparation. Raman spectroscopy involves illuminating a sample with monochromatic light and using a spectrometer to examine light scattered by the sample.

Raman spectroscopy is a spectroscopic technique based on inelastic scattering of monochromatic light, usually from a laser source. Inelastic scattering means that the frequency of photons in monochromatic light changes upon interaction with a sample. Photons of the laser light are absorbed by the sample and then reemitted. Frequency of the reemitted photons is shifted up or down in comparison with original monochromatic frequency, which is called the Raman effect. This shift provides information about vibrational, rotational and other low frequency transitions in molecules. This effect is based on molecular deformations in electric field  $E$  determined by molecular polarizability ( $\alpha$ ). The laser beam can be considered as an oscillating electromagnetic wave with electrical vector  $E$ . Upon interaction with the sample it induces electric dipole moment

$$\vec{P} = \vec{\alpha}\vec{E}$$

which deforms molecules. Because of periodical deformation, molecules start vibrating with characteristic frequency  $\nu_m$ . Monochromatic laser light with frequency  $\nu_o$  excites molecules and transforms them into oscillating dipoles. Such oscillating dipoles emit light of three different frequencies as shown in **fig.4.10** when:

1. A molecule with no Raman active modes absorbs a photon with the frequency  $\nu_m$ . The excited molecule returns back to the same basic vibrational state and emits light with the same frequency  $\nu_o$  as an excitation source. This type of interaction is called an elastic Rayleigh scattering.
2. A photon with frequency is absorbed by Raman active molecule which at the time of interaction is in the basic vibrational state. Part of the photon's energy is transferred to the

Raman active mode with frequency  $\nu_m$  and the resulting frequency of scattered light is reduced to  $\nu_o - \nu_m$ . This Raman frequency is called Stokes frequency or just “Stokes”.

3. A photon with frequency  $\nu_o$  is absorbed by a Raman active molecule, which, at the time of interaction, is already in the excited vibrational state. Excessive energy of excited Raman active mode is released, molecule returns to the basic vibrational state and the resulting frequency of scattered light goes up to  $\nu_o + \nu_m$ . This Raman frequency is called Anti Stokes frequency or just “Anti Stokes”.

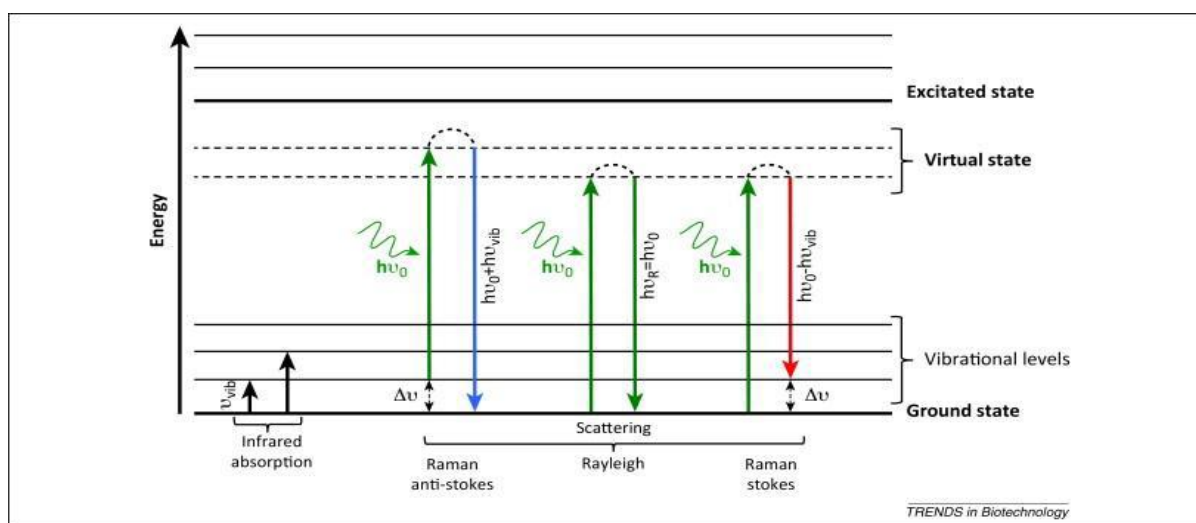


**Fig.4.10** Shows vibrational levels of the material

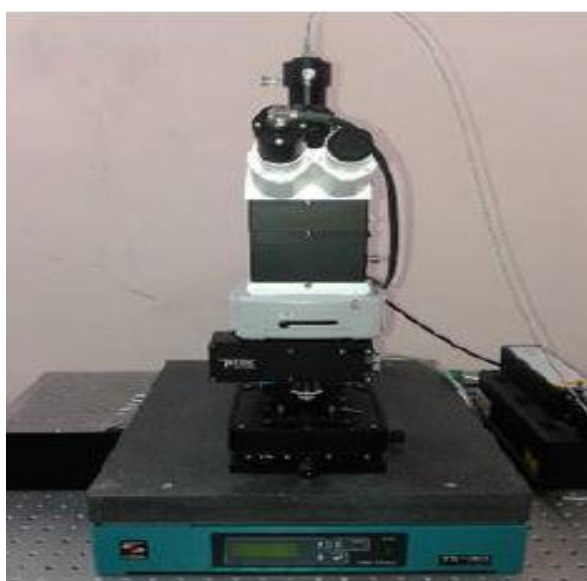


**Fig. 4.11** Experimental set up of Raman spectrometer.

## 4.6.2 Experimental Set Up

A Raman system typically consists of four major components:

1. Excitation source (Laser).
2. Sample illumination system and light collection optics.
3. Wavelength selector (Filter or Spectrometer).
4. Detector (Photodiode array, CCD or PMT).

In Raman instrument a sample is illuminated with a laser beam. Light from the illuminated spot is collected with a lens and sent through interference filter or spectrometer to obtain Raman spectrum of a sample. Wavelengths close to the laser line, due to elastic Rayleigh scattering, are filtered out while the rest of the collected light is dispersed onto a detector. By changing the laser light you can confirm if a peak is a true Raman peak and not a peak just associated with the wavelength of the laser light that was used. Spontaneous Raman scattering signal is very weak because most of the incident photons undergo elastic Rayleigh scattering. Therefore special measures should be taken to distinguish it from the predominant Rayleigh scattering. Instruments such as notch filters, tunable filters, laser stop apertures, double and triple spectrometric systems are used to reduce Rayleigh scattering and obtain high quality Raman spectra.

In some instruments, sample is placed into the cryostat chamber where the low temperature is achieved by the use of liquid helium that cooled the cryostat. The cryostat is kept in vacuum so that laser light suffer no scattering from the particles of the air in the chamber. Before every measurement the scattered light would have to be aligned in the spectrometer so that maximum signal would hit the detector. This can be achieved by moving the sample to different positions and using lens, mirror system. In earlier times for taking Raman spectrum single point detectors such as photon counting Photomultiplier Tubes (PMT) was used.

However, due to the consumption of very long time PMT is not preferred because it slow down any research or industrial activity based on Raman analytical technique. Nowadays, Raman spectroscopy has become even more accurate and easier due to advancements in optics, laser and computer technology. Researchers use multi-channel detectors like Photo Diode Arrays (PDA) or, more commonly, a Charge Coupled Devices (CCD) to detect the Raman scattered light. Charge Coupled Device (CCD) detectors have enormously helped the use of Raman

spectroscopy by allowing scientist to take data quicker and with more precision that they were able to with the older photomultiplier tubes. The CCD has an array of detectors that can look at a range of wavelengths at one time greatly reducing the collection time. Sensitivity and performance of modern CCD detectors are rapidly improving.

Raman spectroscopy can be used on liquids, solids and gases making it very versatile for studying various materials.

## 4.7 Field emission scanning electron microscope (FESEM):

### 4.7.1 Basic Principle

In standard electron microscopes, electrons are mostly generated by heating a tungsten filament (electron gun). They are also produced from a crystal of LaB6. The use of LaB6 results in a higher electron density in the beam and a better resolution than that with the conventional used device. In a field emission (FE) electron microscope, no heating but a so-called "cold" source is used. Field emission microscope is a type of electron microscope that is usually employed to investigate the surface of a sample by scanning it with a high energy beam of electrons. Here, the wave properties of electrons ( $\lambda = h/p$ ,  $\lambda$  associated with a beam of electrons of momentum  $p$ ) are used to obtain resolution. If the electrons are accelerated through a potential difference  $V$ , they acquire energy,

$$eV = \frac{p^2}{2m} \Rightarrow \lambda = \frac{h}{p} = \frac{h}{\sqrt{2meV}}$$

So  $V = 100\text{kV}$  leads to  $\lambda = 3.9 \times 10^{-12} \text{ m}$ , which is about a hundredth of the separation of the atoms in molecules ( $\sim 0.25 \text{ nm}$ ) or crystals.

In FESEM, the electron beam passes through objective lens deflect horizontally and vertically so that the beam scans the surface of the sample. As the electrons penetrate the surface of the sample, a number of interactions occur that can result in the emission of electrons or photons from or through the surface. The generated secondary electrons are collected by the detector and converted into voltage. The amplified voltage is applied to the grid of the CRT which changes the intensity of the spot light. In this way an image is produced on the CRT; every point that the beam strikes on the sample is mapped directly onto a corresponding point on the screen. When an electron beam interacts with the atoms of a Nano structures sample, each

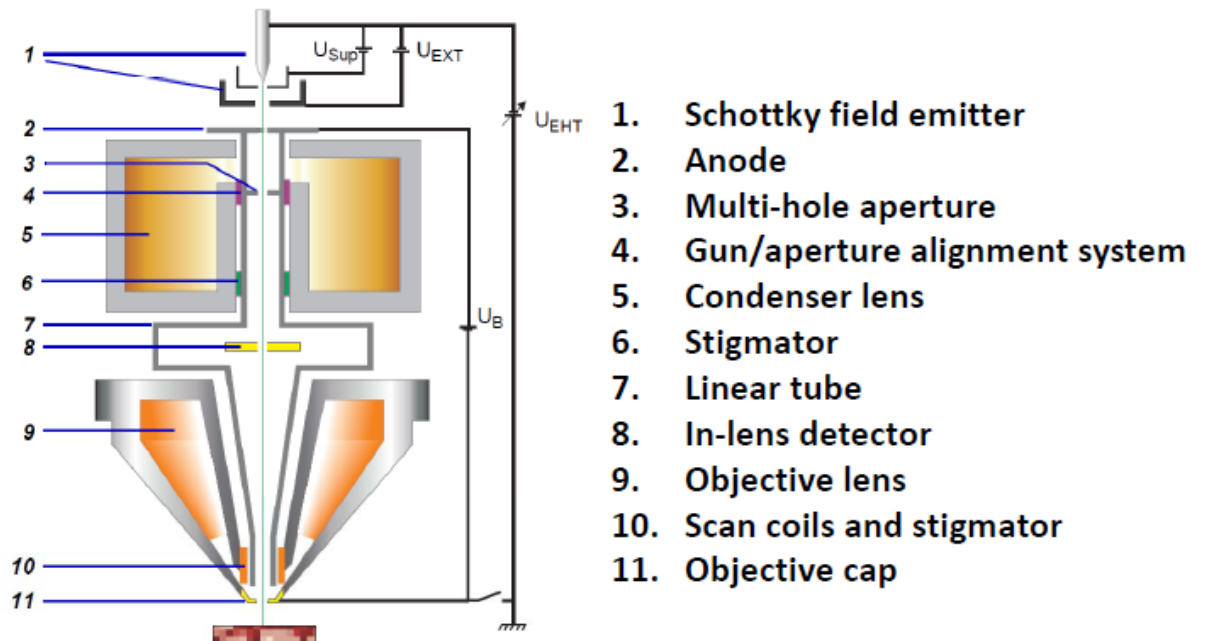


incident electron undergoes two types of scattering elastic and inelastic. In elastic scattering, only the trajectory changes and the kinetic energy and velocity remain constant. In the case of inelastic scattering, the incident electrons displace electrons from the sample orbits around nuclei of atoms. The electron interacts with the sample produces signal about the sample's morphology, composition and other properties. The morphologies of the synthesized nanomaterials are characterized with the help of field emission scanning electron microscopy (FESEM, S-4800).



**Figure 4.12:** Hitachi S4800 FESEM with EDX attachment

## 4.7.2 Experimental Set Up



- ❖ Schottky emitter (1) emits electrons. The beam of electrons passes through anode (2) aperture.
- ❖ Electron beam passes through the multihole aperture (3). Standard aperture is 30  $\mu\text{m}$  hole. Other aperture sizes can be selected by using the gun/aperture alignment system (4).
- ❖ Stigmator (6) makes sure the beam is rotationally symmetrical.
- ❖ Anode and linear tube (7) are connected to form the beam booster
- ❖ Beam booster provides better protection against external stray fields.
- ❖ Condenser lens (5) controls the amount of demagnification. Objective lens focuses the electron beam onto the booster. Specimen. Objective lens consists of electromagnetic (8) and electrostatic (9) lens.
- ❖ Deflection system consists of a set of scan coils (10) to move the electron beam in a point-to-point scan process.

# **CHAPTER-5**

**Novel synthesis and size-dependent  
properties of Fe<sub>3</sub>O<sub>4</sub> nanoparticles**

## 5.1 Introduction

Extensive literature survey reveals a wide variety of bottom-up magnetite synthesis methods including co-precipitation, sol-gel technique, one-pot synthesis with reflux or hot-injection method in inert condition, electrochemical, solvothermal or hydrothermal, reduction followed by microwave irradiation, thermal decomposition of iron (III) acetylacetonate in polyol medium etc. Use of different bases, reducing and capping agents such as NaOH, KOH, NaBH<sub>4</sub>, N(CH<sub>3</sub>)<sub>4</sub>OH, sodium oleate, PEG, PVA, PVP etc have been reported previously. The effect of size, shape, morphology and surface functionalization in different physio-chemical properties have been thoroughly scrutinized by many researchers.

Polyol-mediated synthesis is a versatile chemical approach to prepare high-quality water-stable Fe<sub>3</sub>O<sub>4</sub> NP's. In this method; an even mixture of ethylene glycol (EG), diethylene glycol (DEG), triethylene glycol (TREG), tetraethylene glycol (TEG) and polyethylene glycol (PEG) of different molecular weights often act as a high-boiling point solvent cum reductant, as well as a stabilizer to control the particle growth and morphology and thereby prevents interparticle aggregation. Compared to the thermal decomposition method, Fe<sub>3</sub>O<sub>4</sub> NP's prepared by this route exhibit better stability and dispersibility in organic solvents due to polyol coating. However, such a coating is not covalently linked to the particle-surface and therefore achieves a relatively weak interaction with polyol-molecules. When these NP's are introduced inside a body, they usually exhibit poor stability due to the desorption of polyols, facilitating their aggregation and uptake by the macrophages. Considering these factors, long-term colloidal stability under physiological conditions is desired to overcome these problems. Biocompatible carboxylic acid salts with coating tendency can conquer this problem. Shen *et al.* have synthesized ultra-small, monodispersed and water-dispersible Fe<sub>3</sub>O<sub>4</sub> NP's by using trisodium citrate as growth inhibitor cum stabilizer, whereas Wang *et al.* have produced smaller NP's via high-temperature coprecipitation approach using poly(acrylic acid) as a capping agent to control morphology. Jun *et al.* developed biocompatible Fe<sub>3</sub>O<sub>4</sub> nanocrystalline samples by using 2,3-dimercaptosuccinic acid (DMSA) as a capping ligand to study size-dependent magnetic properties for MFH & MRI-based applications.

## 5.2 Microwave Synthesis Reactor and its implication

Fe<sub>3</sub>O<sub>4</sub> NP's were synthesized in the single-mode Anton-Paar microwave reactor - Monowave 200. The system operates at a frequency of 2.45 GHz with a maximum power of 850 W. Pressure and temperature could be simultaneously monitored by an external infrared (IR) sensor and an internal fibre-optic (FO) probe. With this system, glass-vials of 2 different size (G10 & G30; the number represents the maximum capacity of the vial in ml) and one Silicon Carbide (SiC) vial (C10) were supplied. Only SiC vials are suitable for this synthesis protocol in order to prevent accidents during reactions at the maximum values of temperature ( $T_{\max} = 260^{\circ}\text{C}$ ) and pressure ( $P_{\max} = 30$  bar).

In traditional solvothermal routes, the precursor-solution is directly transferred to a teflon-lined stainless still jacket and placed to be heated in an oven for hours or even days. However homogeneous and well-dispersed the precursors are, eventually undergoes some density distribution inside; besides due to finite thermal conductivity of the container as well as the precursor-medium, the part of the solution in direct touch with the teflon-wall attains the required temperature first and then it slowly gets conducted to the interior region. Naturally, seed-crystals get created first at the exterior region, and by the time the interior-part reaches the set-temperature, the outer seeds already grow to a certain extent. Moreover, the growth-dynamics hugely depend on the local density of the precursors. Hence, particles of a broad size-distribution are formed, which is hardly suitable for size-dependent studies like the following. The best way to acquire uniform nucleation & growth is continuous stirring to cease any density or temperature-gradient; which is followed in one-pot or reflux methods. In microwave synthesis reactor the magnetic beed can be rotated upto 1200 rpm, higher than that of the traditional one-pot set-ups; generating very narrow size-distribution of the NP's in a very short span of time.

## 5.3 Reagents and materials

All reagents were of analytical grade (Assay  $\geq 99\%$ ) and used directly without any further purification. Ethylene glycol (EG), diethylene glycol (DEG) and polyethelene glycol (PEG; Avg. mol. wt.  $\sim 6000$ ) were used to prepare the polyol solvent. Ferric Chloride hexahydrate (FeCl<sub>3</sub> · 6H<sub>2</sub>O) and anhydrous sodium acetate (CH<sub>3</sub>COONa) with  $\geq 99.5\%$  purity are the principle precursors, purchased from SIGMA-ALDRICH. Hydrated disodium (+) tartrate

[(CHOH . COONa)<sub>2</sub> . 2H<sub>2</sub>O] was bought from LOBA Chemie. Absolute ethanol from Merck and deionised water (~18.2 MΩ) were used for washing.

## 5.4 Synthesis Procedure

### 5.4.1 Microwave-assisted synthesis

In a typical synthesis of 4 nm Fe<sub>3</sub>O<sub>4</sub> NP's 0.35 gm (1.29 mmol) FeCl<sub>3</sub> . 6H<sub>2</sub>O was first mixed vigorously in a solution of 20 ml DEG and 5 ml EG to form a clear solution. Then, 0.15 gm (0.65 mmol) disodium tartrate was added followed by 1.2 gm (14.63 mmol) CH<sub>3</sub>COONa and 1.5 gm (0.25 mmol) PEG-6000. Then, the mixture was ultra-sonicated for 10 minutes and heated at 80°C along with continuous magnetic stirring for half an hour to form a homogeneous dark yellow solution.

Thereafter, 5 ml of this mixture was transferred into a C10 vial and closed in air; which was then placed inside the microwave synthesis reactor at 220°C and at a pressure of 7-9 bar for 30 minutes with an additional ramp-up time of 5 minutes. To proceed the reaction-dynamics uniformly a tiny magnetic bead was inserted to stir up the solution @1000 rpm during the reaction. After cooling against a compressor, the dark black solution was collected and washed at least 10 times via centrifugation @8,000 rpm at 10°C for 10 minutes each time being dispersed in a mixture of absolute ethanol and deionized water (DI) in 80:20 ratio. It is essential to centrifuge the solution in such a mixture of polar and non-polar liquids, as sodium tartrate does not dissolve in ethanol or other non-polar / very little polar solvents and hence incapable of removing the excess sodium tartrate present in the system. On the other hand, since the as-synthesized Fe<sub>3</sub>O<sub>4</sub> NP's are highly water-dispersible and form a very stable solution with water-like polar solvents; an aqueous solution does not allow the Fe<sub>3</sub>O<sub>4</sub> particles to be centrifuged out of the dispersing medium even @15,000 rpm at only 1°C for half an hour. Finally, the obtained precipitate was dried at 60°C for 5 hours under rough vacuum to obtain fine Fe<sub>3</sub>O<sub>4</sub> powder-sample. Drying in open air might compromise the sample-quality due to partial oxidation to specific phases of Fe<sub>2</sub>O<sub>3</sub>. The details of composition and synthesis-parameters are listed in Table-IA, where in each series (A & B) a continuous decreasing size-profile of Fe<sub>3</sub>O<sub>4</sub> NP's can be seen using Williamson-Hall analysis. Strain (ε) calculated from W-H plot is a bit random for most of the samples.

**Table – IA (Microwave-assisted synthesis)**

Reaction-temperature (°C)	Sample Code	Amount of reagents						Growth-time (minute)	Maximum particle-diameter ( $d_{WH}$ ) in nm from W-H plot
		EG (ml)	DEG (ml)	FeCl <sub>3</sub> . 6H <sub>2</sub> O (gm)	Sodium tartrate (gm)	Sodium acetate (gm)	PEG -6000 (gm)		
220 (Series – A)	A1	25	X	0.50	0.02	1.75	1.00	90	50.3 ± 3.9
	A2	25	X	0.40	0.03	1.50	1.20	60	39.9 ± 5.1
	A3	20	5	0.40	0.04	1.50	1.20	45	34.4 ± 2.6
	A4	15	10	0.40	0.06	1.40	1.30	45	15.7 ± 4.8
	A5	10	15	0.40	0.10	1.30	1.40	30	10.6 ± 4.7
	A6	5	20	0.35	0.15	1.20	1.50	30	5.9 ± 2.9
200 (Series – B)	B1	25	X	0.50	0.02	1.75	1.00	90	45.0 ± 1.0
	B2	25	X	0.40	0.03	1.50	1.20	60	32.2 ± 1.9
	B3	20	5	0.40	0.04	1.50	1.20	45	18.0 ± 3.0
	B4	15	10	0.40	0.06	1.40	1.30	45	9.9 ± 2.9
	B5	10	15	0.40	0.10	1.30	1.40	30	8.1 ± 3.0
	B6	5	20	0.40	0.12	1.25	1.45	30	4.5 ± 2.3

The as-synthesized NP's have a strong microwave dissipation at the used frequency of 2.45 GHz, which is responsible for the conversion of microwave irradiation to heat, that finally leads to the ultrafast formation of the NP's. Since the thermal conductivity of the SiC vial is significantly higher than that of the glass/pyrex vials, substances within the vial would be partially shielded from the electromagnetic field and some heat-transfer would also occur through the SiC walls by conduction. This dual heating mechanism causes the ultrafast uniform generation of Fe<sub>3</sub>O<sub>4</sub> nano-seedcrystals within a few minutes. Next, the growth-time is adjusted at a certain temperature and pressure accordingly to control the size of the particles. It is cautionary that, the heating profiles with the maximum power of 850 W are prohibited for SiC vials having a thermal conductivity large enough to exceed the maximum temperature limit inside the microwave reactor.

#### 5.4.2 Solvothermal synthesis

As fast microwave-assisted route is specialized for very small NP synthesis, it is not suitable for synthesizing larger particles ( $\geq 100$  nm) and increasing reaction-time indefinitely

can compromise safety-issues governing microwave synthesis reactor. Hence, we need common solvothermal approach to synthesize larger particles ( $\geq 50\text{nm}$ ), where a large pressure ( $\sim 30\text{bar}$ ) along with temperature play key-role in the reaction-kinetics and particle-size. The as-synthesized particles are expected to have a broader distribution of particle-size, but it is acceptable as such large NP's behave more like bulk-material and hence show less sensitivity towards size.

A suitable mixture of all the precursors as described in section 3.3.1 are ultra sonicated and magnetically stirred at  $80^\circ\text{C}$  for an hour to form a homogeneous solution (Details of composition is given in Table-IB). The resulting mixture was then put into a Teflon-lined stainless steel-autoclave with a capacity of 50 mL and maintained at  $185^\circ\text{C}$  for 10-20 hrs. After natural cooling, the black product was precipitated with ethanol followed by centrifugation and vacuum-drying. Commercial  $\text{Fe}_3\text{O}_4$  powder was also purchased from SIGMA-ALDRICH to compare the properties of as-synthesized NP's.

**Table – IB (Synthesis of semi-nanoparticles via common solvothermal route)**

Sample Code	Amount of reagents						Reaction-time (hours)	Maximum particle-diameter ( $d_{\text{WH}}$ ) in nm from W-H plot
	EG (ml)	DEG (ml)	$\text{FeCl}_3 \cdot 6\text{H}_2\text{O}$ (gm)	Sodium tartrate (gm)	Sodium acetate (gm)	PEG - 6000 (gm)		
C1	35	5	1.0	0.1	3.0	1.0	20	$150.8 \pm 4.9$
C2	30	10	0.9	0.1	2.5	1.5	15	$119.2 \pm 6.9$
C3	25	15	0.8	0.1	2.0	2.0	10	$84.0 \pm 2.9$
S	Bulk powder-sample purchased from SIGMA-ALDRICH							$39.1 \pm 7.0$

## 5.5 Role of surfactants and capping agents in coating mechanism

In the synthesis and storage of multivariant transition metal oxides; stability demands utmost importance. On exposure to ambient atmosphere, the surface of  $\text{Fe}_3\text{O}_4$  crystallites are often covered with a few layers of  $\alpha\text{-Fe}_2\text{O}_3$  (as is true for most oxides), monolayer amounts of surface hydroxyls as well as physisorbed  $\text{H}_2\text{O}$ . Very often organic compounds are employed to passivate the surface of NP's during or after synthesis to avoid agglomeration. The main cause is the hydrophobic surfaces with a large surface area-to-volume ratio, which in absence of a suitable surface-coating, acquires hydrophobic interactions in between causing interparticle aggregation and formation of large clusters. The capping agents limit the size of NP's by preventing further particle growth and agglomeration during synthesis and can also be useful



in controlling the particle reactivity, imparting solubility and packing characteristics. Surfactants are also used to control morphology and protect nanoparticles from deteriorating in environment.

In this reaction, sodium acetate acts as a nucleating agent and helps to partially reduce  $\text{Fe}^{3+}$  ions to  $\text{Fe}^{2+}$  in the polyol medium to form  $\text{Fe}_3\text{O}_4$ . PEG not only functionalizes the surface of NP's and acts as a stabilizer, but also dissipates heat energy from microwave to facilitate the reaction. Biocompatible sodium tartrate was chosen, as it can act as a crystal grain growth inhibitor depending on concentration for the synthesis of ultra-small nanoparticles and QD. In addition, the two carboxylate groups of tartrate salts have strong coordination affinity to  $\text{Fe}^{3+}$  ions. This supports the attachment of tartrate groups on the surface of the  $\text{Fe}_3\text{O}_4$  NP's, controlling growth. Hence, the as-synthesized NP's are also intrinsically stabilized with a layer of the hydrophilic ligands in situ, preventing them from aggregating into larger crystals, which is essential for their long-term stability in aqueous media. Besides, tartrates, found in fruits like grapes, tamarind etc are completely biocompatible and non-toxic and hence ideal for biomedical applications. The joint effect of PEG & tartrate ions to form a core-shell structure in increasing solubility and stability in aqueous medium have been elaborated schematically.

## Results and Discussion

### 5.6 X-ray diffraction (XRD) & Williamson-Hall analysis

The crystallographic phase composition of the as-synthesized samples was determined from X-ray diffraction using Rigaku Miniflex powder X-ray diffractometer; operated at 40kV-15mA. Data was acquired in a  $2\theta$  range:  $20^\circ$ - $80^\circ$  in steps of  $0.02^\circ$  at a rate  $1^\circ/\text{min}$ . All the diffraction peaks are indexed ac. to the inverse-spinel structure known for the  $\text{Fe}_3\text{O}_4$  crystal (JCPDS card no. 85-1436) and no additional peaks were detected, confirming pure phase material. In addition, the average grain-size ( $d_{\text{WH}}$ ) and strain ( $\epsilon$ ) were calculated from the Williamson-Hall equation considering spherical morphology:  $\beta \cos \theta = 4\epsilon \sin \theta + 0.89\lambda/d_{\text{WH}}$ , where  $\beta$  is the full width at half-maximum (FWHM) of a Bragg-peak,  $\theta$  is the diffraction-angle and  $\lambda = 1.5406\text{\AA}$  (for  $\text{Cu } k_\alpha$  line). Depicting  $\beta \cos \theta$  vs  $\sin \theta$  plot,  $d_{\text{WH}}$  and  $\epsilon$  were respectively calculated from the intercept and slope of the straight line. The regular increase in FWHM with decreasing particle-size can be observed clearly in figure-II as a result of increase in tensile stress, point-defects at the surface and an overall disorder in the nanocrystals. The values of  $d_{\text{WH}}$  have been listed in Table-IA and IB for all the samples.

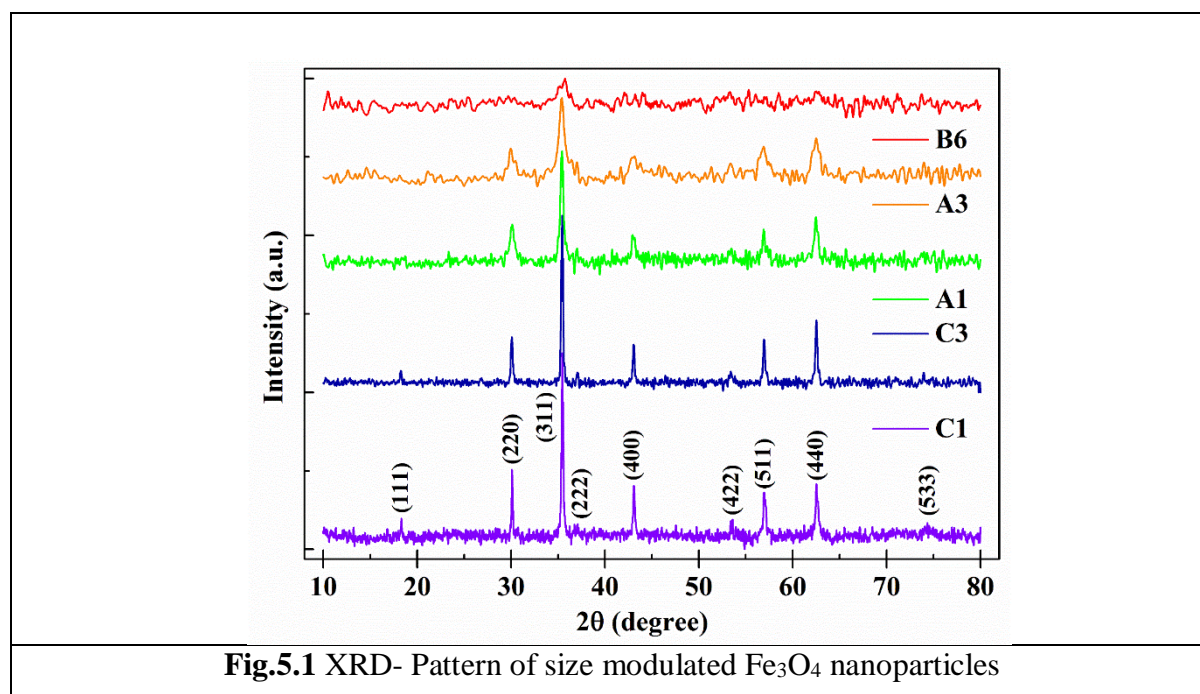
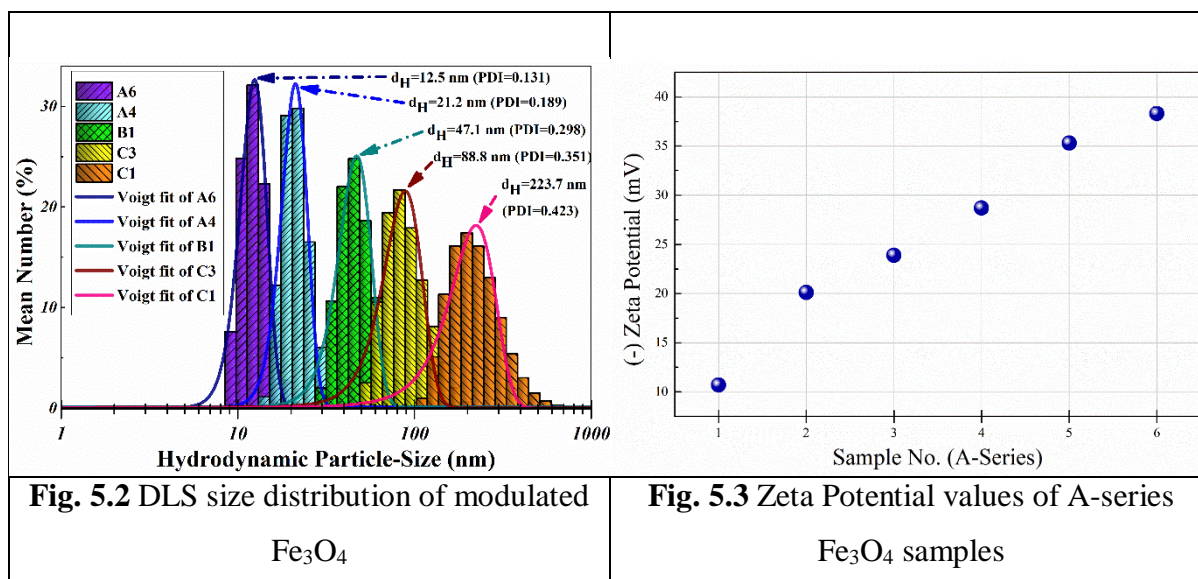


Fig.5.1 XRD- Pattern of size modulated  $\text{Fe}_3\text{O}_4$  nanoparticles

## 5.7 Dynamic light scattering (DLS) & Zeta potential (ZP)

The hydrodynamic particle-size ( $d_H$ ) of the NP's was determined by a DLS instrument (Model DLS-nano ZS90, Zetasizer Nanoseries, Malvern Instruments). A dilute solution ( $\sim 0.1$  mg/ml) was prepared by ultrasonication of the powder-sample in distilled water. The incident laser was projected at an angle of  $173^\circ$  for detecting backscattered photons and the average size was estimated from the autocorrelation function of the time-dependent fluctuation in the scattered intensity. Both  $d_H$  and  $\zeta$ -potential were evaluated from five measurements against each sample.

Particles in a colloidal dispersion scatter an incident laser and the intensity of the scattered light, which continuously fluctuates over time due to Brownian motion of the mobile particles; get detected in DLS. Generally, particles, smaller in size than one-tenth of the wavelength of the incident light (i.e.  $\lambda/10$ ) scatter light elastically and isotropically (Rayleigh scattering). However, when the size of the particles exceeds this threshold of  $\lambda/10$ , then Rayleigh scattering is dominated by anisotropic (preferably in forward and backward direction) Mie scattering. As particle-size further increases, Mie scattering predominantly takes place in the forward direction. Hence, by generating an Autocorrelation function (ACF) based on time-variation of intensity and degree of anisotropy of the scattered light, number-distribution of particle-size is estimated in DLS. By fitting this data with a suitable probability-distribution function such as Voigt (a convolution of Cauchy-Lorentz and Gaussian distribution) most likely particle-size is estimated. Here, the calculated particle-size is not only due to the particle itself; but also because of the hydrated/solvated corona formed at its surface; and hence seems larger always. So, basically in DLS, we get the hydrodynamic size ( $d_H$ ) of the particles, defined by the diameter of a hypothetical hard sphere that diffuses with the same speed as the particles assayed under DLS. In our case, due to the polar core-shell structure of the NP's, the agglomerated  $H_2O$  molecules around; can also cause an increment in  $d_H$  upto 10-15 nm. Polydispersity Index (PDI) is a measure of the distribution of molecular mass in a given sample; also indicates the uniformity of colloidal dispersion. Generally, a dispersion with  $PDI \leq 0.2$  are likely to be monodispersed, as observed for the smaller NP's. In figure-3(a) size-distribution of particles and PDI have been shown for 5 selected samples. The decrease in FWHM & PDI in the smaller variants synthesized by microwave irradiation is quite clear, approaching monodispersity.



Zeta potential (ZP) i.e., the electrokinetic potential at the shear/slipping plane around a colloid-particle moving under an electric field; not only gives information about the surface-charge, but also the stability of the dispersion. It is calculated by determining mobility and using Debye's law:  $\psi = \zeta e^{-\kappa x}$ , where  $\psi$ =surface-potential,  $\zeta$ =ZP,  $\kappa$ =Debye-Hückel parameter; related to the ionic strength and  $x$ =distance from the core-surface (Stern layer). Pure Fe<sub>3</sub>O<sub>4</sub> does not dissolve/disperse in water, ethanol, chloroform, acetone-like solvents, it only dissolves in acidic medium. Naturally, the magnitude of ZP in distilled water is only a few mV's for pure Fe<sub>3</sub>O<sub>4</sub>. But, after surface-functionalization, it has gained ZP upto -38.3mV, indicating formation of water-stable (for days) polar core-shell nanostructures. Figure-3(b) shows the continuous ZP increase of the A-series samples with higher concentration of surfactants and lower size (The raw data has been attached in the supplementary information). The -ve surface-charge has been attributed to the attached tartrate ions and PEG.

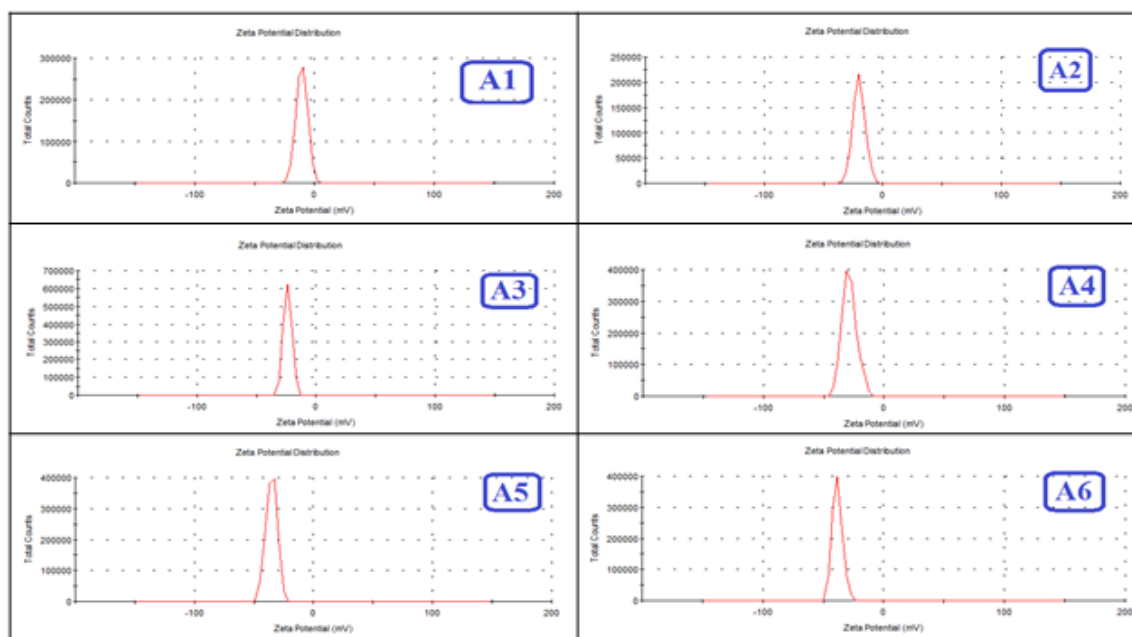
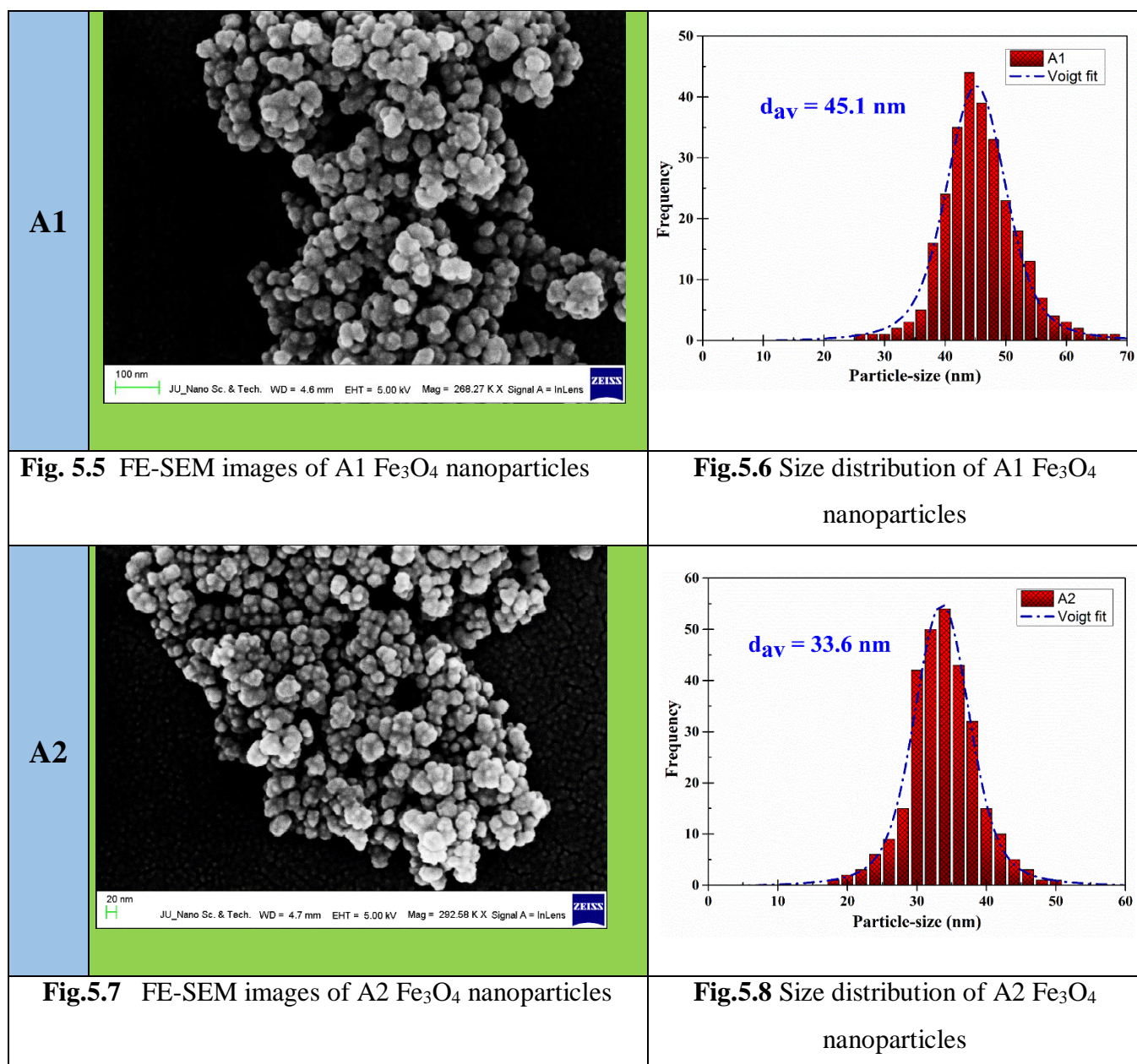


**Fig. 5.4** Zeta Potential distribution of A-series Fe<sub>3</sub>O<sub>4</sub>

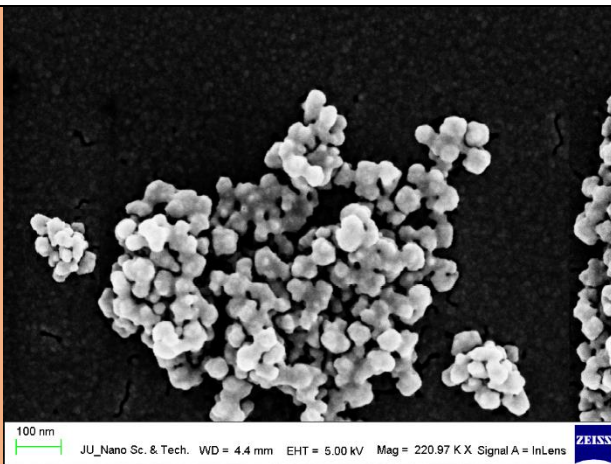
## 5.8 Electron microscopy (FE-SEM and HR-TEM)

Surface morphology and size-distribution of NP's were analyzed using a field emission scanning electron microscope (FESEM, JEOL 6340F FEG-SEM), whereas a high-resolution transmission electron microscope (HRTEM, JEOL-JEM 2100) operated at 200 kV; was employed to observe the NP's, analyse crystalline nature & unidirectional growth. The polycrystalline samples got a spherical morphology because of the polyol medium and tartrate ions. The regular decrease in size and increase in monodispersity can be observed. The HR-TEM images also exhibit well-resolved lattice fringes with interplanar spacings 0.29 & 0.25 nm; corresponding to the (220) and (311) lattice planes respectively, revealing the highly crystalline nature of the NP's.

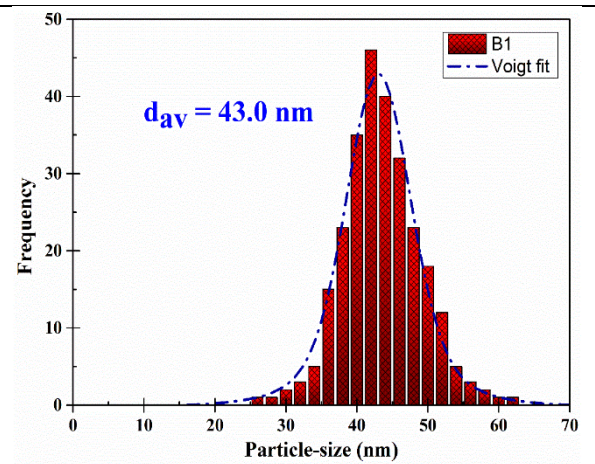
## FE-SEM



B1

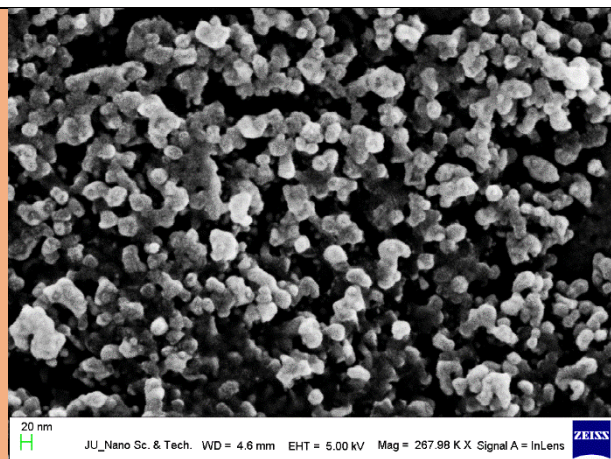


**Fig.5.9** FE-SEM images of B1  $\text{Fe}_3\text{O}_4$  nanoparticles

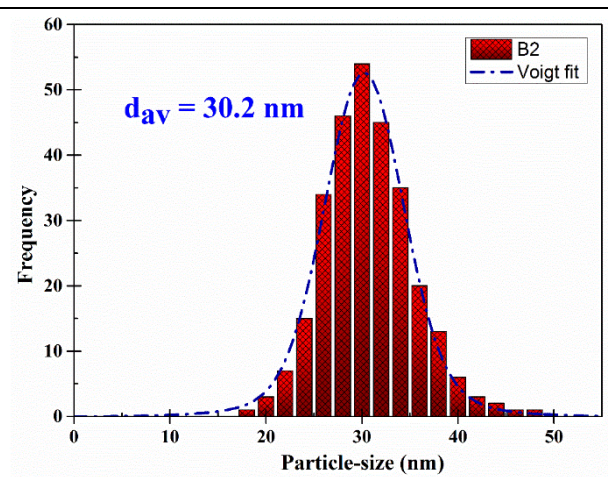


**Fig.5.10** Size distribution of B1  $\text{Fe}_3\text{O}_4$  nanoparticles

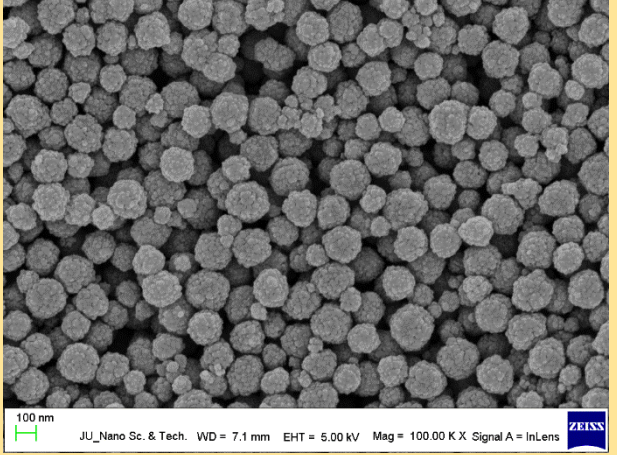
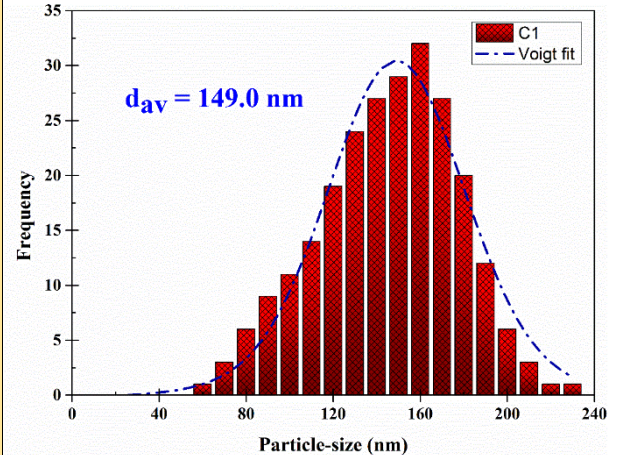
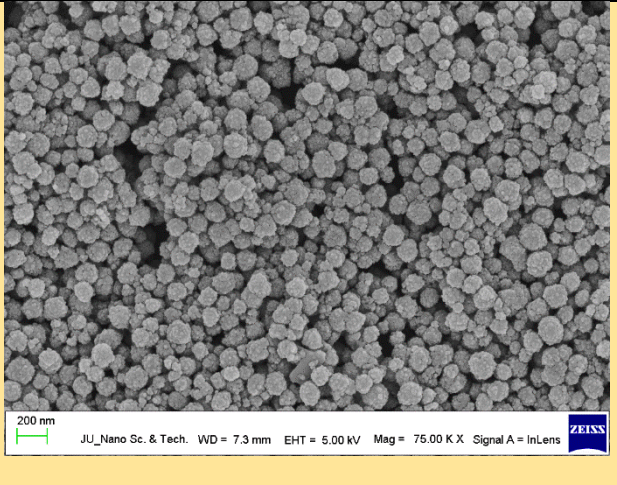
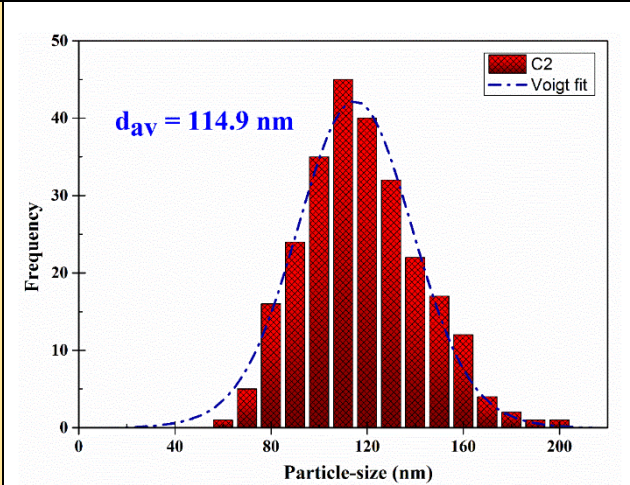
B2



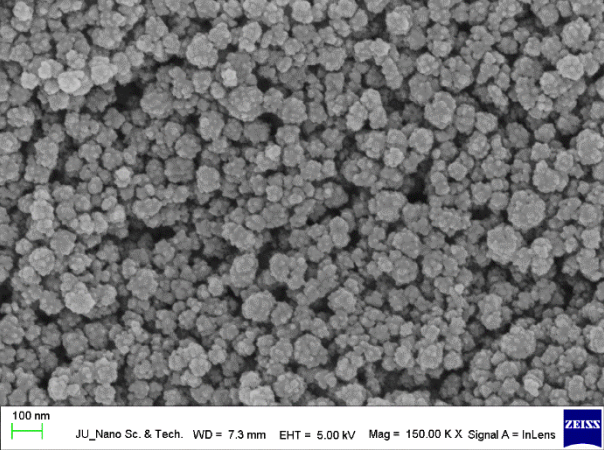
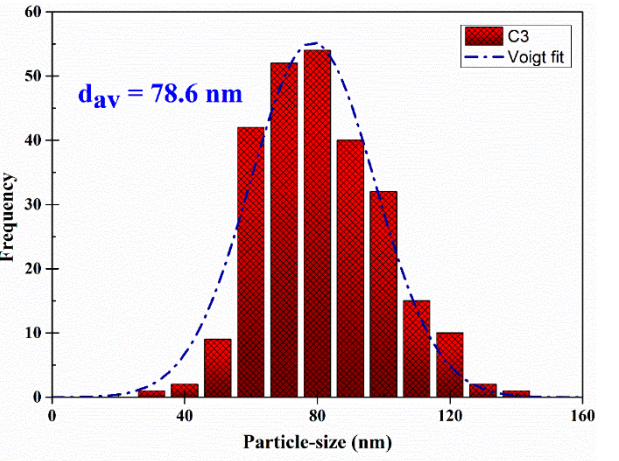
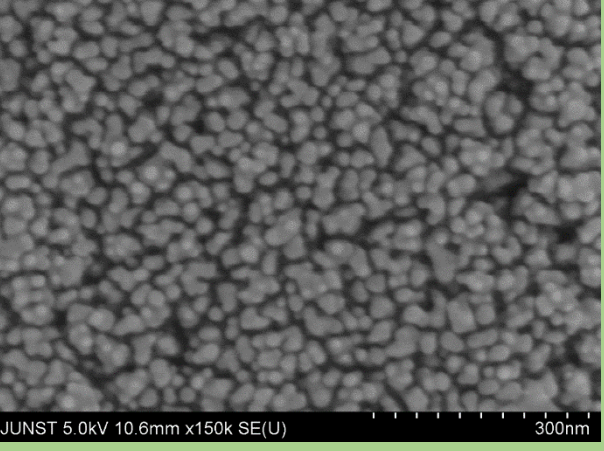
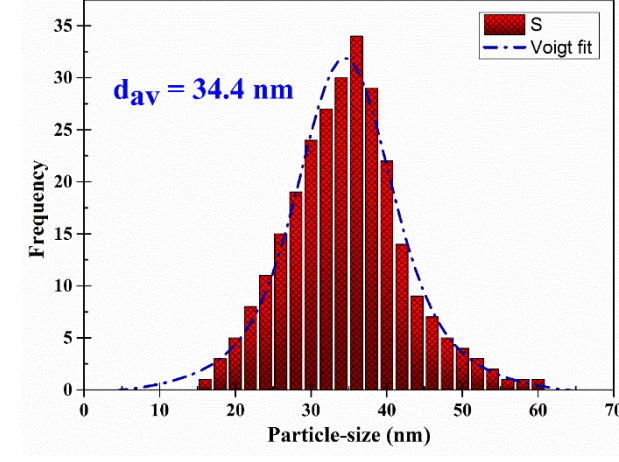
**Fig.5.11** FE-SEM images of B2  $\text{Fe}_3\text{O}_4$  nanoparticles

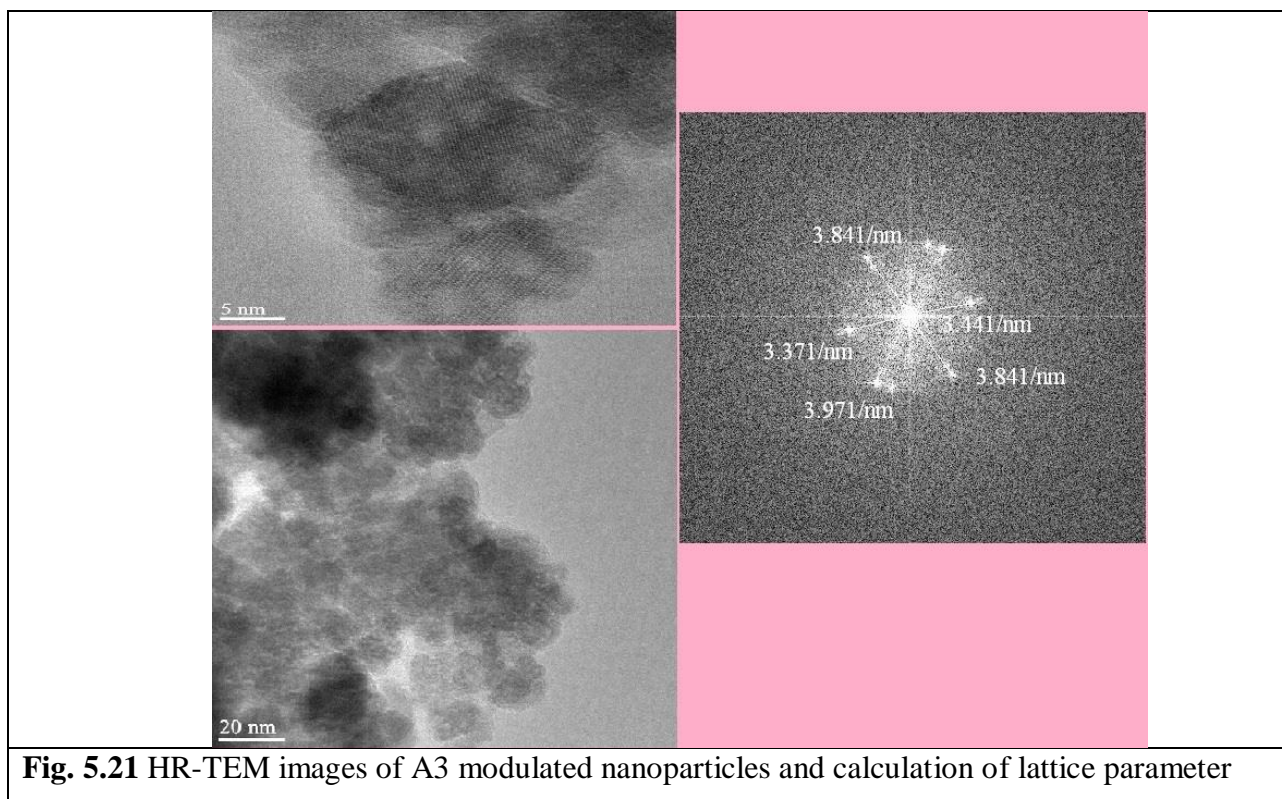
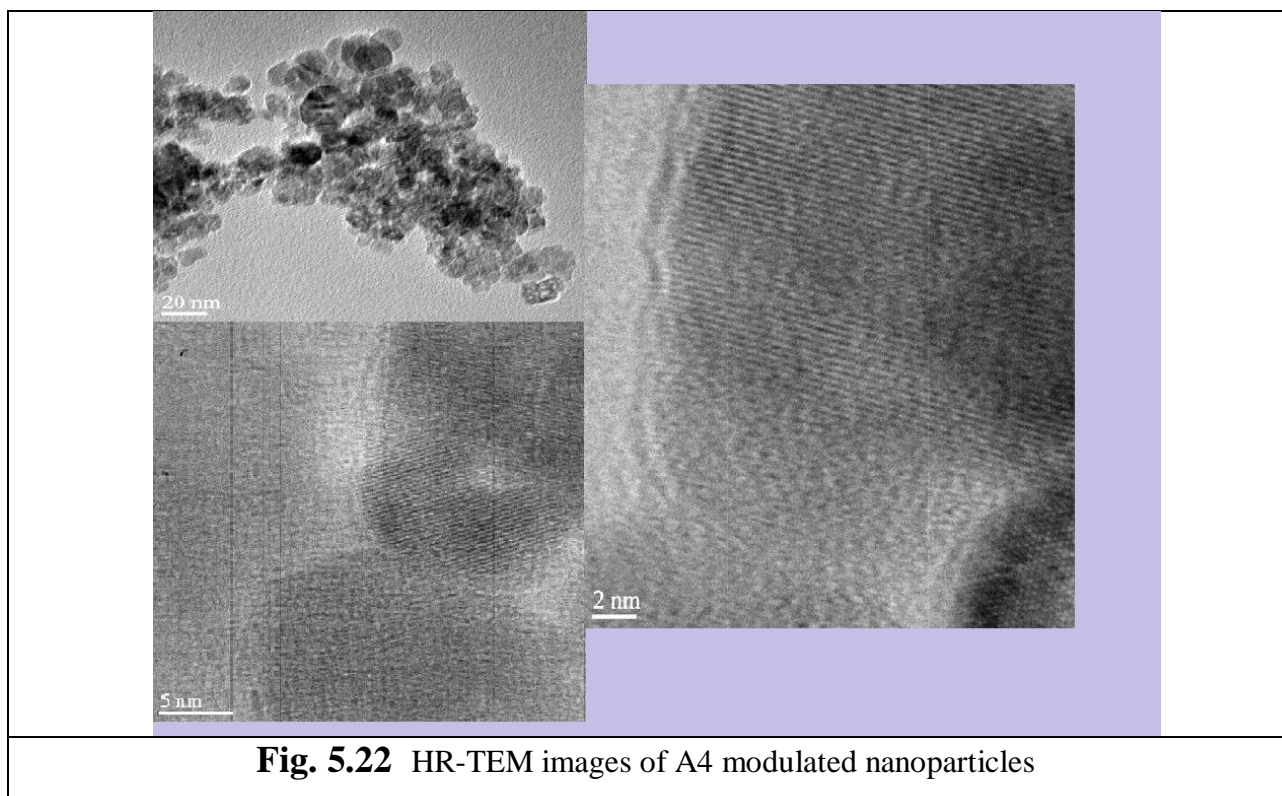


**Fig.5.12** Size distribution of B2  $\text{Fe}_3\text{O}_4$  nanoparticles

<b>C1</b>	 <p><b>Fig.5.13</b> FE-SEM images of C1 Fe<sub>3</sub>O<sub>4</sub> nanoparticles</p>	 <p><b>Fig.5.14</b> Size distribution of C1 Fe<sub>3</sub>O<sub>4</sub> nanoparticles</p>
<b>C2</b>	 <p><b>Fig.5.15</b> FE-SEM images of C2 Fe<sub>3</sub>O<sub>4</sub> nanoparticles</p>	 <p><b>Fig.5.16</b> Size distribution of C2 Fe<sub>3</sub>O<sub>4</sub> nanoparticles</p>

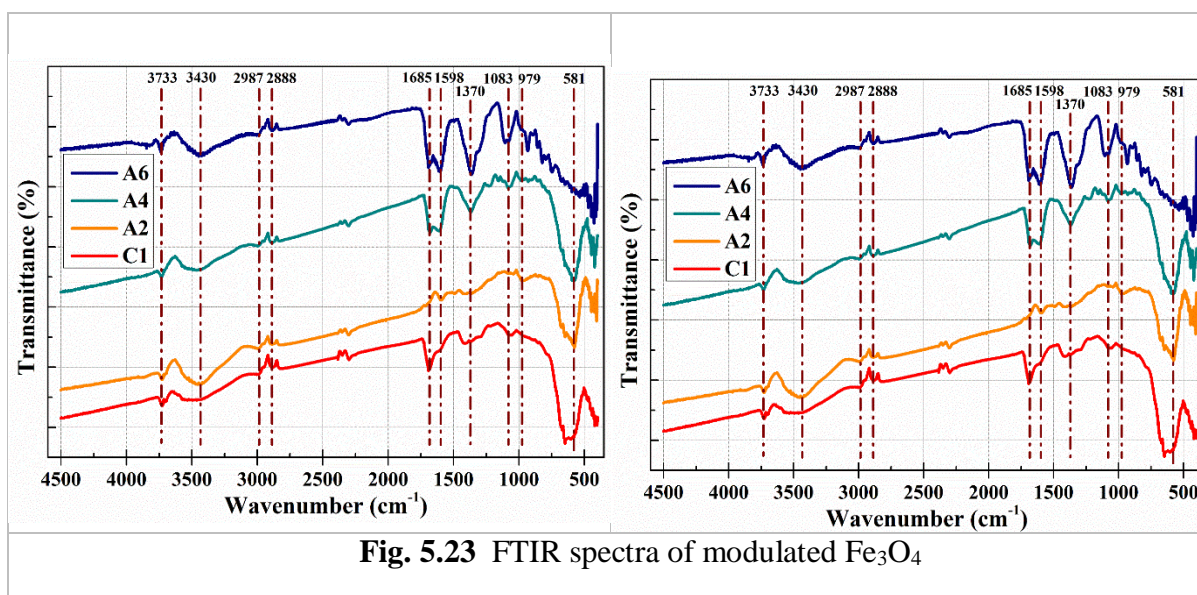


<b>C3</b>		
<p><b>Fig.5.17</b> FE-SEM images of C3 Fe<sub>3</sub>O<sub>4</sub> nanoparticles</p>	<p><b>Fig.5.18</b> Size distribution of C3 Fe<sub>3</sub>O<sub>4</sub> nanoparticles</p>	
<b>S</b>		
<p><b>Fig.5.19</b> FE-SEM images of S Fe<sub>3</sub>O<sub>4</sub> nanoparticles</p>	<p><b>Fig.5.20</b> Size distribution of S Fe<sub>3</sub>O<sub>4</sub> nanoparticles</p>	

**HR-TEM****Fig. 5.21** HR-TEM images of A3 modulated nanoparticles and calculation of lattice parameter**Fig. 5.22** HR-TEM images of A4 modulated nanoparticles

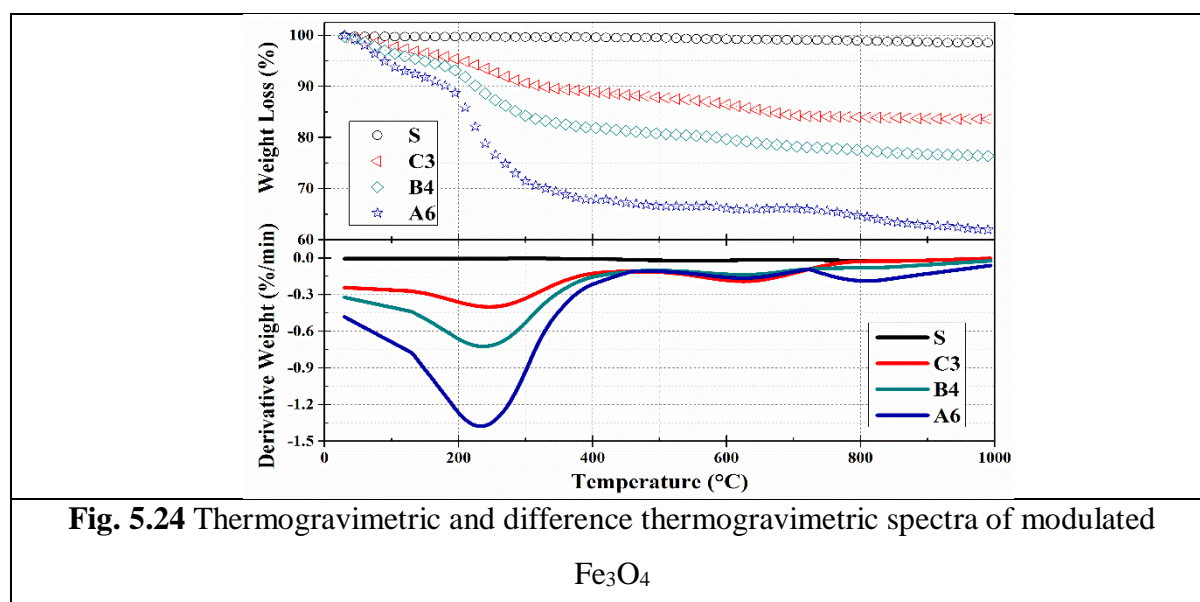
## 5.9 Fourier-transform infrared (FT-IR) spectroscopy

The coordinative effect of carboxylate groups in the surface-composition was further verified by FT-IR spectra, collected from Shimadzu FTIR-8400S. The spectra showed characteristic absorption peaks at 581 and 1370  $\text{cm}^{-1}$  due to Fe-O bending and stretching vibrations respectively. The peak at 979  $\text{cm}^{-1}$  is assigned to the bending vibrations of =C-H and C-C-O groups, whereas the 1083  $\text{cm}^{-1}$  peak is due to CO-C axial deformation and aliphatic bending vibrations of C-C-H groups. The peaks at 1598 and 1685  $\text{cm}^{-1}$  are attributed to -COO-stretching, bending vibrations of water molecules absorbed on the surface of  $\text{Fe}_3\text{O}_4$  NP's and C=O stretching. The symmetric and asymmetric stretching of the methylene (=CH<sub>2</sub>) group and C-H stretching caused peaks at 2888 and 2987  $\text{cm}^{-1}$ . Finally, the bands at 3430 and 3733  $\text{cm}^{-1}$  appeared due to the stretching and bending vibrations of the -OH groups, which are also the characteristic peaks of PEG-6000. Hence, the FT-IR spectra confirms the successful formation of tartrate coated-PEGylated  $\text{Fe}_3\text{O}_4$  NP's.



## 5.10 Thermogravimetric Analysis (TGA) & Difference Thermogravimetry (DTG)

To further explore thermal degradation behaviour and coating nature of PEG & tartrate, about 15mg of four chosen powder-samples, including the commercial one, were elucidated by TGA-DTG (Perkin Elmer Diamond Pyris 480). It is well-known that, in presence of open air or oxygen, pure  $\text{Fe}_3\text{O}_4$  gets oxidized very easily under heat-treatment and generates  $\text{Fe}_2\text{O}_3$  polymorphs. This process gets decelerated acted by suitable organic coating or in presence of inert atmosphere. For a quantitative overview of the carboxylate groups bound around the NP-surface and TGA was performed in  $\text{N}_2$ -atmosphere from room-temperature to  $1000^\circ\text{C}$  in 2hrs duration.



A large weight loss of about 38 wt% was observed for the smallest NP's. In contrast, much smaller loss was found for the solvothermally prepared sample with lesser amount of surfactants. The commercial sample without surface-functionalization; produced almost no loss of weight in  $\text{N}_2$ . It is thus demonstrated that considerable amounts of carboxyl salt would bind to the surface of the NP's. The weight loss below  $200^\circ\text{C}$  might be attributed to the adsorbed water in the samples. The main weight loss at  $200\text{--}300^\circ\text{C}$  was due to the decomposition of tartrate, whereas PEG undergoes a slow and steady decomposition in the range  $180\text{--}900^\circ\text{C}$ . The small peak near  $630^\circ\text{C}$  could be because of reduction to  $\text{FeO}$ , which is thermodynamically more stable than  $\text{Fe}_3\text{O}_4$  above  $570^\circ\text{C}$  in phase-diagram of the Fe-O system.

Another tiny derivative peak near 800°C possibly arose due to the deoxidation of FeO in N<sub>2</sub> environment.

## 5.11 Raman spectroscopy

As magnetite (Fe<sub>3</sub>O<sub>4</sub>) and maghemite (γ-Fe<sub>2</sub>O<sub>3</sub>) exhibit near-similar XRD patterns due to similar spinel structure (except for vacancy-states), the composition of the as-synthesized NP's was further verified by Raman spectroscopy, which is practically capable of characterizing the finger-print vibration-modes of the molecules. Micro-Raman (beam-diameter ≅ 1 μm) spectra was recorded and analyzed by a WITec ALPHA300 RS confocal spectrometer in backscattering configuration. The UHTS 300 spectrograph is connected to a Peltier-cooled back-illuminated charge-coupled device (CCD), operated at -62°C with better than 90% QE in the visible excitation. A solid-state frequency doubled Nd:YAG laser (532.3 nm) was used as the excitation source, having a maximum power of 30mW. Data was acquired using a 50X (N.A. = 0.9) achromatic objective (Zeiss) with 600 groove/mm grating (spectral resolution = 3.3 cm<sup>-1</sup>) by averaging 10 spectral acquisitions with 6sec of integration-time each. The wavenumber error is considered ±1.5 cm<sup>-1</sup> for our calculations. No polarizers were used, but holographic supernotch filters were employed to reject the Rayleigh and anti-stokes lines. Choice of laser power and data acquisition-time are vital parameters for Raman spectroscopy of Fe<sub>3</sub>O<sub>4</sub>, as thermal phase-changes by partial oxidation are easily induced by the excitation laser in open air. For acquisition times longer than a minute with ≥ 5mW laser power; features of maghemite, followed by hematite were observed with time in the collected spectra (not shown). The three principle polymorphs of iron oxides can be obtained simply by heating magnetite in presence of oxygen to specific temperature as:  $Fe_3O_4 \xrightarrow{\geq 200^\circ C} \gamma - Fe_2O_3$   
 $\xrightarrow{\geq 450^\circ C} \alpha - Fe_2O_3$ . The laser-beam with micron-order diameter causes local heating at specific points of sample under observation, which easily reaches the threshold temperature for a phase-change. Shebanova and Lazor have in fact studied laser-induced oxidation of Fe<sub>3</sub>O<sub>4</sub> varying laser-power and time of measurements. Although it was observed that, our samples with higher concentration of surfactants are less prone to get oxidised, which ceases to compromise sample-quality in ambient atmosphere.

Magnetite's irreducible normal modes of vibration, considering its inverse cubic spinel structure for the first Brillouin zone-center are given by,

$$\Gamma_{vib} = A_{1g} + E_{1g} + T_{1g} + 3T_{2g} + 2A_{2u} + 2E_u + 4T_{1u} + 2T_{2u}$$

The pronounced peak near  $670\text{ cm}^{-1}$  is attributed to the  $A_{1g}$  mode, whereas the features at 201, 318 and  $542\text{ cm}^{-1}$  are very weak in all spectra and are assigned to the three  $T_{2g}$  vibrational modes. There was a clear red-shift ( $13.48\text{ cm}^{-1}$ ) and higher degree of asymmetry in the  $A_{1g}$  peak with a decrease in particle-size from 150 to 4 nm.

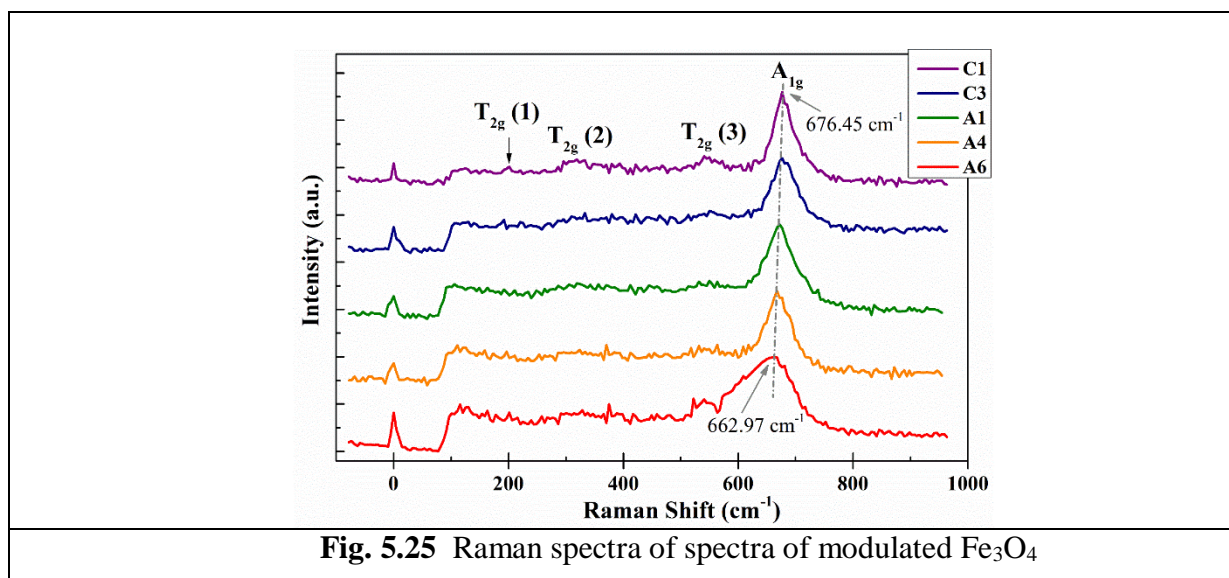


**Fig. 5.25** Raman spectra of spectra of modulated  $\text{Fe}_3\text{O}_4$

The Raman line-shape of  $A_{1g}$  mode for bulk sample is lorentzian, but as the particle-size decreases below 15 nm, a thorough downshift and asymmetric broadening at the low-frequency side was observed, which can be better described by the Breit-Wigner-Fano (BWF) profile, popularly known as Fano asymmetry. If the oscillators are interacting with other modes or a continuum of modes, then the line shape may be strongly altered owing to this coupling and the actual spectral shape depends on the electron-phonon coupling strength. Such asymmetric peaks can be caused by 3 reasons: (a) a laser heating effect causing Fano interference between optical phonon scattering from the  $q=0$  plane and electronic continuum scattering due to the laser-induced electrons in the conduction band. Gupta et al has described this effect on Si nanowire samples for  $>3\text{mW}$  laser power. But, certainly this is not our case, as to avoid oxidation the laser power was intentionally chosen to have the minimum value. (b) Disorder effects leading to reduced phonon correlation length. In disordered systems, the lack of translational invariance induces the activation of forbidden modes. But, pure  $\text{Fe}_3\text{O}_4$  samples gone through surfactant-controlled growth are less likely to produce high disorder. (c) Phonon confinement (quantization) effect: In Richter's phonon confinement model (PCM), the confinement of the phonon wave function leads to a breakdown of phonon selection rule at the

Brillouin zone-center ( $q=0$ ) as found in bulk material. The relaxation in selection rules due to confinement induced uncertainty can result similar effects. As a result, other phonons having different frequencies from the same branch are “activated”, leading to an asymmetric broadening and red-shifting of the Raman band as prescribed by Campbell and Fauchet’s modified model (MPCM). Intensity is calculated by appropriately choosing weighing functions and integration limits on the wave-vector. The Raman intensity as a function of frequency ( $\omega$ ) and crystallite size ( $d$ ) can be expressed as:

$$I(\omega, d) = A \frac{\rho(\omega)}{d^3} \int_{2\pi-1}^{2\pi+1} \frac{4\pi q^2 \left[ \frac{\sin(q/2)}{q(4\pi^2 - q^2)} \right]^2 \left(\frac{\Gamma}{2}\right)}{[\omega - \omega'(q)]^2 + \left(\frac{\Gamma}{2}\right)^2} dq$$

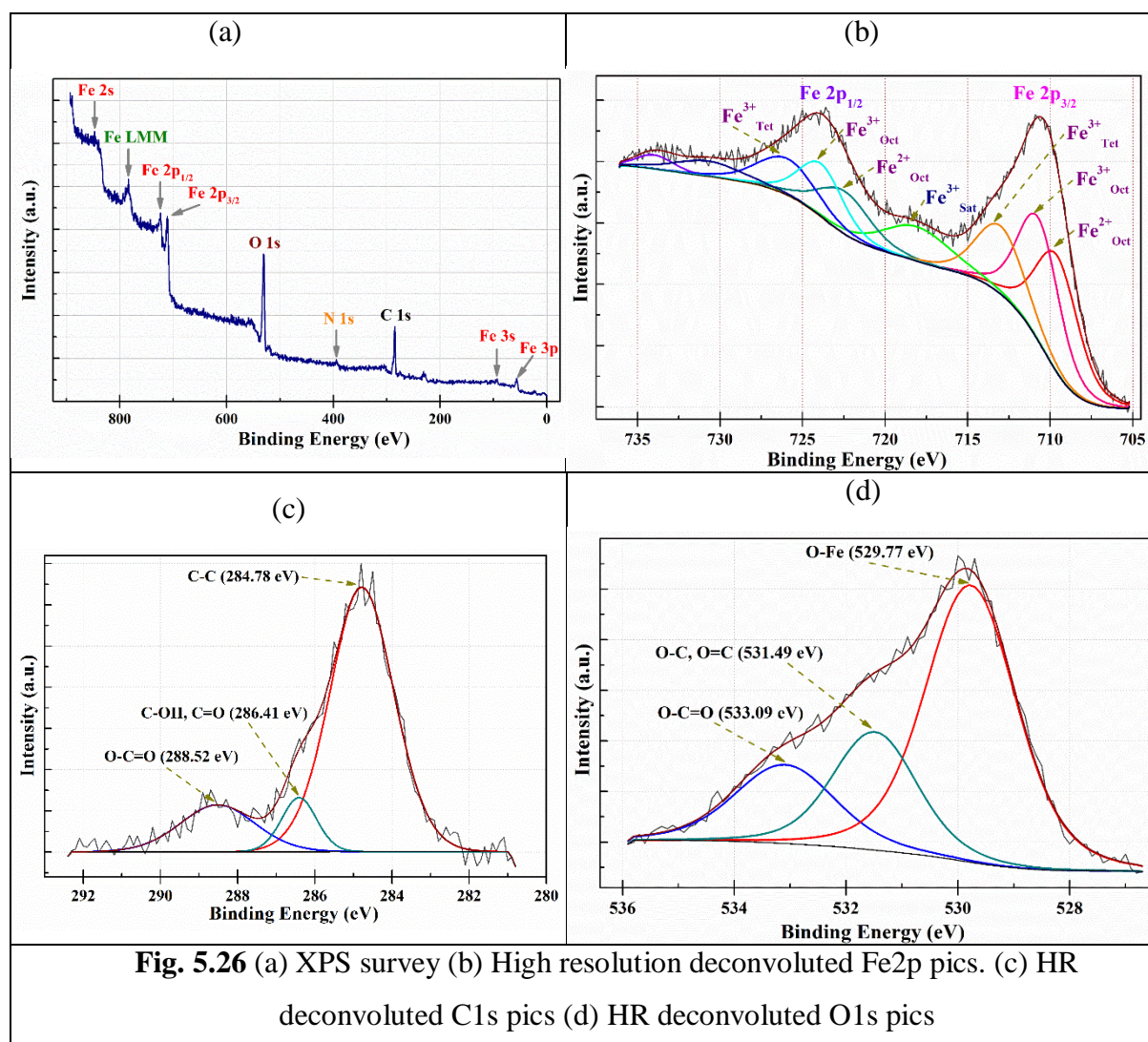
where a suitable dispersion relation is required depending on the material for  $\omega'(q)$ ,  $\rho(\omega)$  corresponds to Bose-Einstein occupancy,  $\Gamma$  is the asymmetric line-width i.e., the sum of symmetric and asymmetric half-widths and  $A$  is a constant. In this model, the fundamental requirement of phonon confinement is: the phonon mean free path must be greater than the particle-size; which is satisfied for the smallest NP’s.

## 5.12 X-ray photoelectron spectroscopy (XPS)

The surface composition of PEG/Tartrate coated  $\text{Fe}_3\text{O}_4$  NP’s (Sample-A2) was further characterized by XPS to investigate the nature of the surfactant molecules chemisorbed to the surface and to substantiate the effects of the capping agents on sample-quality, stability, and stoichiometry. Data was obtained using a Kratos AXIS ULTRA XPS (monochromated Al source; 117 W). The survey scans and high-resolution elemental scans for XPS analysis were carried out with pass energy of 160 eV in steps of 1 eV and 20 eV in steps of 0.1 eV respectively. A thorough survey shows Fe 2s, 2p, 3s and 3p-peaks along with an Auger peak; as well as peaks of 1s orbitals of C and O. Using CasaXPS software, calculation of atomic percentage revealed, synthesis of almost stoichiometric magnetite ( $\text{Fe}_{2.97}\text{O}_4$ ) – which is not abundant in scientific literature. The off-stoichiometry parameters ( $\delta$ ) for non-stoichiometric magnetite [ $\text{Fe}_{3(1-\delta)}\text{O}_4$ ] did not exceed 0.02 for the tested samples of different size, which indicates that, the oxidation state of Fe is not affected by the surface-to-volume ratio, which is similar to the findings of Lee et al.

The  $2p_{3/2}$  peak of high-spin ferrous/ferric compounds undergoes broadening compared to metallic  $Fe^{(0)}$  or low-spin  $Fe^{2+}$ . Gupta and Sen explained this broadness as an outcome of electrostatic interactions and spin-orbit coupling among the 2p-core hole and unpaired 3d electrons inside the photoionized cation due to crystal field interactions. While analysing high-pressure behaviour of magnetite, Bengtson et al has established the spin-state of iron in  $Fe_3O_4$  to be high based on *ab initio* calculations. Moreover, partially filled d-orbitals cause complex multiplet splitting, also contributing to the peak-structure. Hence for rigorous analysis, the high resolution XPS spectra of Fe  $2p_{1/2}$  and  $2p_{3/2}$  peaks have been deconvoluted into 3 components each (keeping in mind, the simultaneous presence of 2+ and 3+ oxidation states with 2 species having tetrahedral and octahedral occupancies) plus 3 satellite peaks with a squared deviation of  $\chi^2 = 0.98$  using a Shirley background. The  $2p_{3/2}$  peak is a convolution of 3 components viz., 709.57 ( $Fe_{Oct.}^{2+}$ ), 710.71 ( $Fe_{Oct.}^{3+}$ ) and 713.01 eV ( $Fe_{Tet.}^{3+}$ ); whereas the  $2p_{1/2}$  peak can be resolved into components at 722.46 ( $Fe_{Oct.}^{2+}$ ), 723.88 ( $Fe_{Oct.}^{3+}$ ) and 725.93 eV ( $Fe_{Tet.}^{3+}$ ). These values are comparable to others pieces of literature. The satellite at 718.08 eV is assigned to the surface-peak of maghemite ( $\gamma$ - $Fe_2O_3$ ) due to unavoidable partial oxidation on the outer surface of NP's, common in most transition metal oxides. Using CasaXPS software, the ratio of relative intensities of the three iron species was found to be  $Fe_{Oct.}^{2+}:Fe_{Oct.}^{3+}:Fe_{Tet.}^{3+} = 1:1.03:0.77$ , which is quite close to the predicted unity ratio. The little higher  $Fe^{2+}/Fe^{3+}$  ratio could be attributed to the surface reduction under ultrahigh vacuum conditions.



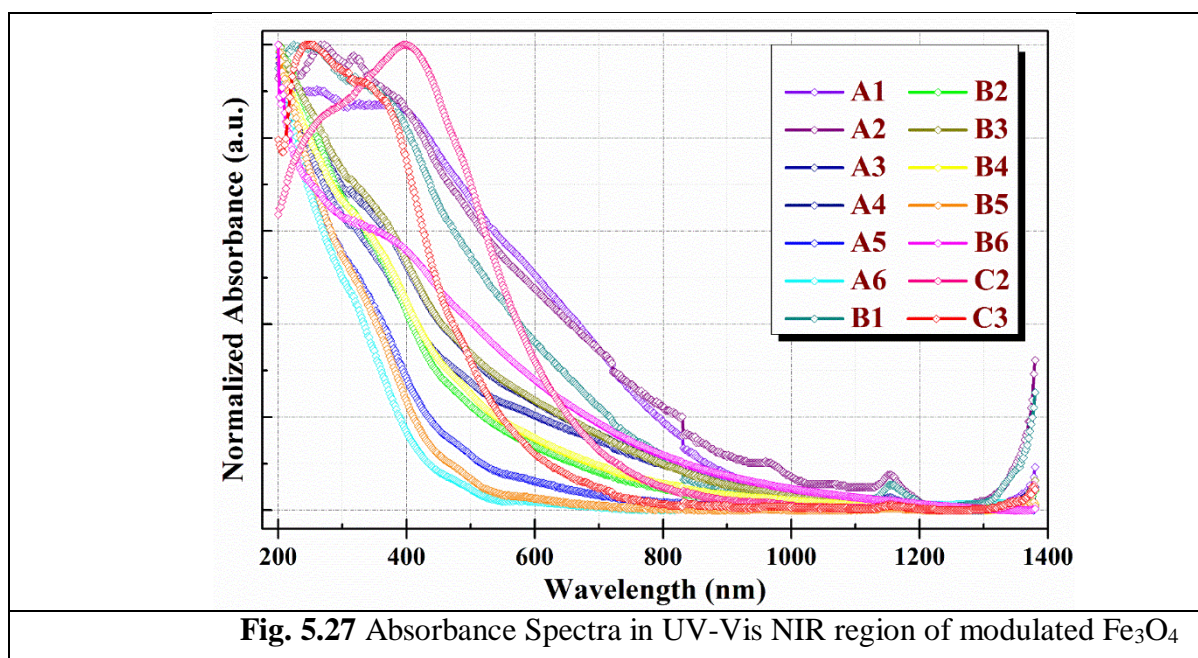


The O 1s XPS spectrum has been fitted into 3 peaks having binding energies 529.77, 531.49 and 533.09 eV with a squared deviation of  $\chi^2 = 0.91$ . The most intense peak at 529.77 eV corresponds to the lattice oxygen in Fe<sub>3</sub>O<sub>4</sub>. The remaining two peaks result from oxygen atoms in mono/bidentate carboxylate groups present in the surfactants used. The high-resolution C 1s spectrum displays another three peaks at 284.78, 286.41 and 288.52 eV. The most intense one at 284.78 eV is assigned to carbon atoms of aliphatic –C–C bonds, while the rest two are attributed to –C–OH, –C=O and –O–C=O groups present in PEG and tartrate ions respectively.

## 5.13 UV-Vis-NIR Spectroscopy

Absorption spectra of the as-prepared samples were collected using a stable aqueous dispersion by employing a Shimadzu UV 3600 UV-Vis-NIR Spectrophotometer, whereas diffuse reflectance spectrum (DRS) of the commercial sample (S) was obtained using BaSO<sub>4</sub> as a reflectance standard. The samples show a broad absorption pattern at 200-600 nm, mainly in

the UV-range, which is attributed to the d-orbital transitions of  $\text{Fe}_3\text{O}_4$ . Thereafter a gradual downfall with increasing wavelength took place, except for a small peak near 1150nm; which can be ascribed to the electron-traps in the tetrahedral sites; originated because of oxygen-vacancies. The allowed direct optical band-gap ( $E_g$ ) can be calculated using Tauc's equation, given by:  $(\alpha h\nu)^2 = A^2(h\nu - E_g)$ , where  $\alpha$  is the absorption coefficient and A is a proportionality constant. By plotting  $(\alpha h\nu)^2$  vs  $h\nu$ , a straight line is obtained at the absorption band-edge, by extrapolating which, for  $\alpha = 0$ ,  $E_g = h\nu$  is determined. A continuous increase of band-gap from 1.59 to 4.78 eV was observed with decreasing particle-size from bulk to quantum regime. In bulk material, bands actually are quasi-continuous energy levels of a large ( $\sim 10^{23}$ ) number of atoms/molecules. As the particle size reaches nano regime, where every particle is made up by only a tiny number of atoms or molecules, the number of overlapping orbitals or energy levels decreases and the width of the band gets narrower. This causes an increase in energy-gap b/w the valence band and the conduction band, which explains the higher band-gap ( $E_g$ ) in NP's than its bulk counterpart. As the width of the forbidden region increases, the electrons' motion gets more and more restricted. Hence NP's exhibit lower electrical conductivity than the bulk. So, there is a blue-shift of absorption spectrum with decreasing particle-size.



Several researchers in theoretical, as well as experimental perspectives have probed the electronic band-gap ( $\sim 0.1 - 0.3$  eV) of magnetite above Verwey transition, but it is too small (causing half-metallicity) to interfere with light of UV-Vis range. Hence, the optical band-gap

determined from absorption spectra is not the electronic gap b/w valence band maxima and conduction band minima, rather corresponds to the optical transitions among crystal field bands of the octahedral and tetrahedral sites, composed of 3d metal atomic orbitals. Jordan *et al.* employing scanning tunnelling spectroscopy on specific crystal planes of single crystalline magnetite have shown that. surface disorder and nonstoichiometry can alter the electronic signature of magnetite and calculated exchange energy ( $\Delta_{ex}$ ) between the crystal field levels of the associated majority and minority spins. From laser-excited photoluminescence spectra; Sadat *et al.* proposed a model of Fe(3d) levels sub-merged between the valence band of O(2p) and empty Fe(4s) levels, separated by an energy-gap of 4-6 eV. Figure-5(d) shows the possible transitions in an approximate band structure of Fe<sub>3</sub>O<sub>4</sub> NP's based on both experimental and theoretical DOS studies, which supports the range of band-gap so obtained with variation in size. The octahedral splitting energy ( $\Delta_{cf(o)}$ ) is larger than the tetrahedral species ( $\Delta_{cf(t)}$ ) due to its geometry and mainly contributes in the optical transitions [ $e_g \leftrightarrow t_{2g} \leftrightarrow O(2p)$ ]. The splitting energies are size-dependent and trap-states in between play a major role in the whole process.

For ultra-small nanoparticles, quantum confinement and excitonic effects often play a dominant role in optical properties at room-temperature in contrast to bulk semiconductors. In the strong confinement regime, the electrons and holes are treated as individual particles and the Hamiltonian for such low-dimensional systems are given by:  $H = -\frac{\hbar^2}{2m_e^*}\nabla_e^2 - \frac{\hbar^2}{2m_h^*}\nabla_h^2 + V_e + V_h - \frac{e^2}{4\pi\epsilon|r_e-r_h|}$ ; where effective masses of electrons and holes are  $m_e^*$  &  $m_h^*$  and  $\epsilon$  is the permittivity. Nanda *et al.* have used the effective mass approximation (EMA) with finite-depth square-well potential to scrutinize the size-dependent band gap (SDBG) for narrow and wide band-gap semiconductor candidates and found that EMA is more suitable for near-insulating materials having lower dielectric constant. For semiconductors with larger dielectric constant and carrier-density, quantum effects can be estimated more precisely using the excitonic model and the Brus equation given by,

$$E_g^{(nano)}(r) = E_g^{(bulk)} + \frac{\hbar^2}{8r^2} \left( \frac{1}{m_e^*} + \frac{1}{m_h^*} \right) - \frac{1.786e^2}{4\pi\epsilon r}$$

$$\therefore \Delta E_g(d) = \frac{\hbar^2}{2\mu^* d^2} - \frac{1.786e^2}{2\pi\epsilon_0\epsilon_r d}, \quad \text{where } d = 2r, \frac{1}{\mu^*} = \frac{1}{m_e^*} + \frac{1}{m_h^*} \text{ and } \epsilon_r = \epsilon/\epsilon_0$$

for spherical particles of diameter  $d$  and  $\mu^*$  being the reduced effective mass of the electron-hole system. The first term in the equation represents the particle-in-a-box quantum localization energy ( $\sim 1/r^2$ ), whereas the 2<sup>nd</sup> term describes the binding energy of an exciton due to Coulomb attraction ( $\sim 1/r$ ). Materials like  $\text{Fe}_3\text{O}_4$  having small carrier effective mass and large dielectric constant, the first term predominates. The optical band-gaps so obtained for the smaller NP's have been well-fitted with Brus equation for suitable values of  $\mu^*$  and  $\epsilon_r$ , acceptable in accordance to previously reported values.

The Urbach energy basically characterizes the extent of the exponential tail of the absorption edge and gives a measure of defect-density & trap-states present in the crystal that originates from thermal vibrations in the lattice, static/induced disorder & impurities. Hence, it depends on temperature, strength of ionic bonds and average photon energies. But, the main factor contributing to edge broadening in the crystalline materials is exciton-phonon coupling (dynamic disorder). The onset of exponential absorption tail ( $E_0$ ) and Urbach energy ( $E_u$ ) is given in accordance with the empirical relation b/w absorption co-efficient ( $\alpha$ ) and absolute temperature (T):

$$\alpha = \alpha_0 \exp \left\{ \frac{\sigma}{k_B T} (E - E_0) \right\} = \alpha_0 \exp \left( \frac{E - E_0}{E_u} \right), \quad \text{where } E_u = \frac{k_B T}{\sigma}$$

Therefore, taking logarithm in both sides, we get:  $\ln \alpha = \ln \alpha_0 + \frac{\sigma}{k_B T} (E - E_0)$ , where  $\sigma$  is the steepness parameter and  $k_B$  is Boltzman constant. So, by plotting  $\ln \alpha$  vs  $E (= hc/\lambda)$ , we get a straight line with slope =  $\frac{\sigma}{k_B T}$ , the reciprocal of which determines Urbach energy. In our case,  $E_u$  depends on a number of factors such as crystal growth-time, concentration of surfactants, particle-size and surface to volume ratio. Decreasing reaction-time and increasing surface to volume ratio originates higher defect-density on the surface, whereas higher concentration of tartrate and PEG regularizes the growth-dynamics and controls unnecessary defects. Hence, although initially increases; an overall decreasing trend of  $E_u$  was observed with smaller size of NP's. The onset of absorption ( $E_0$ ) on the other hand does not explicitly depend on particle-size, but is quite close to the crystal-field splitting energy of the octahedral sites.

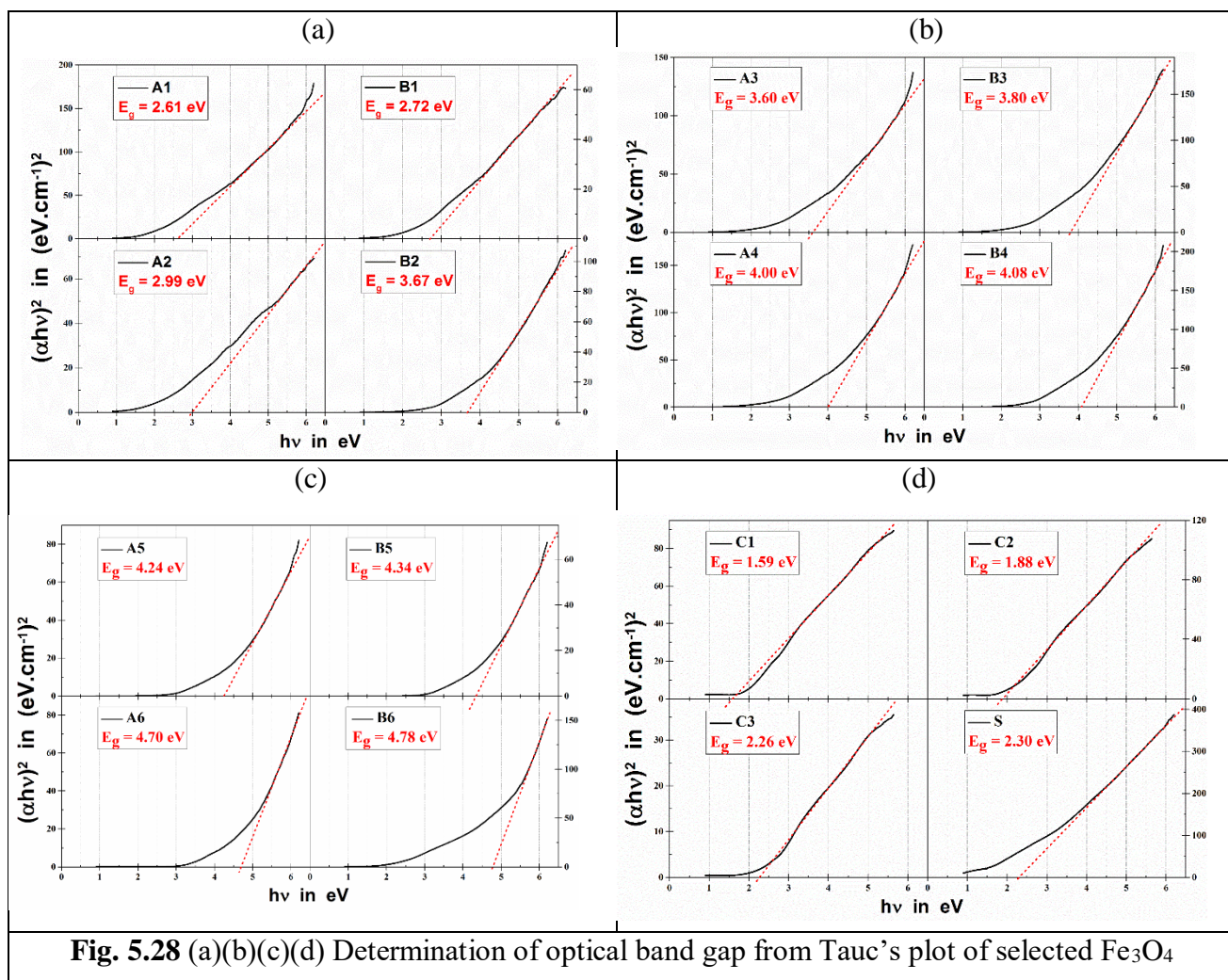


**Fig. 5.28** (a)(b)(c)(d) Determination of optical band gap from Tauc's plot of selected  $\text{Fe}_3\text{O}_4$

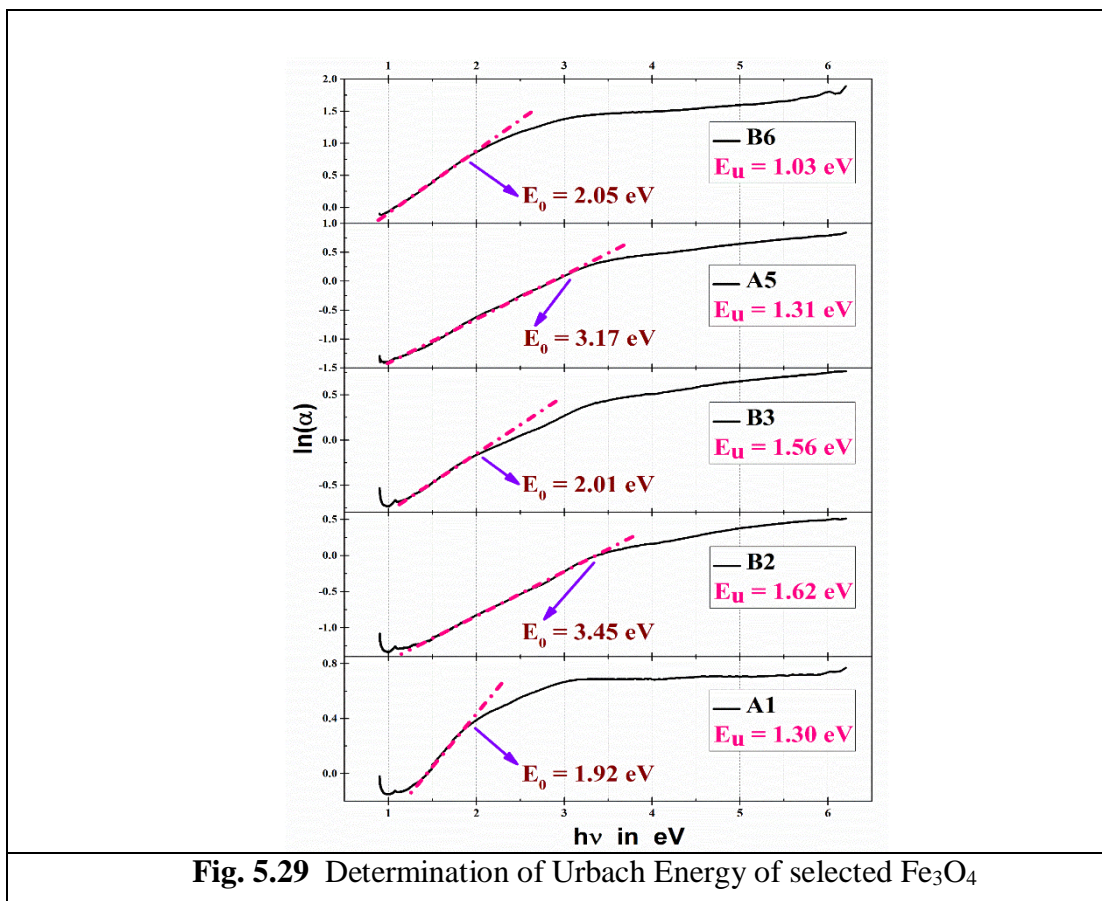


**Fig. 5.29** Determination of Urbach Energy of selected Fe<sub>3</sub>O<sub>4</sub>

# **CHAPTER-6**

**Self-poled Fe<sub>3</sub>O<sub>4</sub>/PVDF composites for piezoelectric nanogenerator applications**

## 6.1 Introduction and Objective

In the era of depleting fossil-fuel; scavenging alternative energy-sources such as solar or fusion-energy and mechanical/chemical energy-harvesting and storage have topped the priorities of materials research. Since the last decade; polymers, 2D materials and different composites have been satisfactorily explored for enhancement of supercapacitor and nanogenerator-based applications. Use of electroactive polymers with high dielectric constant and their composites for cost-effective, flexible, wearable, biocompatible, self-powered nano-devices has truncated considerable attention in this regard. Among these, poly(vinylidene fluoride) {PVDF} and its copolymers, well-known for their promising piezo-, pyro- and ferro-electric response, have been classified as a model-system in fabrication of easily scalable high power-density nanogenerators with intrinsic reciprocal conversion capability. To improve compatibility with smart textiles, these devices owe to have suitable magnetic properties for shielding from electromagnetic interference (EMI) in specific applications.  $\text{Fe}_3\text{O}_4$  is not only a superior magnetic material, but also acts as an electret; which can store charge temporally to enhance electroactive response of the system. Im and Park have recently fabricated mechanically robust magnetic  $\text{Fe}_3\text{O}_4$ /PVDF composite nanofibers to boost its triboelectric performance up. PVDF; a semi-crystalline polymer; consists of mainly five different crystalline polymorphs viz.  $\alpha$ ,  $\beta$ ,  $\gamma$ ,  $\delta$ , and  $\epsilon$ -phase. While in ambient conditions, the energetically favourable alternate trans-gauche (TGTG) non-polar  $\alpha$ -phase is the predominant constituent; tensile stretching, high electric field poling or embedding polar nanoparticles can enhance the planer all-trans (TTTT) pseudo-hexagonal  $\beta$ -phase with largest spontaneous polarization. This is because, the parallelly aligned dipole moments associated with C–H & C–F bonds; perpendicular to the carbon backbone add up altogether to produce the net moment. So, as-synthesized surface-functionalized  $\text{Fe}_3\text{O}_4$  NP's with moderate surface-charge are expected to intensify the  $\beta$ -phase contributions as a filler material also.[2]



## 6.2 Fabrication of self-poled standalone Fe<sub>3</sub>O<sub>4</sub>/PVDF composite nano generators

Im and Park prepared samples with different weight-percentage (0-30%) of commercial Fe<sub>3</sub>O<sub>4</sub> NP's and produced best results in between 5-11%. In this work, we have chosen NP's of 5 different sizes (8.9, 30.2, 45.1, 78.6 and 149.0 nm) and 3 different amounts (4, 8 and 12%) to produce 15 self-poled thin films by a simple solvent-casting technique and compared their piezoelectric performance in reference to pure PVDF film. 1.5 gm of PVDF powder along with as-calculated amount of Fe<sub>3</sub>O<sub>4</sub> had been vigorously stirred in a solution of 12 ml acetone and 8 ml N,N-dimethylformamide (DMF) at 85°C for 2 hours and thereafter transferred onto glass-slides homogeneously. The slides are put to drying at 80°C in rough vacuum for 24 hrs without any mechanical disturbance.[4][5] Finally, the dry stand-alone thin films are separated out of the slides and employed for fabrication of flexible nanogenerators with thin aluminium electrodes.

## 6.3 Basic Characterization

The successful formation of Fe<sub>3</sub>O<sub>4</sub>/PVDF composite and quantitative analysis of the enhancement of  $\beta$ -phase with respect to  $\alpha$ -phase have been confirmed from XRD, FTIR and Raman spectra given in figure-8(a), (b) and (c) (for 30.2 nm particles only). XRD pattern of pure PVDF reveals the preponderance of  $\alpha$ -phase with the characteristic (100), (110), (021) and (002) peaks at  $2\theta = 17.99^\circ, 19.90^\circ, 26.56^\circ$  and  $39.03^\circ$  respectively. Weak traces of  $\beta$  and  $\gamma$ -phases [(020) & (002)] were also detected, among which the (110) or (200) plane at  $20.28^\circ$ , characteristic of  $\beta$ -phase was found to enhance vigorously with magnetite incorporation and for the 8 wt% film dominates over the non-polar counterparts. Although it again gets suppressed a bit for higher concentration of magnetite. With increasing wt%; (311), (220) and (111) planes of Fe<sub>3</sub>O<sub>4</sub> developed gradually.

The key-features of PVDF and its composites can be distinguished on basis of the fingerprint of modes of molecular vibration using FTIR and Raman spectra. There are some infrared active modes, which are common for all the PVDF polymorphs, such as bending, scissoring, symmetric & asymmetric stretching of CH<sub>2</sub>-group and C-C or C-F stretching; whereas some fingerprint modes of  $\alpha$ ,  $\beta$  and  $\gamma$ -phases can be useful in quantitative analysis, as shown in the figure. The gradual augmentation of peaks at  $844$  and  $1278$  cm<sup>-1</sup>; associated with the CH<sub>2</sub>-wagging and CF<sub>2</sub>-symmetric stretching vibrations; indicates formation of  $\beta$ -phase against the

rise of Fe-O bending mode at  $581\text{ cm}^{-1}$ . The evolution of  $\beta$ -bands at  $445\text{ & }510\text{ cm}^{-1}$  and  $\alpha$ -bands at  $764\text{ & }976\text{ cm}^{-1}$  clearly indicates the change in relative proportions, although the  $\gamma$ -bands at  $832\text{ & }1234\text{ cm}^{-1}$  remains unaltered. Embedding  $\text{Fe}_3\text{O}_4$  NP's in PVDF matrix has left the less-polar  $\gamma$ -phase almost unaffected, as seen in all the basic characterizations.

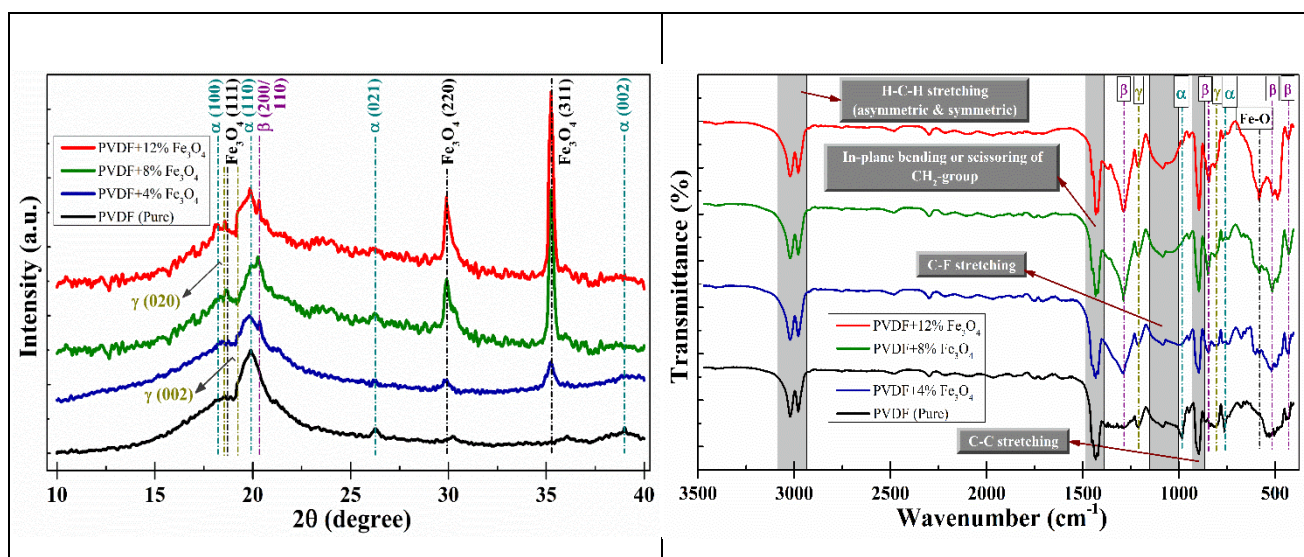


Fig. 6.1 PVDF/Fe<sub>3</sub>O<sub>4</sub> XRD spectra

Fig. 6.2 PVDF/Fe<sub>3</sub>O<sub>4</sub> FTIR spectra

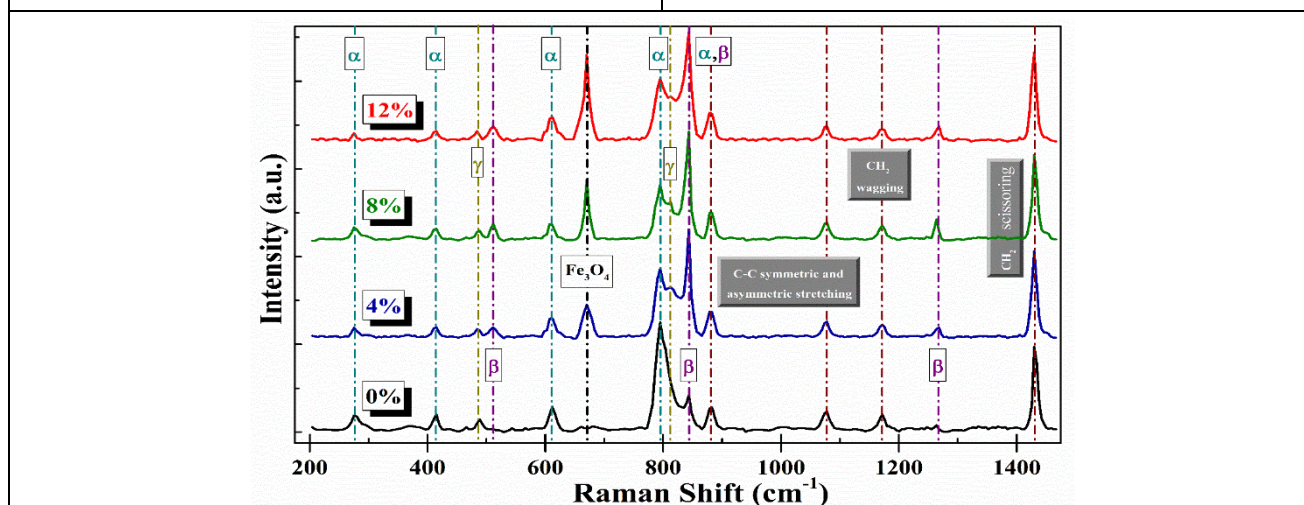
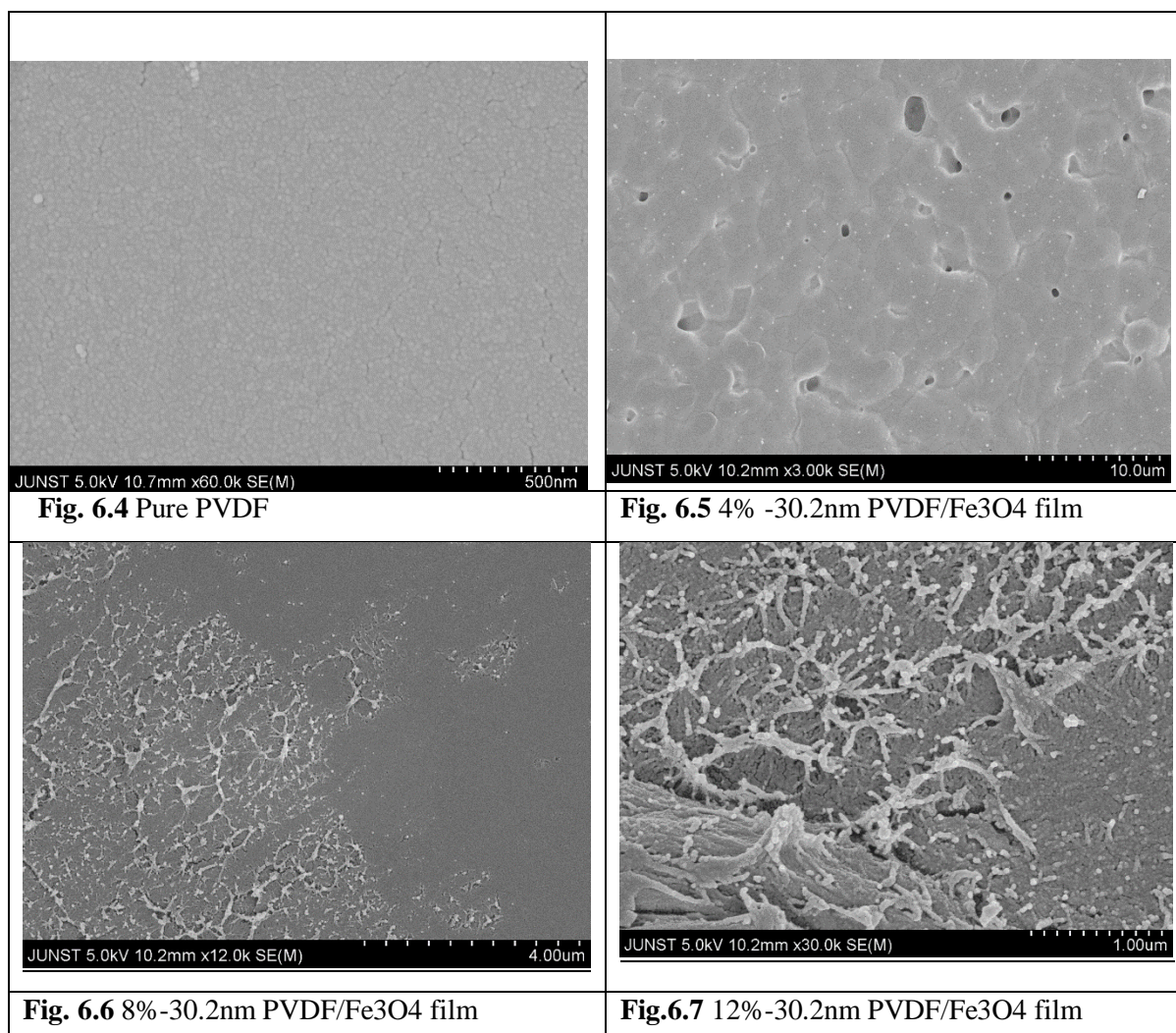


Fig. 6.3 PVDF/Fe<sub>3</sub>O<sub>4</sub> Raman spectra

$\text{Fe}_3\text{O}_4$  nanoparticles could have a tendency to aggregate in case of very high surface energy or large relative proportion. This proposition is supported by the FE-SEM images for different wt (%) films, where we can see a homogeneous and uniform distribution of PVDF in the pure sample. The 4% film is also uniform, except for some tiny porous structures developed for the association of  $\text{Fe}_3\text{O}_4$  NP's. In the 8% sample, gradual aggregation of the nanoparticles initiates at random regions in the films. This effect becomes severe for the 12% film, where the

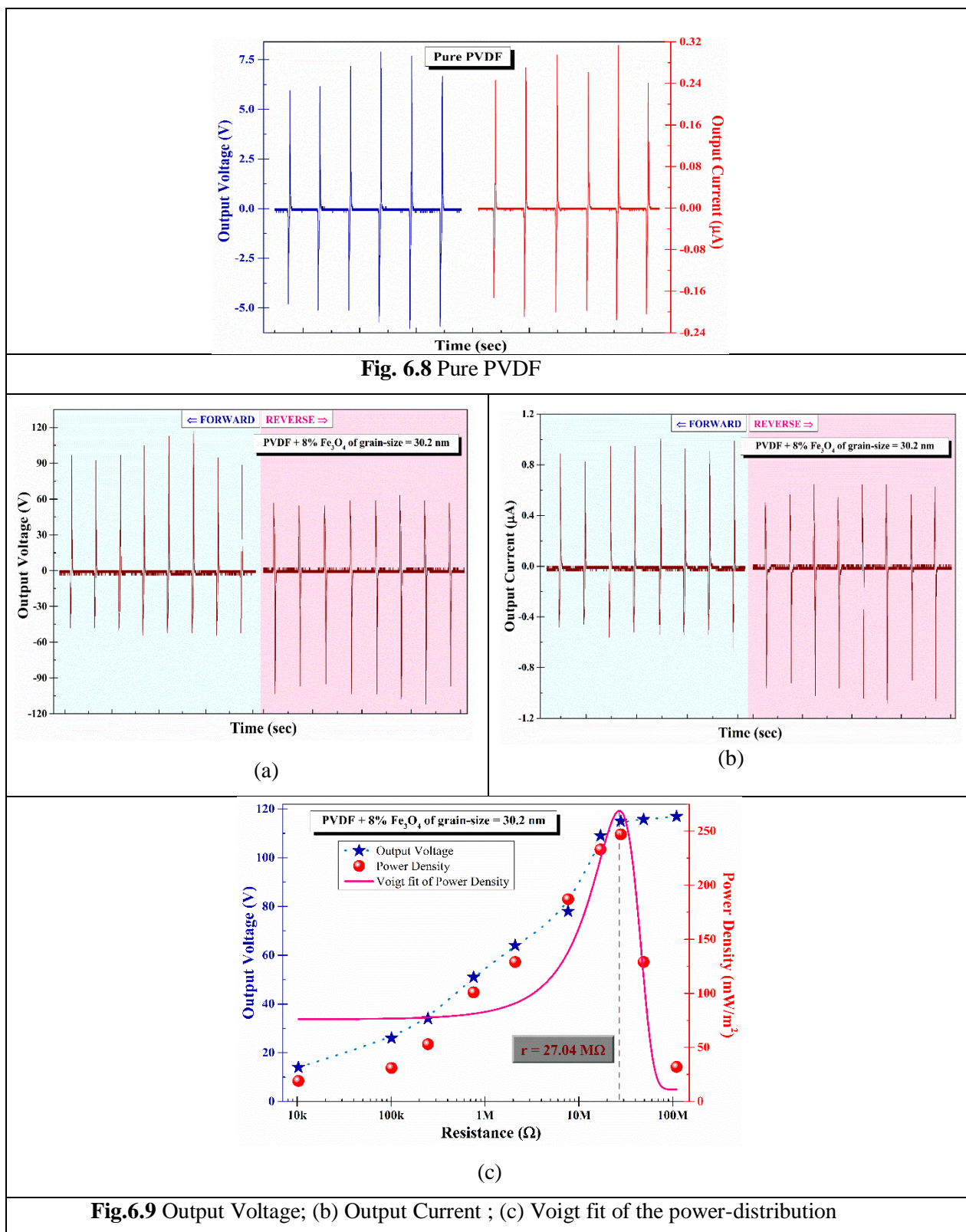
aggregation becomes massive enough to block the continuity of the film, which can be attributed for the degradation of piezo-performance.



## 6.4 Piezo performance

The best overall piezoelectric gain was obtained for the 8% -30.2 nm film, where rapid finger-tapping motion ( $\leq 14kPa$ ) on a  $3\text{ cm}^2$  effective electrode-area can generate open-circuit voltage and short-circuit current as large as 115.95 V and  $1.04\ \mu\text{A}$ , which is nearly an order enhancement from the pure PVDF reference. During the press-action the electrons get accumulated at the film-electrode interface with a voltage-peak and no sooner the electrons start to balance with the piezo-potential causing the diminishing peak-shape. After the release, the accumulated free electrons get back to the electrode and thereby giving an opposite signal. The polarity-reversal for forward and reverse connections confirm the piezoelectric effect. The uneven voltage gain for the press and release action indicates different micro-strain levels at

the interface. Employing a number of resistors ( $10^4 - 10^8 \Omega$ ), the internal resistance of the films was estimated from a voigt fit of the power-distribution using the maximum power-transfer theorem. The 8%-30.2 nm sample delivered output power  $\sim 247.3 \text{ mW/m}^2$  for a resistor close to its internal resistance i.e.,  $27.04 \text{ M}\Omega$ .



## 6.5 Discussion and conclusion

The enhancement of  $\beta$ -phase and piezo-response with the gradual incorporation of  $\text{Fe}_3\text{O}_4$  NP's can be attributed to the fact that, an ion–dipole interaction takes place among the  $\text{CH}_2$ -dipoles in the PVDF chain and oxo-, hydroxo- and carboxylate-groups on the  $\text{Fe}_3\text{O}_4$  NP-surface. Moreover, the electret-doping effect strengthens the polarizability of the PVDF-matrix. As the size of the NP's decrease, due to the synthesis-scheme, the predeveloped surface-charge and the contribution of the polar functional groups on the NP-surface evolves continuously and thereby nourishes the polar  $\beta$ -phase. Besides tiny magnetic particles are most effective for EMI shielding. This trend is quite clear upto 30.2 nm size and 8 wt(%). But, as the particle-size gets smaller; due to high surface-energy, the NP's start to aggregate causing blockage and discontinuity in the film. This degradation becomes massive for the 8.9 nm and 12 wt(%) samples. Comparing the general trends of output voltage, current, maximum power delivered and  $\left(\frac{I_\beta}{I_\alpha}\right)$  ratio the 8% 30.2 nm nanogenerator performed optimally, which had been further employed to light up red, green and blue LED's (~mW). Hence, we can conclude, use of superparamagnetic polar NP's with high dielectric constant and/or superior electret-properties can be assigned to polymer-based new-age piezo-, pyro- and tribo-electric nanogenerators.

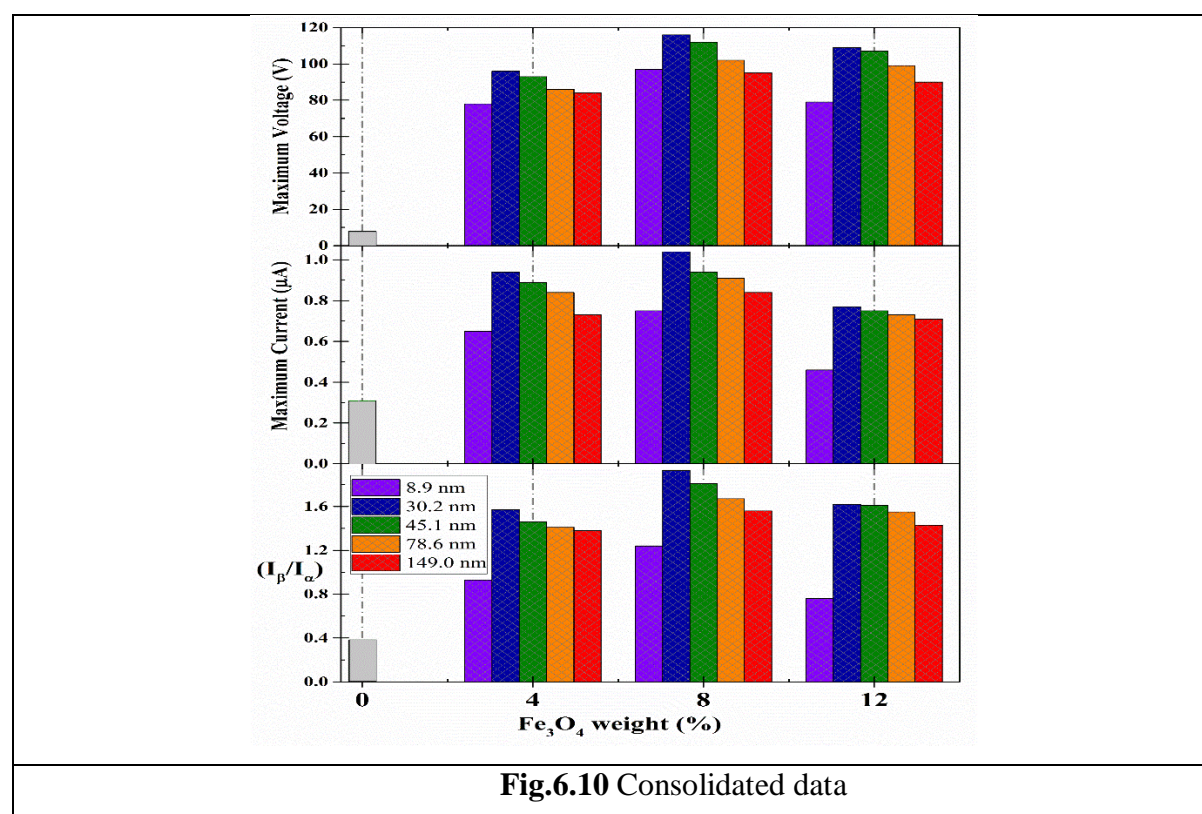


Fig.6.10 Consolidated data

## 6.6 Reference

- [1] Hasan, M. R.; Baek, S.-H.; Seong, K. S.; Kim, J. H.; Park, I.-K. Hierarchical ZnO Nanorods on Si Micropillar Arrays for Performance Enhancement of Piezoelectric Nanogenerators. *ACS Appl. Mater. Interfaces* 2015, 7, 5768–5774.
- [2] Pi, Z.; Zhang, J.; Wen, C.; Zhang, Z.-b.; Wu, D. Flexible piezoelectric nanogenerator made of poly(vinylidene fluoride-cotrifluoroethylene) (PVDF-TrFE) thin film. *Nano Energy* 2014, 7, 33–41.
- [3] Alamusi; Xue, J.; Wu, L.; Hu, N.; Qiu, J.; Chang, C.; Atobe, S.; Fukunaga, H.; Watanabe, T.; Liu, Y.; Ning, H.; Li, J.; Li, Y.; Zhao, Y. Evaluation of piezoelectric property of reduced graphene oxide (rGO)-poly(vinylidene fluoride) nanocomposites. *Nanoscale* 2012, 4, 7250–7255.
- [4] Whiter, R. A.; Narayan, V.; Kar-Narayan, S. A Scalable Nanogenerator Based on Self-Poled Piezoelectric Polymer Nanowires with High Energy Conversion Efficiency. *Adv. Energy Mater.* 2014, 4, 1400519.
- [5] Mao, Y.; Zhao, P.; McConohy, G.; Yang, H.; Tong, Y.; Wang, X. Sponge-like Piezoelectric Polymer Films for Scalable and Integratable Nanogenerators and Self-Powered Electronic Systems. *Adv. Energy Mater.* 2014, 4, 1301624.

# **CHAPTER-7**

## **Grand Conclusion**

## 7.1 Conclusion

In summary, monodispersed and highly water dispersible spherical  $\text{Fe}_3\text{O}_4$  NP's with large variation in size (4 - 150 nm) have been synthesized by a facile microwave-assisted solvothermal approach using disodium tartrate as a crystal grain growth inhibitor and stabilizer in polyol medium. Temperature, pressure, reaction-time (crystal growth time), concentration of surfactants, and density of  $\text{Fe}^{3+}$  ions in the solution play key-roles in the size of NP's. The resultant  $\text{Fe}_3\text{O}_4$  NP's; due to covalent surface-functionalization, exhibit an excellent long-term colloidal stability in aqueous or other polar solutions, which have been further confirmed by Zeta potential measurements. The coordinative effect of carboxylate groups in the surface-composition was further verified from FTIR spectra, whereas thermal degradation of the as-prepared core-shell structure of the NP's was investigated by TGA-DTG measurements. A thorough XPS analysis revealed the difference in binding energies of the tetrahedral and octahedrally co-ordinated Fe atoms along with degree of stoichiometry and related surface-chemistry. A red-shifting and line-shape asymmetry of Raman peaks with smaller size was detected, which have been illustrated by the Phonon Confinement Model (PCM). The calculated optical band-gap ( $E_g$ ) from UV-Vis-NIR absorption spectroscopy increases from 1.59 to 4.78 eV in a very regular fashion with decreasing size of NP's, which was well-explained in the light of Crystal Field Theory (CFT) and Brus equation on the excitonic model. Besides, these  $\text{Fe}_3\text{O}_4$  NP's may be useful in other fields, such as hyperthermia treatment of cancer and targeted drug delivery because of their size-dependent magnetic property, non-toxicity and excellent stability.